A NOVEL MEMS-BASED MICRO HEAT ENGINE AND OPERATING CYCLE

By

LELAND W. WEISS

A dissertation submitted in partial fulfillment of
the requirements for the degree of

DOCTOR OF PHILOSOPHY

WASHINGTON STATE UNIVERSITY
School of Mechanical and Materials Engineering

MAY 2008

To the Faculty of Washington State University:

The members of the Committee appointed to examine the dissertation of LELAND W. WEISS find it satisfactory and recommend that it be accepted.

_____
Chair

_____

_____

_____

ACKNOWLEDGEMENT

There is little doubt that most engineering work is not the result of one person's efforts, but really, the combination of effort by a group working together towards a common goal. The work presented in this dissertation is no different. From the summer of 2002 to the spring of 2008, there have been a large number of people who have made this effort possible by contributing in some way. Over the past few years I've been blessed to have Jennifer alongside for some of the more difficult parts of this process. Her encouragement has made a great difference and I thank her for the important role she's played and will continue to play. There have been many others, like Dan Carpenter and Tiffany Quy who have developed a fabrication or testing procedure that has since been incorporated into the overall device. Hamazeh Bardaweel has proved invaluable in the daily tasks of fabrication and engineering discussions that help solve difficult problems. Jeong Cho deserves recognition for his efforts to improve the thermal switch which was a key component in the operation of the micro-engine. Scott Whalen deserves much credit for his work on the initial engine design and operation. There have been many more who have drifted in and out of this project as my work has continued and I thank all of you for making the last six years more enjoyable than they would have otherwise been. Like so many other jobs and places, the enjoyment comes from the people who journey alongside.

While students have come and gone during my progress, the faculty that have made up my committee have remained constants. I thank all of you for the opportunity to be here working on this device and the personal attention that I have received from each of you. I have learned a great deal about understanding the fundamentals of a problem and how to pursue solutions. Like so many other projects, this one has had its high points and its lows. I appreciate your weathering of the storms as well as the celebration of the successes. It is my hope that when you look back over the past six years you will consider them time well spent.

As I look back over the past few years I am thoughtful of a parallel, and yet, intertwined journey. When I first visited Pullman in the late winter of 2002 I was reacquainted with an old friend whom I hadn't thought much about during my years in the Midwest. Built as America's final transcontinental railway, The Milwaukee Road spanned several western states and five mountain ranges on its way from Chicago to the Northwest Coast. Its history is fraught with bankruptcy and mystery. In 1980 it was abandoned across the west, leaving quiet and failure behind it. Though it has been gone for nearly thirty years, the leftovers of the Milwaukee Road's presence in the West remain haunting and thoughtful reminders of things larger than oneself. Halfway between Spokane and Pullman, at a small town named Rosalia, the Milwaukee Road's old transcontinental right of way still spans the valley on concrete viaducts that are impressive structures to this day.

Inspired by the old railroad's sprawling signature, I set out to explore as much as I could during the summers in Pullman. From Eastern Montana to the city of Seattle I tracked the old line, recording as much as possible in photographs along the way. Somewhere along the journey, I began to appreciate the wonder of big skies and the beauty of high desert plains. There was a majesty to the world through which the Milwaukee journeyed. As I pondered the possibilities of what could lay beyond the small worlds we create, I was led to the Milwaukee's deserted tunnel atop the Saddle Mountains. It was dark and cool compared to the hot desert that surrounded it and as I stepped inside, I could feel without question that things weren't quite as I thought they were.

I think, on some level, we hold out hope that we're not here all alone as a cosmic accident. That is a disconcerting thought, however, because it means the world we create around us, a world which seems so important, might be smaller than we think. On that day in the Saddle Mountains, I knew that we were not here alone. There is something greater that is reaching out to us through our passions and our loves as we explore and live them. I felt its presence and welcome in the tunnel and have felt it many times since just as deep cries out to deep.

Since that time, life and the journey has changed a great deal for me. Several times I have been faced with the thought of "walking away" from this dissertation or settling for a masters and doing something else. Yet, with the help and encouragement of the people I've already mentioned and the God who loves us all so much, the will to continue was found. Lord, thank you for all that's been done and Your hand in all of it. Any acknowledgment section would be remiss to leave You unmentioned.

A NOVEL MEMS-BASED MICRO HEAT ENGINE

AND OPERATING CYCLE

Abstract

by Leland W. Weiss, Ph.D.
Washington State University
May 2008

Chair: Robert F. Richards

This dissertation presents operating characteristics of a MEMS-based micro heat engine. The engine is shown to operate in two distinct modes. First, at sub-resonant frequencies, then at resonant frequencies. Each operating mode is shown to have distinct thermodynamic characteristics.

Integration of a thermal switch is shown as an effective means to introduce heat or reject heat from the micro-engine. The engine is shown to operate from a constant temperature heat source via thermal switch operation. Additionally, use of the thermal switch to reject heat from the micro-engine results in the ability to increase operating speeds. This enables high frequency sub-resonant operation (beyond 100 Hz) and operation at resonant frequency.

To improve micro-engine performance and power output at sub-resonant frequencies, several designs are considered. These include micro-engines constructed with both 25 mm^2 and 100 mm^2 top membranes. Maximum power output is 2.6 mW using a micro-engine constructed with a 100 mm^2, 2 μm thick silicon top membrane and evaporator membrane with 40 μm high, SU-8 based fluid wicking structures. The maximum efficiency obtained is .15 % using a 25 mm^2, 300 nm thick silicon-nitride top membrane and evaporator membrane with 10 μm high, SU-8 based fluid wicking structures.

Increasing operating speed to the micro-engine resonant frequency is shown to produce cycle work. The micro-engine produces up to 6.7 μW of cyclic mechanical power when operating at a resonant frequency of 125 Hz.

Contents

List of Tables

List of Figures

Dedicated to Jennifer Madden Weiss.

Thank you for telling me that it could be done

and believing in me too.

Chapter 1

Introduction

Power generation, and the efficiency with which it is generated, is becoming an increasingly important issue around the world. The concern over energy consumption is driving a great number of technological developments in a wide range of specific areas and industries. One of the strategies to limit energy use and consumption is to use energy that is already available as part of a larger process. Technologies of this type can take many forms, however, all must be effective and relatively low-cost in order to be attractive.

In recent years, one area of intensified research on the micro scale has been the scavenging of waste energy for the purpose of doing useful work. Waste energy is most often associated with energy that is discarded by some process, or "wasted." Most energy harvesters have taken the form of vibration harvesting devices, especially on the micro scale [1]. However, there have also been some efforts to harvest waste thermal energy. Thermoelectric-based devices attempt to make use of this thermal energy and have met with limited success. The work presented in this dissertation examines the operation and thermodynamic cycle of a micro-heat engine that can be operated from a low temperature heat source like waste heat. Devices like this micro-heat engine are increasingly necessary to power the wide variety of

micro actuators being developed around the world. The opportunity to power them with low-grade heat is growing as well. Not only do standard cycles like the Otto cycle produce a great deal of waste heat, but emerging technologies like fuel cells reject heat that could be useful as well.

1.1 Engine Concept

Among the many challenges of engine design in any scale is the minimization of losses that effect engine operation. Reciprocating engines constructed as macro scale devices share the same basic sources of system inefficiency. Of the total energy available to the engine (as supplied by fuel) only about $\frac{1}{3}$ is output as useful work. The remaining $\frac{2}{3}$ is split equally between heat losses out the exhaust stack and heat dissipated through the radiator [2]. These losses are of particular interest in the design of the micro heat engine presented in this work. A large amount of radiator dissipated heat is due to heat of combustion. This unused energy is transmitted through cylinder walls and the engine head into the circulating coolant flow. However, significant heat is lost due to the frictional wear of piston rings and crankshaft bearing friction as well. A diesel engine sized with a 137 mm bore and 135 mm stroke can exert nearly 250 N of frictional force on the piston rings alone [3]. For macro scale engines, these frictional and combustion heat losses remain a manageable fraction of both the total engine output and total system loss. However, when engines based on rotary motion are downsized, these frictional and combustion losses become controlling factors of successful engine operation [4].

There have been many attempts to downsize these cycles and produce power on the micro scale. These efforts have produced micro-scale engines that operate on the Otto, Brayton, and Rankine Cycles [5, 6, 7]. What has plagued these devices, however, is the combined effects of poor bearing life and combustion quenching in the high surface area to volume

combustion chambers [4].

One of the goals that has driven the development of the micro heat engine presented in this dissertation has been the desire to avoid these issues common to other approaches. To this end, the micro-engine presented in this work has been designed as a closed system, external combustion device capable of operating from a variety of heat sources. This makes the engine fuel non-specific. It also makes operation from various existing systems that produce waste heat a real possibility. The design of the engine as an external combustion device eliminates issues related to micro-scale combustion quenching. In addition, the micro-engine is designed to have the motion of a flexing expander. Without rotating parts, the design is able to mitigate frictional losses inherent to other approaches. The engine has also been designed as a low-cost device that is capable of manufacture using simple clean-room techniques. Manufacture is accomplished via "batch" fabrication that produces many engine components with relatively few processing steps. In this way, the engine has been designed to be a highly flexible, robust, and inexpensive alternative to many of the more complicated micro heat engines under development.

1.1.1 Engine Design

The design of the micro heat engine is quite simple. Two thin membranes about the size of a thumbnail are separated by a thin gasket about 100 μm thick. This forms a cavity between the membranes which is filled with a working fluid that can boil at low temperatures. Figure 1.1 shows this simple concept in cross-section.

The membranes are fabricated in batches starting with standard three inch diameter silicon wafers. Heat addition is through the lower membrane, called the evaporator membrane, and is accomplished by one of two methods. In many tests a gold resistance heater is fabricated

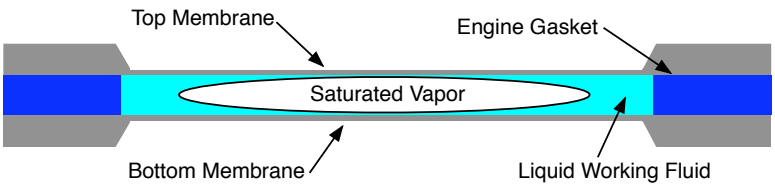

Figure 1.1: Basic Engine Cross-section

on the lower membrane to introduce heat into the engine. This allows accurate assessment of engine performance as a result of timed heat inputs and amounts. However, this does not allow the operation of the engine from an external heat source as originally intended. The second heat addition method is via a device called a thermal switch (Section 1.1.3). The switch can introduce (or reject) heat to the engine from an external source and allows operation of the engine as outlined in the original concept. The introduction of heat to the engine cavity forces the evaporation of working fluid and expansion of the top membrane. The top membrane is analogous to shaft output from a reciprocating engine. In this case, however, the useful work is performed as a "push" motion instead of rotation.

1.1.2 Engine Operating Cycles

There are two operating modes for the micro-engine. The first involves operation when the micro-engine is running at speeds less than its resonant frequency. In this mode, heat addition is through the lower membrane which causes evaporation of the working fluid and an increase in pressure within the cavity. As a result, the membranes stretch apart and produce useful work. Once fully expanded, the engine is cooled and awaits its next heat application. Engine cooling is accomplished by either allowing the micro-engine to passively cool to the surrounding environment or by using the thermal switch to extract heat and ready the engine for the next cycle. Figure 1.2 illustrates this operating mode while Figure 1.3 shows the resulting pressure-volume curve.

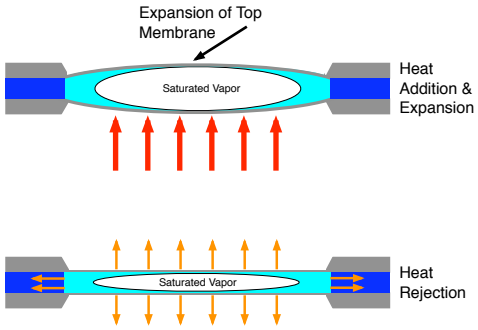

Figure 1.2: Engine Operation at Sub-Resonance

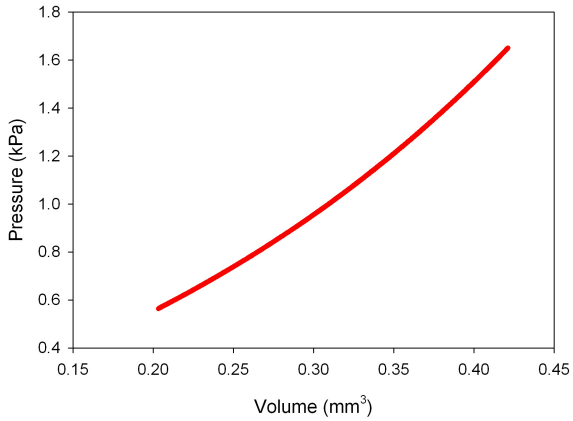

Figure 1.3: Typical P-V Plot for Sub-resonant Operation

When the micro-engine is operated at its resonant frequency, it enters the second mode of operation. Like the sub-resonant operating mode, resonant operation involves heat addition and rejection, however, compression is added to the cycle. Resonant operation also causes the heat addition and volume expansion to operate out of phase with one another. Figure 1.4 illustrates micro-engine operation at resonant conditions. Figure 1.5 shows a typical pressure-volume plot. The key to operation at resonant conditions is the ability to operate the engine at increased frequency. Naturally, high speed operation results in increased engine temperatures which can lead to overheating. This is controlled via the active rejection of heat to a cold sink, controlled by the thermal switch.

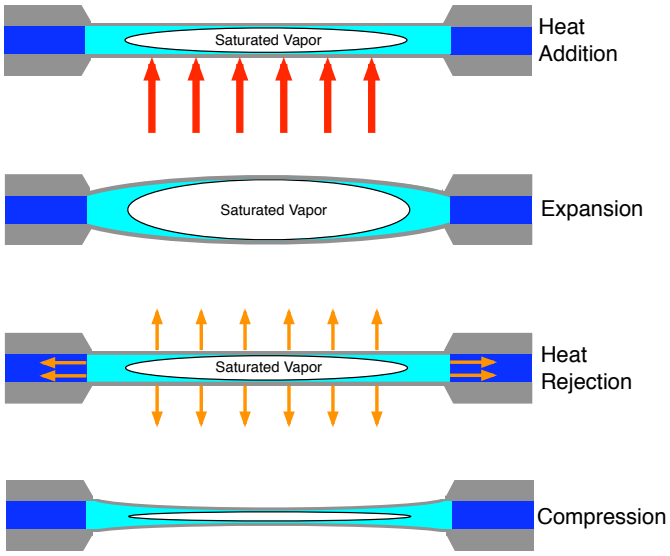

Figure 1.4: Engine Operation at Resonance

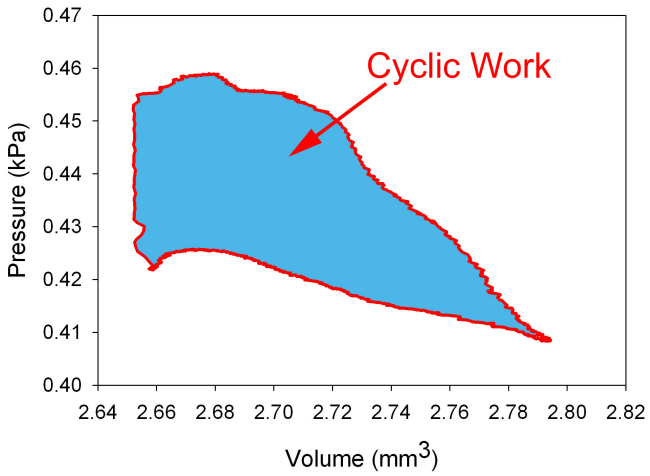

Figure 1.5: Typical P-V Plot for Resonant Operation

1.1.3 Thermal Switch Design and Operation

The purpose of the thermal switch is to serve as a conductor of heat between the micro-engine and an external heat source or sink. The switch can either introduce heat to the micro-engine or reject heat depending on its temperature. Like the engine, the switch has been designed to meet this need as simply as possible. The switch consists of a small silicon die that

rests above a constant temperature heat sink. The heat sink is maintained at the desired temperature of operation. The silicon die and heat sink are translated up to 150 μm and brought into contact with the evaporator membrane. This contact initiates heat conduction between switch and micro-engine. The translation of the switch back to its original position stops the heat transfer and completes the heat addition or heat rejection cycle. Figure 1.6 shows the micro-engine cross-section mounted above the thermal switch and heat sink. The switch and heat sink are shown mounted above a piezo-stack actuator which controls the vertical position of the switch.

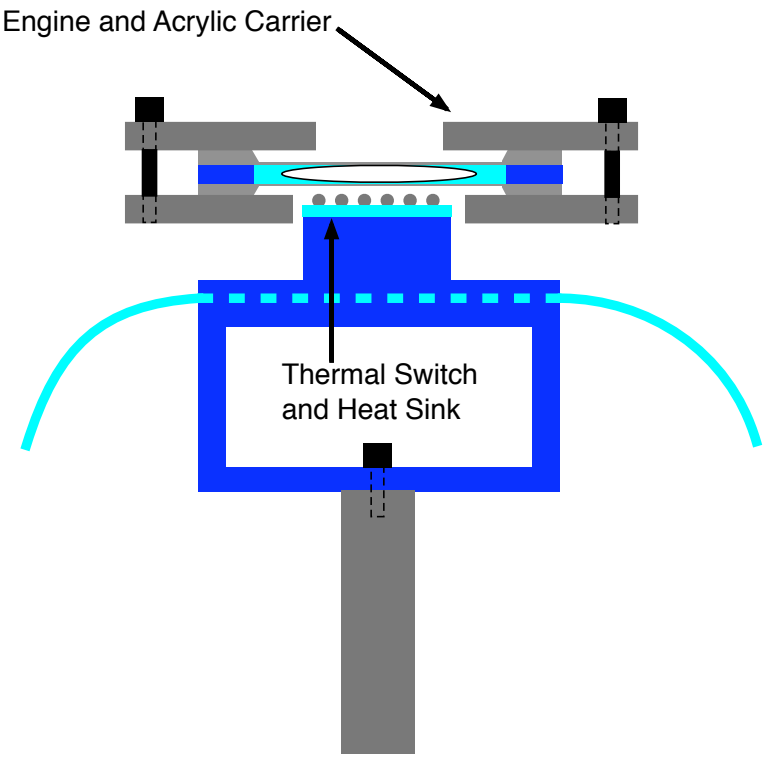

Figure 1.6: Combined Engine and Switch Setup

The thermal switch plays a critical role in the operation of the micro heat engine. In most tests, only a single switch is used. The switch operates in conjunction with the electrical heater on the micro-engine evaporator membrane. The electric heater controls heat addition to the micro-engine. The switch is maintained at a low temperature and periodically contacts the evaporator membrane. This contact controls heat rejection from the engine. This

allows the micro-engine to operate at increased speeds as it no longer tends to overheat. The increased speed of operation yields increased power output for sub-resonant operation. Increased speed also allows operation at the natural frequency of the micro-engine.

Alternately, the switch may be maintained at a high temperature and used to control heat addition to the micro-engine. In this mode, the switch periodically contacts the evaporator membrane and heat conducts into the cavity as a result. As with the use of the electric heater, this results in useful work output from the micro-engine. Occasionally, two thermal switches are used to simulate micro-engine operation from both hot and cold temperature sources. In this mode, one switch is maintained at a low temperature while the other is maintained at a high temperature. Operating out of phase with one another, their contact with the evaporator membrane results in cyclic heating and cooling of the micro-engine.

1.2 Component Fabrication

The micro-engine, as shown in Figure 1.1, is a fairly simple device consisting of two membranes, a gasket to define the cavity, and working fluid. Almost all the fabrication steps necessary to produce the engine and thermal switch are performed in the clean room at Washington State University. This gives excellent control and accessibility to the device manufacture and design. Both micro-engine and switch are fabricated using standard IC chip-type fabrication techniques that are common to many micro-fabrication processes. Because of this, the cost of individual engines remains small. Additionally, due to the batch fabrication process, many engines and many switches may be constructed from only a few fabrication steps. This achieves one of the system design goals: a low cost alternative that is easily produced using standard fabrication techniques. An introduction to the fabrication of the micro-engine and thermal switch is presented in this section.

1.2.1 Lower Evaporator Membrane

The micro-engine lower membrane is called the evaporator membrane. This is because heat is introduced through this membrane and evaporation of working fluid occurs from its surface. The evaporator membrane is fabricated from a silicon wafer to a thickness of 2 μm. The evaporator membrane consists of a gold resistance heater that is patterned across its inner surface. This allows heat addition to the engine from an electrical source. In addition, a gold RTD is fabricated on the membrane. This allows the temperature of the lower membrane to be monitored during engine operation. Evaporator membranes are also fabricated with polymer-based wicking structures. These wicks maintain a thin layer of liquid working fluid across the membrane surface and improve the engine evaporation characteristics as a result. A top-down view of a completed evaporator membrane is shown in Figure 1.7. The radial wicking structure is clearly noted with the gold circular pattern of the electrical resistance heater beneath it.

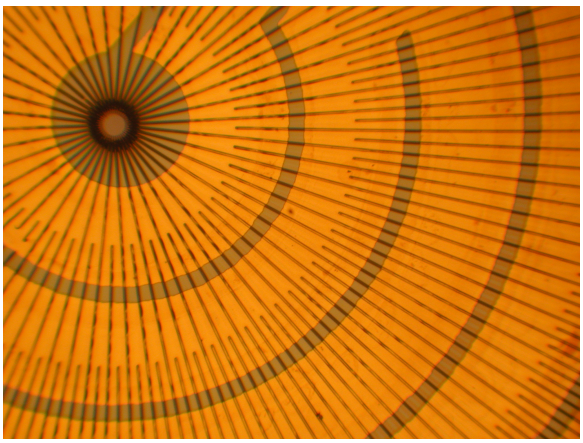

Figure 1.7: Top-down View of Evaporator Membrane

1.2.2 Top Expander Membrane

The top membrane serves as the work output membrane for the micro-engine. Like the evaporator membrane, the top membrane is fabricated from silicon wafers and is made of

either silicon or silicon-nitride material. On some top membranes, a gold RTD is fabricated to allow the temperature monitoring of the top membrane during operation. A picture of fabricated top membranes is shown in Figure 1.8.

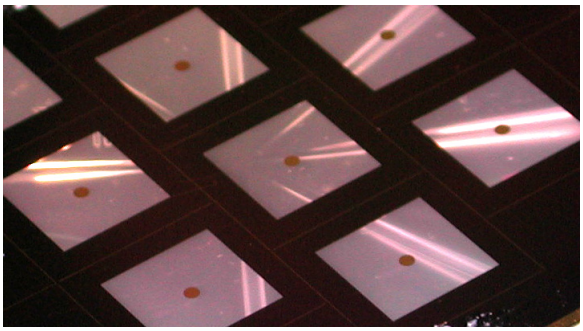

Figure 1.8: Finished Top Membranes on a Silicon-Nitride Wafer

1.2.3 Engine Cavity

The micro-engine cavity is fabricated using semi-conductor tape. The desired cavity shape is cut from the tape and placed over the lower evaporator membrane. The thickness of the tape determines the cavity thickness and the amount of working fluid present in a fully assembled engine. After placement on the lower membrane, the cavity is filled with the desired amount of working fluid. The fluid tends to collect at the edges of the cavity due to surface tension forces. The presence of the wicks on the evaporator membrane help draw fluid back across the membrane surface and improve engine operation.

1.2.4 Thermal Switch

The thermal switch die is fabricated from silicon wafers like the engine membranes. In some cases, the presence of liquid metal droplets on the surface of the thermal switch has been noted to improve the heat conduction aspects of the switch. The deposition of these droplets is accomplished by the patterning of small gold targets atop the switch die followed

by their exposure to mercury vapor. The mercury preferentially deposits on the gold targets and yields a switch die with small liquid metal droplets arrayed across its surface. The completed switch die is placed above the constant temperature heat sink as shown in Figure 1.6. Water at constant temperature is passed through the heat sink and the switch is thus maintained at the desired temperature.

1.3 Engine and Switch Assembly

The combination of the three micro-engine components (evaporator membrane, cavity, and top membrane) result in an engine that is ready for operation. After the cavity has been filled with working fluid, the top membrane is placed on the cavity top, sealing the working fluid between the two membranes. Figure 1.9 shows the micro-engine in its acrylic carrier. The carrier not only allows transportation of the assembled device, but also maintains a clamping force that ensures a good seal about the cavity.

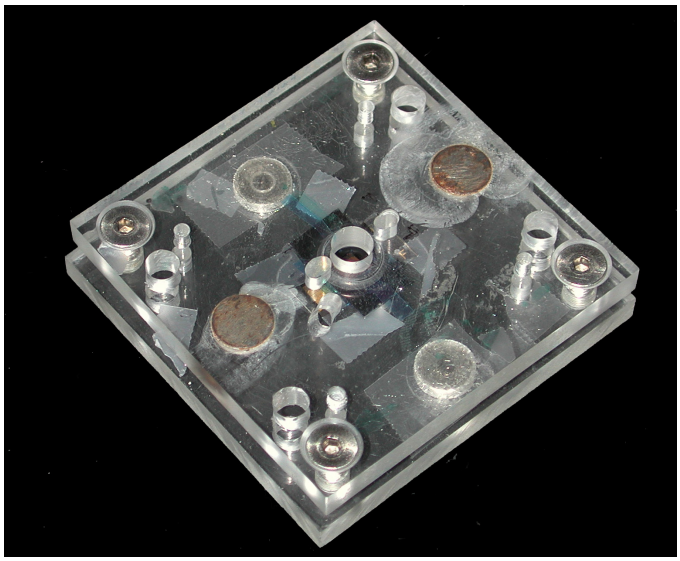

Figure 1.9: Assembled Engine in Acrylic Carrier

Once housed in the carrier, the entire micro-engine and acrylic carrier assembly is visually aligned over the thermal switch. A schematic of the setup is shown in Figure 1.6. The

photograph in Figure 1.10 is of the actual device assembled and ready for operation. Figure 1.10 also shows an optional acrylic chamber that can be used to isolate the system from the surrounding environment.

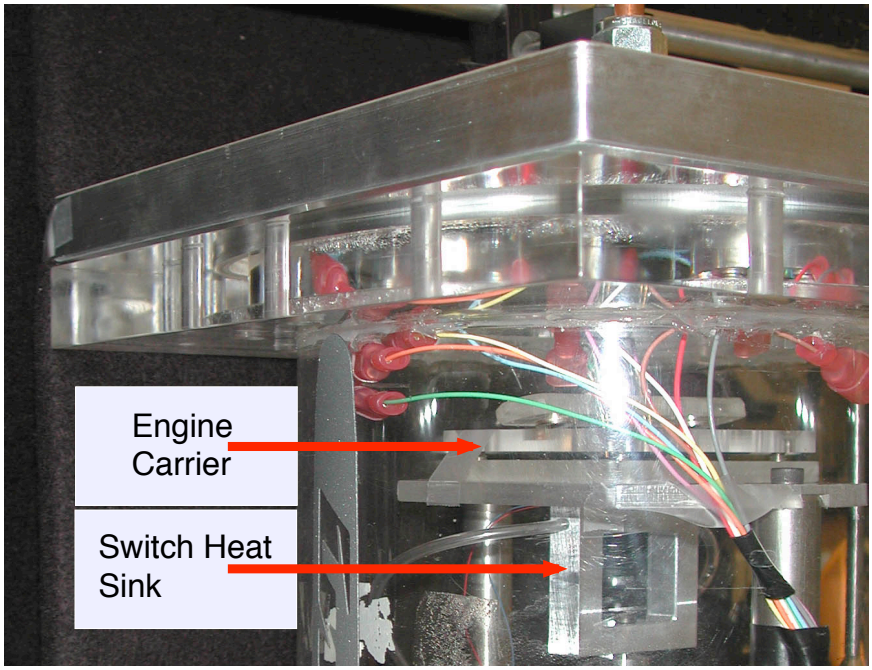

Figure 1.10: Assembled Engine and Thermal Switch Ready for Operation

1.4 Research Objectives

There are three primary research objectives for this work. The first goal is maximization of power output during sub-resonant operations. This is accomplished by increasing the micro-engine speed of operation via heat rejection to the thermal switch. In addition to the use of a thermal switch, different engine configurations are examined to further increase the power output.

The second goal of this research is to operate the micro-engine at its resonant frequency as shown in Figure 1.4. Operation at resonance is desirable for several reasons. First, there exists the potential for a greatly increased efficiency of operation. This is true because, like

a playground swing, a relatively small energy input may be used to exact a large motion. Additionally, once set in motion, the swing tends to stay in motion with little input. For the case of micro-engine operation, the same fundamentals are true: relatively small heat inputs have the potential to result in a large continuous output. A second reason for interest in the resonant cycle is the production of cycle work. Resonant operation is made possible because of the ability to operate at high frequencies due to active heat rejection via thermal switch.

The third and final goal of this research involves operation from low-grade heat sources. This goal entails operation of the micro-engine using a constant temperature heat source for operation at sub-resonant conditions. To attain this goal during resonant operation requires the use of a constant temperature heat source and cold sink. This involves the use of thermal switches to control both heat rejection and heat addition to the engine. The setups for these operations most closely match real-world conditions where the device must operate from low-temperature heat sources and perform useful work.

1.5 Dissertation Layout

Many of the first chapters of this dissertation relate to the basic fabrication, construction, and test setups for the micro-engine and thermal switch. There are several different variations of engine construction and test setups that are discussed. The results of this work are presented in an order that reflects the research objectives defined in Section 1.4. First, results from sub-resonant operation are discussed. These include operation from both electrical sources as well as constant temperature heat sources. Next, results from resonant operation are presented, again including results from both electrically operated and heat source/sink operated micro-engines. Finally, overall conclusions are drawn based on these results.

Chapter 2

Literature Review

2.1 Introduction

One of the constants within the engineering field has been the development of devices that produce power. As the world has changed, these devices have been developed across a broad spectrum of specialities. Of particular note, is the trend of miniaturization. In fact, the past twenty years have seen dramatic developments in the fields of micro actuation and micro power generation. One of the first successes was the 1988 demonstration of an electrostatically operated micromotor. Since that time, the complexity and application of micro devices has expanded greatly [8]. The design and manufacturing capabilities that have accompanied this revolution provide the opportunity to develop MEMS (Micro Electro Mechanical Systems) devices that create power and control heat transfer.

In 1992, Muntz *et al.* identified transient energy release from pressure-driven microdevices as a legitimate and available source of power production [9]. Their work consisted of simplified modeling of several potential systems and cycles including a closed system (similar to an

Otto cycle) and open system (like that of a Brayton or Rankine cycle). Specifically, their study targeted the potential of transient gas heating to deliver useful work on the micro scale. They surmised that this approach could deliver a device that produced far greater force per unit volume than any similar electrostatic device. Albeit an early and simplified look at micro-scale work production, Muntz *et al.* identified several issues that have remained salient to this day and can be seen in the wide variety of approaches that have blossomed since the study was completed in 1992. First, they noted the action and thermal design of the cavity enclosing the gas under consideration is crucial to the design of the device. Also, the ability of the cavity walls to conduct heat and the use of thin, highly insulating layers on conducting substrates was noted by the authors as key. As can be seen elsewhere in the literature, these issues related to thermal control on the micro scale remain among the most studied and problematic to this day. In their summary, the authors noted that, "A class of microdevices with potentially attractive performance characteristics has been identified...[and] pressure driven microdevices require further study." The breadth of devices and diversity of approaches that have been examined since 1992 seem to indicate that this conclusion was indeed valid. As predicted by the authors, these further studies have focussed a great deal on the challenges they identified. The following literature review examines many of these approaches to micro power generation.

2.2 Micro Actuators

PowerMEMS is a designation given to a class of MEMS devices that generate power or pump heat [10]. These can include heat engines, fuel cells, and other energy harvesting devices. Different approaches have produced both internal combustion and external combustion devices that operate on different cycles. Among some of the more simple devices designed to produce useful work is a class of phase-change actuators that produce mechanical work.

Many of these devices are actuators embedded within a micro-pump system [11]. Others are constructed as actual valves that can expand and contract to control fluid movement within the system [12]. An examination of this class of actuators is presented.

2.2.1 Phase Change Actuators

Bergstrom *et al.* fabricated a micro phase-change actuator that could be applied to many different situations including biotechnology and micro pumping systems [13]. The device consisted of a lower glass substrate which supported the actuator and provided the bottom surface for the actuator cavity. The cavity was formed by an anisotropic etch of a silicon wafer that left a thin membrane on the wafer, but a cavity below it. This cavity served as the actuator cavity. An elevated heater (10 μm) was placed above the glass substrate and the combined cavity and membrane were placed over the heater. This setup was filled with Freon-11 or methanol working fluid and sealed. The size of the cavity formed was about 900 μm by 900 μm by 300 μm. The top membrane served as the work output membrane and pressure was monitored within the cavity via integrated sensors. Heat was applied to the actuator via the electric heater and the evaporation of the working fluid caused an increase in pressure within the cavity. The best performance of the actuator yielded a pressure increase of 1.2 atm in a response time of 100 ms. The power input was 100 mW. The authors noted that increased performance derived from insuring the heating element was covered by a thin layer of liquid. Not only was the response of the actuator improved, but the heat lost to the lower glass substrate was reduced. In a test where the heater was constructed without elevation above the substrate, losses were reduced from 98 % to 83 % when the heater was covered with a thin layer of working fluid. Elevation of the heater above the lower glass slide proved to be advantageous to the design as it allowed peak pressure to be achieved about 60 ms sooner than a slide mounted heater. This was due to a reduction in heat loss to the glass substrate.

Yang *et al.* noted the ability of MEMS-based phase change actuators to simultaneously generate large forces through lengthy displacements. As a result, Yang *et al.* developed silicon nitride and composite silicone membrane-based actuators for the purpose of valve control [12, 14]. The device was constructed by spinning a thin layer of MRTV1 on the front side of a silicon-nitride wafer. The backside of the wafer was etched using KOH, leaving the silicone membrane intact on the front side with a surface area of 9 mm^2. A resistance heater was patterned on a lower silicon-nitride membrane and the composite silicone membrane and heater membrane were brought together. A cavity between the two was filled with various fluids including air, water, and several refrigerants. By applying heat via the resistance heater, the fluid within the cavity was evaporated and the composite membrane was deflected. The system required 130 mW of electrical input to deflect the composite membrane up to 200 μm. When operated at a transient state, the actuator showed slow responses, especially when cooling between heat applications. The cooling time to return to initial deflection was determined to be 37 seconds for a device using pf5060 refrigerant.

Similar to the work by Yang *et al.* is that of Sim *et al.* where a phase-change type actuator was constructed using a silicone rubber diaphragm and working fluid chamber [15]. As with other systems of this type, the evaporation and condensation of the working fluid actuated the membrane, however, in this case the membrane displacement provided the volume change necessary to move fluid through the pump system. A heater was fabricated via gold deposition on a glass substrate which formed a cavity beneath the rubber diaphragm. The 4 mm square diaphragm was formed by spin-coating silicone rubber atop an etched silicon cavity to a thickness of 30 μm. The assembled actuator proved capable of deflections up to 230 μm when the heater was actuated for four seconds using water as the working fluid. The system peak performance was at .5 Hz given a duty cycle of 60 %.

Paraffin was used as the working fluid in a phase-change actuator designed by Klintberg *et al.* Unlike typical phase-change actuators that rely on the change from liquid to vapor to provide mechanical actuation, the paraffin device relied on the transition from solid to liquid to move a solid silicon disk up to 100 μm [16]. The device was constructed using solid circular centers, attached via thin membranes to an outer substrate. Two of these were placed atop one another with differing radii of the solid centers. This constrained the motion of the actuator to vertical only. A cavity was formed between the two actuator pieces in an annular gap which was filled with the paraffin working fluid. The overall size of the device was about 150 mm in outside diameter and 1mm in thickness. DRIE was used to define the annular cavity spaces as well as the constraining membrane of the central solid disks. The device was heated from the center and the subsequent heating of the solid paraffin in the outer annuli caused a phase change from solid to liquid and forced the actuator to translate. The total distance traveled was up to 100 μm given a temperature increase of 60 K. The ability of the device to move under loading was also examined. With loads of up to 3 N, the actuator proved capable of maintaining 80 μm of deflection (out of its original 100 μm). Some issues were encountered with maintaining a level actuation of the silicon disk and the duration of time required to reach full actuator extension was slow at 15 seconds. The authors noted that further miniaturization of the device should reduce these response times, however, a smaller device carried with it limitations in maximum deflection as well as force.

The similarity of the approaches to phase change actuators allowed the development of an encompassing model that related the thermodynamics of the actuator to the operation of a pump system as a whole [17]. Henning's 2-d model examined several aspects of actuator operation, particularly the working fluid constrained within the cavity. The entire thermodynamic process was modeled, including evaporation and condensation as a result of heat application and actuator volume change. This thermodynamic model was coupled mechanically and thermally to a membrane model which approximated the actuator work output. Henning asserted that a lumped capacitance and lumped resistive approach to heat transfer

works well on the length and time scales considered (typical lengths between 30μm and 1000 μm). Both transient and steady state situations were investigated by the model. Different working fluids, substrate thicknesses, and different power inputs were also considered. When compared to actual device performance, the model predicted actuator and valve response well and showed the importance of convective heat loss when considering the system.

Whereas work by Henning created a somewhat universal approach to modeling phase-change actuators on the micro scale, work by Whalen *et al.* produced a universal look at these devices based on testing and modeling. In this work, the factors that govern the performance of these phase change actuators were investigated including energy budget, efficiency of evaporation, and work output from the device [18]. As with other actuators of this type, the device used consisted of two thin membranes separated by a thin cavity. The cavity was filled with working fluid, 3M^{TM} pf-5060dl. The lower membrane was fabricated with a gold resistance heater which served to power the actuator. Micro channels were fabricated from SU-8 on the lower membrane (above the heater) to improve the evaporation of the fluid when heat was introduced. Several channel designs were used, the most effective for the slow operating speeds of this device being an annular design. In conjunction with this physical testing, a numerical model was developed to predict and detail some of the specific performance characteristics of the actuator. Not only was the mechanical effect of the flexing membranes modeled, but the evaporation and condensation of the working fluid as a result of heat addition was included as well. This led to a highly successful model, capable of matching experimental results well. The authors were able to conclude many significant points regarding the operational characteristics of these types of actuators. These included the importance of matching input energy to the amount required to evaporate and dry the working fluid on the lower evaporator membrane. This resulted in the most efficient operating points considered. The effects of thermal mass on the evaporator membrane was also noted to contribute significantly to the actuator efficiency, increasing as the thermal mass decreased. The actuator was able to produce up to 123 kPa with a maximum thermal

efficiency of .15 % given a single heat application. At 10 Hz, the efficiency of operation declined to .11 % with a power output of 150 mW. This was due to the heating of the actuator and the subsequent decline in evaporator efficiency.

Kim *et al* investigated the performance of passivated and non-passivated micro heaters for the purpose of bubble nucleation in DI water [19]. The heaters were constructed over a silicon substrate with an 3 μm insulating layer of $Si0_2$. The heater was fabricated from Tantalum nitride (TaN) with aluminum electrodes following typical sputtering techniques. The overall size for the heaters was about 22 by 22 μm. An open pool of DI water was placed above the heaters and high speed visualization equipment was used to track the bubble nucleation, growth, and collapse versus time. The heaters were actuated at 8 Hz and their power input was recorded. Using a previously developed model for bubble pressure, the work of the vapor bubble against the pool of DI water was calculated. The bubble was determined to perform up to 4 nJ of work against its surroundings over a range of power densities from 1 to 6 $\frac{GW}{m^2}$. Based on the amount of power applied to the heaters, the maximum efficiency (defined as bubble work to input energy) was found to be about 1.3 % for optimal conditions. While an impressive efficiency figure for a device on this scale, the authors do not record the operating temperatures of their experiment and hence, it is difficult to conclude how this process compares to those of other actuators.

A different approach was taken by Song *et al.* who, instead of relying on flexing membranes, used vapor bubbles entrained in fluid to provide mechanical pumping [20]. In this manner, the phase change of a working fluid was directly responsible for the generation of fluid flow. For the purpose of these experiments, the device was constructed using Pyrex glass tubes with diameters of 1 mm and a length of 31 mm. The tube was attached at either end to water reservoirs that provided both a source and sink for any fluid flow. Heaters were fabricated from thin resistive wire and placed periodically beneath the glass tube. The heaters were actuated in sequence, such that a vapor bubble was propagated at one end of the tube, then

progressed down the tube length. This motion of the bubble resulted in fluid flow within the tube. When the bubble reached the far end of the tube, the lack of heat caused it to collapse within the fluid. The power requirements for the device were fairly high as it consumed 11 W and generated a liquid flow of up to 5.0x10^{-9} $\frac{m^3}{sec}$.

2.2.2 Thermoelectric Generators

Phase change actuators have been shown effective in the conversion of thermal energy to useful mechanical work. Thermoelectric (TE) devices also seek to generate useful power output from thermal input, however, in the form of electricity. Thomas Seebeck first discovered what is now known as the "Seebeck Effect" in 1821 and work on TE devices has proceeded ever since [21]. A review micro TE devices and progress on the MEMS scale is presented here.

One application of micro TE devices has been investigated by Strasser *et al.* In this device, the heat needed to drive the Seebeck effect could be generated by computer chips and the TE has been shown capable of 5 V output across 5 K [22]. The authors noted that, unlike conventional TE devices, a micro device operates in a significantly different regime. The limitations on height of the electric legs as well as a limited temperature gradient limit the output of these generators. As such, careful material selection was critical. Pure poly-Si was used to build up miromachined CMOS generators based on the need to effectively conduct heat through the structure as well as generate as much electrical output as possible. The poly-Si generators were tested over a 10 K temperature gradient and produced up to 30 $\frac{V}{cm^2}$ across an open circuit. Sized to 1 cm^2, the authors asserted the output would be 1 μW, 5 V across a 5 K temperature gradient. The power density of the device can be calculated to be approximately 45 $\frac{W}{m^2}$.

Similar to the work of Strasser *et al.* is that by Leonov *et al.* In this work, the human body was considered for the purpose of supplying heat to power a micro-TE [23]. While the authors noted their preferred use of poly-SiGe in this application, they constructed a device utilizing more classical BiTe thermopiles to speed development. 48 thermopiles were used in the device, each with a volume of approximately 175 mm^3. At the same time, conditioning electronics were developed to control and stabilize the output of the generators. This first device proved capable of generating 100 μW which was stored in NiMH batteries for use in wireless packet transmission. The approximate temperature gradient used to drive this output was 5 K. The power density of the device was calculated to be about 12 $\frac{W}{m^2}$. The authors asserted that future use of poly-SiGe has the potential to greatly improve the TE output over a similar temperature gradient and for lower cost. They predicted that future poly-SiGe based TE devices will be able to output up to 30 $\frac{\mu W}{cm^2}$.

The combination of a micro-TE and micro-vibration harvesting device was investigated by Sato *et al.* The concept put forth by the authors was for a TE designed for use on humans as a wearable technology. The device combined different characteristics of both thermo-electric and vibrational devices [24]. The authors also created a technology called "SeaiT," or Seamless Integration Technology, that enabled the planar construction of multi-function devices. In concept, the combined device used the variable capacitance of the vibrational device to boost the charge output from the TE. The energy was then stored in a capacitor for use in a micro system. The test device was fabricated atop a typical silicon wafer using the established techniques of DRIE and gold electroplating for interconnect formation. Of interest was the author's careful processing that allowed both the TE and vibrational comb harvester to be fabricated simultaneously. The TE device was constructed using Si, and as a result, its output was fairly low compared to other similar devices. The device output 2 mV across a measured temperature gradient of 75 K. Testing of the comb-type device showed its construction with gold electrodes had resulted in a lower resonant frequency (1.8 kHz) than similar devices constructed from silicon. While a unique approach, this combined device is

still in need of much further development before the claims made by the authors about the potential of a combined system can be substantiated.

A newer and less developed approach to micro-thermoelectric device construction was examined by Wang *et al.* The analysis of nanowire arrays via Bi_2Te_3 deposition has been shown to increase the Seebeck coefficient and improve the overall performance of the device [25]. Theoretical analysis indicated an opportunity to improve the ZT value of a TE by decreasing the width of the material to the nano-scale. As a result, the authors constructed an array of n-type and p-type Bi_2Te_3 nanowires by potentiastatically electrodepositing them on porous alumina substructures. One side of the substructure was coated with nickel for the purpose of attaching the nanowires. The opposing side was used for an electrode. The authors noted that the difficulty of this design was connecting the nanowires in series for maximum output. As the density of the wires was approximately 10^9 per square centimeter, the authors designed and fabricated multiple sections and insulators to break the nanowires into p-type and n-type zones. These zones could then make up the series connections that maximized the device output. Although actual testing of the device has yet to be undertaken, the authors expected this "film-like" TE to be merely 200 μm thick and capable of high voltage outputs over relatively small areas. If sucessful, this advance could make micro-TE devices far more competitive with other micro generators, however, there is a high cost associated with the complexity of the assembly and fabrication.

Another alternative construction technique for micro-TE devices was undertaken by Bottner *et al.* in their investigations of TE fabrication using MEMS thin film technology [26]. The authors noted that limitations on material and construction techniques failed to produce TE coolers that were capable of cooling 100 mW across low temperature gradients. Similarly, the authors noted an opportunity to produce a truly efficient and powerful micro-TE generator. The devices were fabricated atop a standard Si wafer by sputtering Bi, Sb, and Te atop pre-formed electrodes. This technique allowed the growth of both n-Bi_2Te_3 and p-

$(Bi,Sb)_2Te_3$ to a thickness of 20 μm. The power applied to the sputtering targets controlled the stoichiometry of the TE materials. This approach to TE material growth allowed the fabrication of devices with Seebeck coefficients that approached 160 μVK^{-1}. Photoresist was used as a mask for DRIE which refined the sputtered TE materials into the appropriate geometric shapes. To complete the TE device, silicon was attached to the top of the stack with pre-formed electrodes, similarly to the bottom. When used as a generator, the device output up to 3.5 μW of electrical power across a 9 K temperature gradient. Given the device size, this equates to .6 $\frac{W}{m^2}$ across a 5 K gradient. While this appears lower than other devices, it can be noted that this output was from a single thermopile. The authors noted this is actually more powerful than other values in literature when this is considered.

2.2.3 Cantilever and Beam Actuators

Actuator work has also been examined via cantilever devices. While some were designed for the use of translation only [27], others have been combined into intricate MEMS systems [28]. The work of Zheng *et al.* concentrated on the advantage and availability of thermal power to actuate CMOS-based cantilevers [28]. The cantilevers were fabricated from atop a silicon substrate and formed of a polysilicon layer with several metal layers being deposited atop this polysilicon base. Interspersed between the metal layers was a dielectric. An isotropic silicon etch was used in the final processing step to release the composite cantilever structure. The length of of the cantilevers was 300 μm and the width was about 10 μm. Integrated into the cantilever was a comb drive system that allowed the accurate detection of cantilever displacement. The metal layers of the cantilever also served as capacitance strips for the comb system mounted on either side of the actuator. The actuator was placed over an electric heater which caused the device to deflect. The maximum deflection of the cantilever was 24 μm given 17 mW of heater input. This corresponded to a temperature of 232 °C. The unique sensing system proved successful at measuring displacement to 8.8 nm.

A patent filed by Dhuler *et al.* explored a similar cantilever device that could respond due to thermal stimuli [29]. The invention proposal involved a cantilever comprised of thermally mismatched materials such that heating of the device would cause it to predictably deflect. In an interesting innovation, the inventors suggested the cantilever itself could contain a self-heating element. This element would be fabricated within the cantilever and the base of the cantilever would be electrically connected to a power source. Hence, electricity flowing to the cantilever would cause it to heat and subsequently deflect. This was an interesting variation as the device would act more like a piezo-based cantilever operating from applied electrical currents.

An additional unique cantilever actuator has been investigated by Gray and Kohl. This device not only deflected in a vertical manner as typical, but also "wiped" back and forth at the apex of its deflection [30]. This characteristic could be useful when considering electrical conduction and switch contact. The authors generated a model of the system (with multiple DOF) based on the use of the Euler-Lagrange equation. In this manner, they predicted the motion of the cantilever including both translational (vertical) and rotational (wiping) motions. The cantilevers were fabricated for the purpose of magnetic actuation in lengths of 500 to 1000 μm in length. Lithographic patterning of ferromagnetic materials created the beams themselves which were released from a ceramic substrate via thick photoresist release layers. To allow translational and rotational motion, they were attached to a substrate by dual, 30 μm high hinges 200 to 300 μm in length. Application of a magnetic field caused the actuators to reach their maximum vertical deflection within 1 ms, depending on the magnetic field. The longer devices showed the greatest disposition to rotate when at their peak deflection (due to hinge and cantilever flexibility). Rotation was accomplished by changing the amount and orientation the magnetic field once beam and substrate contact had been achieved, causing the unique wiping motion. Maximum vertical deflection was about 130 μm with an applied magnetic field of .14 Tesla. Maximum wiping deflection was about 50 μm at .07 Tesla. The authors asserted that wiping motion of this type should

prolong the life of permanent electrical contacts by continually cleaning them.

Work by Zhang *et al.* has also concentrated on electromagnetic micro-actuation via cantilever displacement [31]. The device examined by the authors consisted of a cantilever beam that was free at both ends and fixed in the center to a cross-ways torsional beam. The beam was attached at either end to the substrate. At both ends of the cantilever, a magnetic plate was attached and rested above a planar electrical coil fabricated on the substrate. As such, the activation of the coils could cause the cantilever to swing toward or away from the coils similar to a teeter-totter. Fabrication of the device was based on UV-LIGA techniques and a large sacrificial photoresist layer. The entire system of components were fabricated from a single substrate with the photoresist providing spacing as different components were fabricated and etched. Finally, the cantilever was released by removal of the photoresist layer, producing the unique setup. Testing of the cantilever showed it capable of 17 μm of deflection and capable of switching (or rotating about the torsional beam axis) within 20 μs when a driving frequency of 15 Hz was applied. The authors asserted that use of a cantilever setup such as this one could be an effective and controllable electric switch or relay depending upon its use.

Also working on the promise of magnetically driven micro-cantilevers was the work by Wright *et al.* who developed an actuator capable of a 200 μN clamping force [32]. Designed for electrical relay connections, the device was constructed using 500 μm thick silicon with a nitride coating as a substrate. On the front side of the substrate, metal electrodes were fabricated and the electromagnetic coil (which caused deflection) was plated. A photoresist sacrificial layer was used to create spacing between the coil and the deposited permaloy that made up the cantilever itself. Removal of the photoresist released the permaloy cantilever over the fabricated coil. Several different gaps between the cantilever and coil were considered, the maximum being 50 μm, the minimum being .5 μm. A simple model was created to predict the performance of the device and results agreed well with actual testing. Given a

coil current of 24 mA and 19 mW, the cantilever (1000 μm long) was deflected a total of 4 μm. Although the device produced 200 μN of force, the authors contend it capable of force in the mili-Newton range given an 800 μA coil load.

The use of piezoelectric cantilevers has also been investigated. Jeon *et al.* studied the use of MEMS-based piezoelectric cantilevers for the purpose of micro gripper fabricaiton [33]. In this work, two cantilevers were fabricated to serve as the dual sides to the gripper. Fabrication proceeded above standard silicon substrates with a silicon-nitride film deposited to a thickness of 1.2 μm. Bottom and top electrodes of platinum and titanium were deposited via standard methods to a thickness of 200 nm. Sol-gel multicoated PZT was deposited to a thickness of 1.2 μm above the electrodes and the entire material stack was etched using a combination ICP-RIE (inductively coupled plasma-reactive ion etch) process. At this point, the authors produced some cantilevers with only the silicon-nitride supporting substrate, while others were left with the full silicon substrate in place. The size of the cantilevers was 1 mm in length, 100 μm in width. The cantilevers that were released from their silicon substrate curled significantly as a result of residual stress in the PZT film. Those that remained atop the silicon substrate did not exhibit the same curling characteristics, however, were not able to attain high displacement values. With the cantilevers fabricated, they were placed in a jig with a foot print of 6.5 mm by 5.5 mm. With an applied voltage of 5 V, the released cantilevers achieved about 53 μm of deflection while the unreleased cantilevers displaced about 5 μm. In the jig, the cantilever setup proved capable of holding a small metallic ball of 100 μm diameter given 7 V input. The authors concluded that a setup like this one could be useful in the areas of handling biological cells where precise movement and control is a necessity.

Because of the applicability of piezo-based cantilevers to a wide variety of applications, work by Baborowski specifically targeted the fabrication techniques necessary for the PZT layers that underpin these devices [34]. Work by Zhang *et al.* combined not only research into

advanced materials processing, but also the application of that research into a real cantilever device [35]. Like many other piezoelectric cantilevers, the work by Zhang *et al.* involved the deposition of PZT on a substrate to form the micro cantilever. However, recognizing the need for a low-stress substrate, the authors used a .5 μm thick layer of silicon nitride and $Zr0_2$ which was released to form the cantilever. The $Zr0_2$ layer was used due to the limitations of PZT deposition on silicon nitride films. The released cantilever structures were tested for resonant frequency primary modes. Given a length of 180 μm and width of 100 μm, the measured resonant frequency was 13,750 Hz. Reducing beam length to 100 μm increased the natural frequency to about 40,000 Hz. The maximum tip displacement of a cantilever with a length of 280 μm was found to be 30 μm. The authors noted that the largest expected displacements would occur when the cantilevers were operated at their respective resonant frequencies.

This work by Zhang *et al.* was extended by Gross *et al.* who stepped not only the fabrication of the device forward, but also directed its use for a microswitch [36]. The authors noted that typical MEMS switches that require fast switching times are based on electrostatic actuation. However, these switches also require a higher actuation voltage (50 V) and electrostatic operation is known to be non-linear. Hence, the authors fabricated and tested additional cantilevers for the purpose of electrical switching. Using actuation voltages of 30 V, they were able to achieve switching speeds of 1-2 μs with a 30-dB isolation between on and off states when operated at 100 MHz.

A device developed by Conway *et al.* combined features common to cantilever actuators for the purpose of developing a high-force, large displacement device [37]. The device was created by using SU-8 to form beams that responded to a thin-film PZT strip. The PZT strip was located centrally and caused the flexure of the surrounding SU-8 beams. Via mechanical advantage, the beams were capable of amplifying the original force and displacement of the thin-film PZT. The overall scale for the device was about 500 μm by 550 μm . The device

was fabricated atop an $Si0_2$ substrate. Next, platinum and titanium were patterned to serve as one electrode for the PZT. The PZT was deposited in a sol-gel process, then patterned. A top layer of Pt/Ti was deposited and patterned atop the PZT to serve as the top electrode. Finally, the SU-8 was deposited and patterned into the flexing, amplifying system tested by the authors. The authors found this actuator capable of producing 55 μN with a peak deflection of 1.18 μm given 10 V applied to the PZT.

Lai *et al.* developed an actuator that, like work by Conway *et al.*, relied on amplification of displacement and force to attain a final useful result [38]. Two systems of actuators were employed, each connected at the top by a platform that was actuated. Each actuator system was constructed of several leaf-like assemblies that expanded and contracted similar to a car jack. The leaf assemblies were constructed of 25 μm thick nickel foil. The leafs were linked by a larger center beam of nickel foil to form the overall jack-like appearance. Movement of the device was accomplished by thermal heating. The different thickness of the beams caused vertical motion as the device was heated (via applied DC) and the entire structure lifted. The authors noted some tendency for the thin leaves of the structure to buckle when the applied current became too high and the temperature gradients too harsh. The maximum displacement of the assembled actuator was 44 μm while the maximum recorded force was about 200 mN. Overall, the authors noted a vertical displacement equivalent to at least 4 % of the actuator height and a maximum power consumption of .2 W.

2.3 Micro Engines

In addition to MEMS-based actuators, micro engines are also being developed that operate on a wide variety of thermodynamic cycles. PowerMEMS devices that operate from both internal combustion and external combustion sources are reviewed. The internal combustion cycles reviewed here include a gas turbine (Brayton cycle) engine [39], a Homogeneous Charge

Compression Ignition Free Piston (Otto cycle) Engine [40], and a micro rotary internal combustion (Otto cycle) engine [41]. External combustion devices include the development of a Rankine cycle steam turbine [42]. One commonality between these competing cycles is they are traditional macro-scale cycles, reproduced on the micro-scale.

2.3.1 Internal Combustion Engines

There have been several approaches to micro Brayton cycle engines. Chief among their differences is the method of fabrication. Isomura *et al.* built compressors and combustors based on 5-axis micro milling technology. This allowed the fabrication of a 10mm diameter device from a titanium alloy material [43]. Bearings in this type of engine have received much attention due to the very high speeds that must be tolerated. Herringbone grooves were cut into the titanium alloy shaft of the device and the engine proved capable of speeds up to 566,000 RPM. While this was a notable accomplishment, to achieve the proper compression ratio across the compressor, future speeds must achieve 870,000 RPM. When operating as designed, the authors contended the combined system should be able to produce upwards of 100 W of electrical power.

By contrast, others who have worked on micro-Brayton cycle engines employed fabrication techniques more compatible with standard IC chip design. Work by Epstein *et al.* produced a 2 cm diameter engine based on the DRIE of silicon wafers [4, 39]. As with the work by Isomura, certain considerations were addressed due to the high-speed rotation of the devices. These included the stability of the rotating masses themselves, the life-span of the bearings, the fluid flow into, around, and out of the device, and the dynamics of the system at high speeds. Epstein also noted that costs of high-volume production must be addressed (hence the attraction of DRIE silicon wafer construction versus the approach by Isomura). Epstein further noted that at high speed operation, there exists the issue of resonant excitation.

Research found several frequencies in the bandwidth of operation that excited the bearing setup or the rotor itself. The mechanical difficulties of these devices was further compounded by the effect high speeds had on the thermodynamics, specifically, on the oxidation of fuel in the combustor. The combustion process in these engines was critical to their performance and power density. The speed of fluid flow into and out of the combustor effectively limited the time that was available for combustion to occur and as a result, much work concentrated on the stabilization of the fluid flow (and hence the flame).

The Brayton cycle is only one of several that have been adapted to MEMS devices. Using Homogeneous Charge Compression Ignition, (HCCI), a cycle that approached the Otto cycle was investigated in the form of a free piston engine. An HCCI free piston engine (FPE) was investigated by Aichlmayr *et al.* to address flame quenching effects characteristic of internal combustion on the micro scale [5, 44]. As noted by Aichlmayr, significant obstacles exist for combustion in a MEMS engine of any type related both to the kinetics (or speed of flame propagation) and the interaction of that flame with the walls of the combustion chamber. This interaction results in cooling of the flame, or quenching. HCCI introduces a pre-mixed fuel/air mixture into the combustion cavity which ignites due to the compression supplied by the piston, similar to a diesel engine cycle. A key difference, however, is that the combustion event occurs uniformly throughout the combustion cavity similar to an Otto cycle engine. Aichlmayr argued this approach addresses quenching issues as HCCI removes the flame front from the combustion event found in a typical spark-ignition engine. Findings related to the combustion development of the HCCI FPE found that good fuel conversion efficiency in the device could be achieved using a lean mixture at the expense of power density. Additional modeling indicated a pre-heated fuel/air mixture could also improve operation of the HCCI cycle, again at the expense of power density. When operating as intended, the engine could be capable of producing 10W of output power in the form of compressed air. The problem of flame quenching remains a common theme among the internal combustion cycles on the micro-scale.

A similar approach used a sliding piston translating within a combustion chamber [45, 46]. The engine design was dual-ended such that the cylinder had combustion occur on both ends. As a result, the piston translated back and forth within the cylinder. The exhaust was located mid-way between the two ends and, similar to a two-stroke macro-scale diesel, was uncovered when the piston passed beneath it. The authors quickly realized the inherent challenges of combustion on the micro-scale and devised a simple combustion model to aid in the development of their engine. The model was used to analyze and verify the operation of the actual micro engine that was constructed. The fuel/air mixture was introduced into the combustion chamber and ignited via spark ignition. Over the course of one million cycles, the electrodes were found to degrade substantially. The authors found the total burned fraction, or combustion efficiency, of the device to be about 60 %. Also noted, the need to maintain at least a 2 mm combustion chamber height to limit flame quenching behavior. Further increasing the problem was assumed poor sealing around the piston which not only aided poor combustion efficiency, but also gave the piston a lower than expected velocity of travel (reported as 10 cm/sec).

Further investigation of the Otto cycle on the micro-scale has been pursued by multiple groups in the form of Wankel rotating engines. The attraction of the Wankel engine as a PowerMEMS device can be traced to the fact that the internal components of the engine can be viewed as largely two-dimensional. Lee *et al.* designed one such engine [6]. This two-dimensional geometry enabled production based on photolithography and other available micro-fabrication techniques. As noted in the development of the FPE, however, significant design challenges existed with respect to combustion. As an attempt to recognize at least part of the Wankel design, an SU-8 expander was designed and fabricated to expand liquid CO_2 and turn a rotor as a result. The principle design feature absent in this SU-8 based expander was the compression chamber necessary for combustion to occur. Based on this simplified expander only design, the device was found to output up to 12 W at 17,000 RPM. The development of the combustion Wankel engine is underway using nickel as the primary

fabrication material. The final product is expected to be a centimeter scale device that is about 3 mm thick.

Development of a Wankel engine by Fu *et al.* progressed beyond an initial centimeter scale engine [47, 48]. Fabricated parts from silicon wafers produced using batch processing techniques allowed a millimeter scale device to be assembled. This research sought to produce a device that could output between 10 and 100mW. As is the case with macro-scale Wankel engines, however, this micro-scale Wankel suffered from sealing at the rotor apexes. The clearances required for consistent operation proved difficult to attain with the precision achievable from current fabrication techniques. Due to the problems of the micro-scale device, a larger centimeter scale device was altered to perform as a compressor which could be placed in a meso-scale refrigeration cycle.

2.3.2 External Combustion Engines

Rankine Cycle Engine

In contrast to the internal combustion cycles, the use of the external combustion Rankine cycle has been investigated as a PowerMEMS alternative. Frechette *et al.* reported that an expected 1 to 12W of power could be generated by a Rankine steam cycle engine. The engine described was constructed of DRIE silicon wafers with a surface area size of 1.5 cm^2 and thickness of 1.5 mm [7, 49]. As with the Brayton cycle engines, the turbine used was a multi-stage device designed for maximum expansion. Rotational speed was a determining factor. The shaft and journal bearings necessary for implementation of the turbine were similar in nature and requirements to those of the Brayton cycle and hence, were designed with similar considerations in mind. Design of a pump for the cycle focussed on a spiral groove design due to the low Reynolds numbers of the micro-scale flow. In addition to the

bearings, limitations of the Rankine cycle device included the need for small evaporators and condensers that must be fabricated on the micro-scale. An apparent advantage, however, was the reduction in temperatures in the expansion turbine as compared to the Brayton Cycle device. Frechette noted the need to control unwanted heat leakage between components of this integrated system. Thin walls of SiO_2, a less-conductive material, placed as boundaries between components provided adequate insulation.

Organic Rankine Cycle Engines

The engines discussed in literature to this point have operated on modified macro-scale engine cycles. Essentially this has resulted in engines that operate across temperature gradients which are not highly removed from their larger counterparts. One area of macro or meso-scale engine development with interesting micro implications is work on devices that operate across small temperature gradients. Engines that operate from an Organic Rankine Cycle (ORC) have the promise to fill this niche.

Yamamoto *et al.* developed a working model and experimental hardware for a meso-scale ORC engine [50]. Like most ORC systems, their work focussed on the adaptation of a standard Rankine cycle setup to operate across low temperature gradients through the use of alternative working fluids and redesigned turbo-machinery. The device modeled and constructed by Yamamoto *et al.* operated with a turbine inlet temperature of about 80 °C. The turbine was desgined to have an outer radius of about 40 mm and shown to have an efficiency of 70 % at 22000 RPM. The turbine was connected via shaft to a torque meter and tachometer to monitor performance. A pump was used to increase the pressure of the working fluid between the tank supply and evaporator. The evaporator was designed with two 10 kW electric heaters instead of low-grade heat sources to facilitate better control and ease of use in this initial system setup. After heating to saturated conditions, the working

fluid was allowed to expand in the turbine and then cooled via a shell-type heat exchanger before returning to the supply tank. Two working fluids were considered and tested in the device, namely, water and HCFC-123. HCFC-123 was shown to be the preferred fluid due to its reduced temperature boiling point. The system achieved an overall efficiency of 1.25 % operating with HCFC at its best point. Heat input via the evaporators ranged from 10 to 14 kW for the case of the HCFC-123, however, water required increased heating and 17-20 kW was used. At 13 kW with HCFC-123, the peak output from the turbine was 150 W with a rotational speed of 35000 RPM. Peak torque output from the turbine was measured to be about .15 Nm with a heat input of 14 kW. The authors concluded that the initial outputs from the setup show the viability of operating an ORC from a low temperature heat source. The ability to attain 20 kW from waste heat, however, may pose significant challenges.

Work by Hung focussed on developing an ORC model that examined several different working fluids suitable for low temperature operation [51]. Among the fluids considered were Benzene, Toluene, p-Xylene, R113, and R123. Through the use of the model, the irreversibility of the system was studied when operating with the various working fluids. Key to the system irreversibility was the operating temperature of the evaporator as compared to that of the surrounding environment. As a result, fluids operating at higher temperatures showed increased system irreversibility. Inlet turbine pressures ranged from zero to 3.5 MPa dependent on the fluid under consideration. Operating temperature of the evaporator was 400 to 500 K for most test conditions. The findings of this study indicated that the use of the refrigerants was generally a better choice to reduce irreversibility of the evaporator. However, operation using any of the $C_{6+n}H_{6+n}$ compounds was expected to produce higher overall power output and better overall system efficiency (if the increased temperature of the evaporator could be maintained from the external heat source).

Similar to work by Hung, modeling by Liu *et al.* examined the operation of an ORC setup using several different working fluids and evaporator heat source temperatures [52]. The

authors noted that the presence of the hydrogen bond in some molecules (water, ammonia, and ethanol for example) could produce "wet" fluid conditions and may be unsuitable for ORC systems. "Wet" fluids were designated as those with a T-s curve whose slope was negative on the right hand side as compared to "dry" fluids which show a positive T-s slope. The use of dry fluids was noted to reduce the potential for turbine blade droplet impingement as they remained superheated after isentropic expansion and outside the saturation dome of the fluid. The authors also noted the ability of increased operating temperature gradients to drive improved performance, which is not terribly surprising.

2.4 Micro Thermal Switches

In addition to engines and actuators, a review of micro-scale heat transfer technologies is also included. In general, heat transfer devices fall into one of two groups: devices like heat-pipes that operate in an always"on" state or a class of devices that, like a thermal switch, operate in either an"on" or "off" heat transfer mode. There are many different implementations that all seek the same final result: good "on to off" heat transfer ratios.

2.4.1 Mechanical Thermal Switches

Electro-mechanical thermal switches operate on the principle of electrostatic attraction. Electrostatically actuated MEMS thermal switches have been developed for spacecraft thermal control by Slater *et al.* [53]. In space, the primary method of heat rejection is via radiation, hence, electrostatic actuation has been employed to turn active radiation surfaces on and off. The design of this radiation type thermal switch consisted of a radiating surface that could be brought into contact with a hot surface. An applied electrical voltage was used to bring the surfaces into contact and start heat transfer across the device. Separation of the

two surfaces turned the switch off. This separation distance also determined the necessary voltage to attract the two surfaces together. Fabrication relied on a combination of surface and bulk machining techniques. Slater aniostropically etched a silicon substrate to form a large membrane. This membrane served as the radiator that deformed to contact the hot base surface when voltage was applied. The radiator was coated with a high-emissivity paint to improve heat rejection to the surroundings. This design proved only minimally effective, however, due to poor contact between the surfaces, and hence, poor heat transfer.

Similar to the work by Slater, work by Beasley *et al.* produced a similar radiation type thermal switch [54]. This design also relied on an electrostatically driven radiation membrane that was coated with high-emissivity paint. The use of a polymer support was employed to provide supporting structure to the radiating membrane. This support maintained the determined gap distance between the heat source and membrane when the switch was in the off position. Beasley noted the need to minimize actuation voltage while maintaining robustness of the radiating membrane as an inherent design tradeoff. Further, an electrically insulating layer needed to be applied to one of the surfaces to prevent shorting when the surfaces are brought into contact. This layer increased the stiffness of the device and resulted in higher actuation voltages. Like Slater, the device fabricated by Beasley produced only minimal heat transfer. Many of the problems were the result of poor fabrication and issues with the high-emissivity paint. Future work on these radiative-type devices will concentrate a great deal in these areas.

The use of electrostatic operation is not unique to the radiative type switches. Electrostatic attraction was also employed by Hilbert *et al.* in the development of a thermoelectric MEMS cooler [55]. Their device provided cooling through the use of thermoelectrics in conjunction with electrostatically actuated switches. The design was such that the switches provided temporary contact between the cold-sink of the thermoelectric and the hot surface needing to be cooled in a cyclic application. The design provided a cyclic electrical pulse to the

coolers that coincided with the thermal switch actuation. In this manner, efficiency of the coolers was maximized. Fabrication of the device consisted of micro-machining to create the thermal switch out of thin metal contact strips, a dry metal contact type, and suitable electrical connections for the coolers. An improvement in the operation of the coolers and system as a whole was shown (although not quantified). Optimization work that was left to be done included the determination of correct switch sizes, materials, best actuation voltages, and timings.

Closely related to the work of Hilbert *et al.*, is that of Ghoshal [56]. In a US Patent Ghosal described a similar arrangement where pulsed power was provided to peltier coolers and "multiple selectively enabled thermal switches." In this scenario, MEMS electrostatic switches provided the conduction paths between the T.E. coolers and the hot and cold sides of the device to be cooled.

Work on a thermal switch has been described by Weiss *et al.* [57]. An array of mercury micro-droplets mounted above a heat exchanger make and break contact with a second membrane, thus turning heat transfer on and off in this design. 30 μm diameter gold targets were fabricated via photolithography on a silicon die. The gold targets were arranged in arrays of 1600. The preferential deposition of mercury vapor onto the gold targets produced an array of mercury micro-droplets. It was shown that the thermal resistance ratio, R_{on}/R_{off}, of the switch approached 50 when operated in an air environment over a distance of 400 μm. Heat transfer in the "on" state of operation was shown to improve with contact force, requiring .1 N of force to achieve a thermal resistance of about 1°C/W. Work on this switch by Christensen *et al.* predicted and demonstrated the ability of the micro-droplets to deform and increase in contact area as force was applied [58]. For the same .1 N load applied to achieve 1 °C/W in thermal resistance, the droplet contact area was shown to increase to about 32 μm.

The switch investigated by Weiss *et al.* was further developed by Cho *et al.* by integrating a unique cantilever setup for the switch translation [59]. In this setup, the thermal switch (similar to the one used by Weiss *et al.*) was mounted to the tip of a piezoelectric cantilever. The cantilever was sized such that its resonant frequency was around 100 Hz. By careful operation of the piezoelectric cantilever, it was found that the power requirement could be reduced to 7 μW at 100 Hz operation. This was due to the cantilever operation at its natural frequency. This result proved the conclusion drawn by others working on cantilever devices: operation at resonant frequency requires less electrical input (as noted by Zhang *et al.*, Section 2.2.3). The peak to peak operation of the cantilever switch was measured to be 400 μm.

Similar to the work of Cho *et al.* is that of Fang *et al.* who developed a model of a proposed cantilever system capable of translating many hundreds of μm with low applied power [27]. The authors noted this system could be used for many different types of switching. In essence, the authors described a system of cantilevers that used mechanical advantage to achieve large deflections. The system was named a "piezoelectric folded cantilever microactuator," or PFCM. In their conception, two parallel cantilevers were fixed to a level surface, then the end of each were attached to a second parallel cantilever that was fixed only to the first cantilever. This produced a "U" shape of parallel cantilevers. Connecting two of these U shapes together created a two-level PFCM. Attaching a third parallel cantilever fixed only to the second, created a three-level PFCM. Modeling by the authors suggested a three-level PFCM could generate up to four times the displacement of a single cantilever. Given a cantilever length of 2 mm, the expected maximum deflection of a three-level system would be 100 μm. The authors did not predict the power requirements for this PFCM.

A complete integrated cooling system was investigated by Darabi *et al.* By combining several MEMS devices, the authors constructed a singular system incorporating a micro pump, evaporative heat transfer, and temperature monitoring [60]. The authors noted that the

expected heat generation of future microprocessors is expected to dissipate over 1000 $\frac{W}{m^2}$, and hence, the need to develop systems capable of removing excess heat from electronic components is great. The cooling system was constructed using typical MEMS fabrication techniques with an overall size of 5 mm by 50 mm. Unlike typical construction techniques, however, a quartz substrate was selected due to its low thermal conductivity (of 1.5 $\frac{W}{mK}$ versus 100 $\frac{W}{mK}$ for a silicon substrate). A platinum heater was then fabricated on one end of the substrate to simulate the heat supplied via a micro-processor. Also patterned during this process were long and thin (20 μm) platinum electrodes. These electrodes served as the basis for the electro-hydrodynamic effect the authors used to pump fluid. In essence, one end of the device was immersed in R134a working fluid, and the opposite end was heated via the patterned platinum heater. A high voltage was applied across the electrodes and fluid was moved across the heated substrate in a thin film. The evaporation of the working fluid provided the cooling of this system. The authors noted that the primary means of cooling at lower heat fluxes was via conduction to the working fluid, which returned to the reservoir via gravity once pumped past the heat source. In this manner, the device behaved similarly to a standard heat pipe. At higher input heat fluxes, however, evaporation and even boiling was noted. The peak convective coefficient achieved by the device was about 20 $\frac{kW}{m^2K}$ when 30 $\frac{W}{cm^2}$ were applied via the platinum heater. As a concluding note, the authors suggest that their device may in fact, "pave the way for practical utilization of thin-film evaporation in many applications."

While thermoelectric (TE) devices were previously discussed in their form of power generation on the micro scale (Section 2.2.2), research has also been conducted into their potential to provide cooling [61]. Noting a need to maintain positive temperature control on high-power LEDs, Cheng *et al.* proposed a TE which could control an LED junction temperature to below 125 °C. Two n-type silicon wafers were used to construct the micro-TE. Using standard fabrication techniques (including the deposition of an insulating $Si0_2$ layer), the wafers were sputtered with titanium and copper which was then patterned to serve as the

electrodes for the TE. SU-8 channels were fabricated between the patterned Ti/Cu to confine the placement of the TE legs atop the electrodes. Solder paste was deposited atop the electrodes and Bi_2Te_3 "legs" were placed in the SU-8 defined channels (atop the paste and electrodes). The two silicon wafers were brought together as a sandwich, and using a hot plate and the reflow process, the construction of the device was completed. Tests of the constructed device showed a minimum temperature capability of 11.5 °C with an input current of .75 A.

2.4.2 Non-Mechanical Thermal Switches

A final area of thermal switch development consists of switches that define their on or off states without any mechanical actuation or contacts. Included in this group was a switch proposed in a U.S. Patent by Slasky to use liquid crystal [62]. Slasky suggests a device consisting of an electrically insulated volume that may be filled with liquid crystal and contacted with isolated electrodes to provide the necessary voltage to drive the switch performance. The applied voltage would align the crystal parallel to the electrodes and turn on heat conduction. While an interesting idea, much has yet to be proven on the actual capabilities of a switch of this type. However, the non-mechanical nature of the switch makes it intriguing.

Design of a switch by Smith *et al.* focussed on the adsorbtion and desorption of a conductive gas between concentric cylinders [63]. The design of the device utilized concentric cylinders that had an annular gap of .1 mm between them. The gap was filled with ^3He and exposed to an activated carbon layer that resided in a small portion of the gap. Gap conductivity was changed by applying or removing a heat load (via resistive heater) from the activated charcoal. This caused the ^3He to be ad or de-sorbed. This effectively altered the conductivity of the gap. Limitations of the device were size and operating frequency. The authors claimed a "quite quick" desorption rate of the gas when heat was applied to the activated carbon

to turn the switch on. However, achieving a full "off" could take as long as ten minutes. Nonetheless, on to off ratios of approximately 100 times were achieved.

2.5 Microscale Wicking

A review of micro-scale wicking through square channels is presented. Work on capillary wicking design was conducted by Whalen [64]. In this work, square SU-8 structures were used to form wicking channels. These channels allowed capillary force to continually re-wet the membrane with fluid. The position of fluid along the channel length was described as a function of time by Equation 2.1.

$$x(t) = \sqrt{t}\left[\frac{\sigma(2h_0 + w)cos(\theta) - \sigma w}{4\pi\mu}\right]^{\frac{1}{2}} \tag{2.1}$$

x(t): distance of wicked working fluid
σ: surface tension of working fluid
μ: dynamic viscosity of working fluid
θ: liquid - solid contact angle
t: time
h_0: wicking channel height
w: wicking channel width

The SU-8 channels described in this work were 10 μm high by 10 μm wide. They were used to provide a thin layer of liquid atop a silicon membrane.

In addition, correction factors were proposed for volumetric flow in a rectangular duct [65]. Kim *et al.* noted that the typical hydraulic radius for flow in a non-circular pipe can be approximated in a circular pipe by Equation 2.2.

$$R_h = \frac{2A}{P} = \frac{WH}{W+H} \tag{2.2}$$

A: cross-sectional area
P: wetted perimeter of the non-circular duct
W, H: width and height of the channel

The correction factors offered by the authors for capillary driven flow in square or rectangular channels is given by Equation 2.3.

$$R_{h,cor} = C_f R_h \tag{2.3}$$

C_f: correction factor

where

$$C_f = \frac{2}{3}\left(1 + \frac{H}{W}\right)^2 F_p \tag{2.4}$$

F_p: duct shape factor

Hence, the authors showed it is possible to use relatively straight-forward equations for the case of modeling capillary flow in non-circular ducts. The authors also suggested correction factors for flows that were not capillary driven, but instead driven by pressure gradients acting across the channels.

2.6 Membrane Deflection Calculations

A review of deflection calculation of square membranes is presented. Work by Vlassak and Nix created models to predict the deflection of thin membranes of square or rectangular shape [66]. For square thin-films, the authors offered the deflection as stated in Equaiton 2.5

$$w = w_o \frac{1}{a^4} \left(a^2 - x^2\right) \left(a^2 - y^2\right) \left[1 + \frac{R}{a^2} \left(x^2 + y^2\right)\right] \tag{2.5}$$

a: half membrane side length
x, y: cartesian coordinates within membrane
R: determined experimentally
w_o: center-point deflection
w: membrane deflection (at position x,y)

The authors further noted that based on the potential energy of the membrane, a more simple form may be determined for the centerpoint deflection as shown in Equation 2.6.

$$w_o = f(\nu) \left(\frac{qa^4(1-\nu)}{Et}\right)^{\frac{1}{3}} \tag{2.6}$$

q: pressure applied to membrane
ν: Poisson's ratio
$f(\nu) \approx .800 + .062\nu$
t: membrane thickness
E: Young's Modulus

The double integration of Equation 2.5 or Equation 2.6 along the membrane edges then yields the volume beneath the deflected membrane.

Chapter 3

Fabrication

Just as there has been great advance in the design and development of micro power systems and MEMS devices, there has been parallel development and advance in the fabrication processes that support these devices [67]. Unlike larger scale systems, MEMS devices have a unique ability to be batch fabricated using many of the techniques developed by computer chip manufacturers over the past decades. This not only makes them inherently flexible because of their small size, but also attractive because of their low cost of production on a per unit basis [68]. Because of these production and design advantages, the engines and thermal switches constructed for use in this work rely heavily on micro-fabrication and batch fabrication techniques. Many of these techniques are similar to work in the IC chip industry, however, the specific needs of the engine and switch have mandated the development of new fabrication processes specific to their design. This section describes the fabrication necessary to create the components used by the engine and thermal switch.

3.1 Silicon Substrate Preparation

At the heart of every engine and thermal switch component is the silicon substrate from which it is fabricated. The basic preparation of the silicon substrate is relatively simple, however, several processing steps are involved. The substrate wafer used in all cases is a standard three-inch diameter <100> wafer. Both sides are polished to facilitate the fabrication steps that are necessary for engine and switch component manufacture. The thickness of the silicon wafer is approximately 400 μm, however, variance of up to $\pm$ 25 μm is typical [64]. While potentially concerning for some applications, this has little impact on the construction of engines and thermal switches for these tests. The wet etching techniques used in membrane fabrication nullify any small irregularities in wafer thickness.

The first processing step for the base wafer involves the growth of a High Temperature Oxide (HTO) SiO_2 layer on both the wafer front and back sides. A wet oxidation is used to speed the process of oxide growth [67]. Wafers are placed in a furnace at 1100 °C for 120 minutes to grow an oxide thickness of 500 nm. Once the oxide layer has grown, the back side of the wafer is masked using semi-conductor tape. The wafer is then submersed in a 10:1 Buffered Oxide Etch (BOE) solution for 15 minutes. This effectively removes the oxide on the front side of the wafer and prepares it for the boron diffusion process. As described in Section 3.6, boron doping provides an etch stop for the wet etchants used in the fabrication process. This etch stop (boron layer) determines the final thickness of the membrane being fabricated.

The boron diffusion process begins by placing the wafers (with oxide layer removed on the front side) parallel to boron-nitride disks. The front side of the wafers are each placed within 2 mm of the boron disks. Next, the temperature of the wafers and boron disks are elevated to 1125 °C and maintained at that temperature for 110 minutes. This process results in a boron layer of 2.2 μm on the topside of the wafer. Although in proximity to the boron disks, the back side of the wafer remains uneffected due to the 500 nm thick $Si0_2$ mask. Figure

3.1 shows the basic cross-section of a silicon wafer following the HTO and boron doping processes.

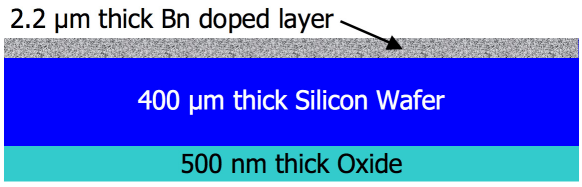

Figure 3.1: Si Wafer Cross-section with HTO and Boron Doping

After boron diffusion, several additional processing steps are necessary to complete the substrate wafer. The boron diffusion process leaves a layer of borosilicate glass atop the wafer which interferes with successful future processing steps [69]. To remove the borosilicate glass, the wafer is immersed in BOE for fifteen minutes. After BOE, a Low Temperature Oxide (LTO) layer is grown on the wafer. Like HTO, the LTO process is a wet oxide growth step. The wafer is heated with oxygen and water vapor to a temperature of 850 °C for 60 minutes. This lower temperature oxide growth is used to prevent the boron layer from continuing to diffuse through the wafer. Continued diffusion would reduce the concentration of the boron doping and the effectiveness of the boron layer as a wet etch stop (Section 3.6). After LTO, the wafer is again stripped of any oxides by re-immersion in BOE for 10 minutes.

At this point in the process, the substrate wafer is clean and ready for further processing steps, however, the boron layer proves to be problematic because of its ability to electrically conduct. To insulate the boron from any patterned electrical devices, a final LTO is grown on the wafer to a thickness of 80 nm by repeating the LTO step a second time. Finally, the substrate wafer is ready for processing steps that can manufacture it into engine or thermal switch components. Figure 3.2 shows the substrate cross-section in this final form.

The thickness of the doped layer is important for consistent membrane production. This process typically produces thicknesses within ± 10 nm [67]. This equates to only .5 % of the total thickness of the layer.

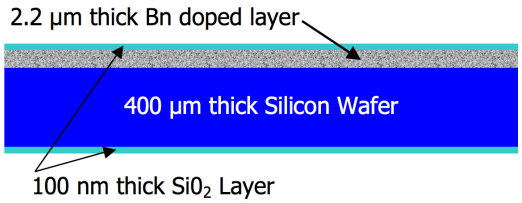

Figure 3.2: Fully Processed Silicon Substrate Wafer

3.2 Photolithography Process

The photolithography process described in this section is a standard process common to the fabrication of many of the engine and thermal switch components. The result is a patterned polymer layer atop the membrane surface which serves as a mask for future processing steps. The resolution of the patterns created by this photolithography process is about $\pm$ 1 μm. Photolithography begins by the spin-coating of hexamethyldisilazane (HMDS) which is an adhesion layer. The HMDS solution is spun at 3000 RPM for 30 seconds. Following HMDS deposition, AZ5214-EIR photoresist is spun onto the wafer at 3000 RPM for 30 seconds. After spinning, the wafer is placed on a hot plate for one minute at a temperature of 110 °C.

After baking, the photoresist is ready to be patterned by selective exposure to UV light in a positive process [69]. To achieve the desired pattern, masks are used which allow exposure of the AZ5214 in areas where it must be removed. Typical exposure to UV light is about 14 seconds. Many different types of masks are used based on the desired photoresist pattern. In this manner, the photoresist that remains on the wafer becomes an effective barrier to further processing steps.

After UV light exposure, the photoresist is developed using a 1:4 solution of AZ400K developer and DI water. The wafer is agitated in the developer solution for 45 seconds to completely pattern the photoresist. Figure 3.3 shows a positively patterned cross-section of the photoresist on the basic substrate wafer. Removal of the photoresist layer is performed by exposure to acetone.

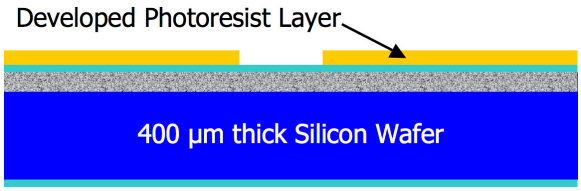

Figure 3.3: Developed/Patterned Photoresist Layer

3.3 Gold Deposition and Etching Process

The gold deposition and etching process is also common to the fabrication of many different engine and switch components. Gold deposition on silicon wafers is done via DC sputtering in a two-stage process. First, titanium-tungsten (TiW) is sputtered to a thickness of 5 nm. This is followed by a deposition of gold which can vary in thickness from 300 nm to 500 nm depending on intended use.

After sputtering is complete, the wafers are patterned by first spinning and developing photoresist as described in Section 3.2. Many different masks and patterns are created depending on the desired end use of the wafer. Figure 3.4 shows a simple cross-section of photoresist patterned over a thin layer of gold.

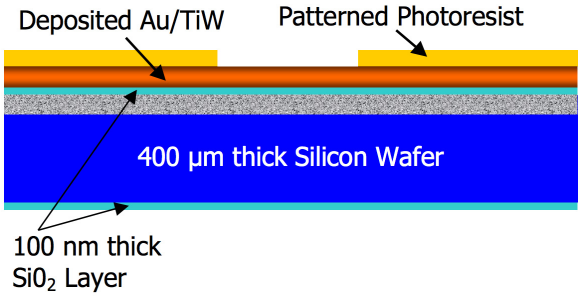

Figure 3.4: Patterned Photoresist over Gold Layer

With the photoresist mask in place atop the sputtered gold, the wafer is placed in a TFA gold etch solution and agitated until all of the exposed gold has been removed. Next, the exposed TiW layer is removed via 45 seconds of agitation in hydrogen peroxide. Figure 3.5 shows the etched gold and TiW layers atop the standard silicon wafer.

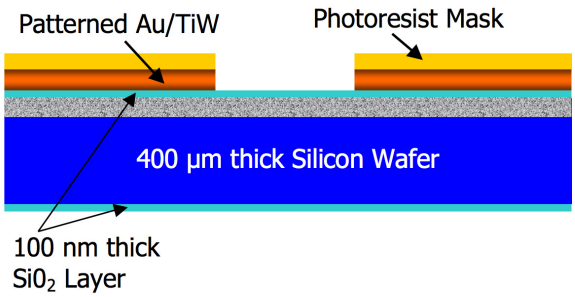

Figure 3.5: Patterned Gold and TiW

3.4 Engine Components Fabrication

There are two basic components that go into the construction of a micro-engine. The first is a lower membrane which serves as the evaporator and lower bound to the engine cavity. The second is the top membrane which is the primary expansion and work output membrane. The top membrane also serves as the top bound to the micro-engine cavity.

3.4.1 Top Membrane Fabrication

There are two distinct types of upper membranes used in micro-engine operation. The first is a standard 2.2 μm thick silicon membrane that is directly fabricated from the basic wafer substrate. The second type is a 300 nm thick silicon-nitride membrane that is fabricated using an alternative process.

Silicon Top Membrane

In the case of the silicon top membrane, fabrication begins using a standard substrate wafer that has been prepared as described in Section 3.1. Photoresist is spun on both sides of the wafer as described in Section 3.2, however, only the back side is patterned using an oxide mask similar to the one in Figure 3.6. Figure 3.6 shows the mask for 5 mm membrane

creation, a similar mask is used for 10 mm membrane fabrication.

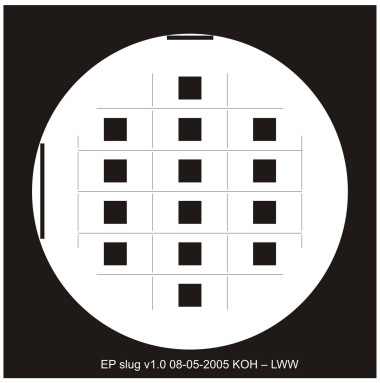

Figure 3.6: 5mm Membrane Oxide Mask

After patterning, the wafer is placed in BOE for ten minutes to remove the oxidation layer in areas patterned by photolithography development. By leaving the top side unpatterned, the BOE does not remove any oxidation on the wafer top side. Oxidation removal exposes the base silicon and readies the wafer for wet etch as described in Section 3.6.1. After etching the wafers are ready for dicing and use in micro-engines. Figure 3.7 shows the effects of photolithography patterning and subsequent BOE exposure to the wafer backside.

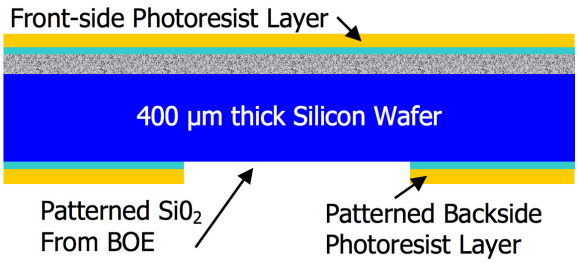

Figure 3.7: Wafer Cross-section after BOE

Silicon Nitride Top Membrane

Unlike the silicon top membrane, the silicon nitride top membrane does not start with a standard boron doped base wafer. Instead, a 300 nm layer of SiNx is deposited on both sides of a <100> wafer via an LPCVD process [69]. Photoresist is again used to define

a membrane pattern on the back side of the SiNx wafer as described in section 3.2. The pattern used is the same as that shown in Figure 3.6. Using the patterned photoresist as a mask, etching of the backside SiNx is performed by a CF_4 reactive-ion etching process until the base silicon is exposed as defined by the photoresist pattern.

This process prepares the SiNx wafer for wet etch and membrane creation, however, an additional step of gold deposition and patterning on the wafer top side is needed. This is done because of the minimal thickness of the SiNx layer as well as the desire, in some cases, to monitor the temperature of the top membrane. The SiNx membrane after wet etch is too thin to effectively reflect the laser in the standard laser vibrometer setup (Section 5.2.1). Because of this, the top side of the wafer has 300 nm of gold deposited and patterned as in Section 3.3. The pattern in Figure 3.8 is used to pattern the gold into 1.3 mm dots at the center of each 5 mm membrane (a similar mask is used for 10 mm membranes). These dots serve to reflect the laser vibrometer signal and allow the determination of membrane deflection.

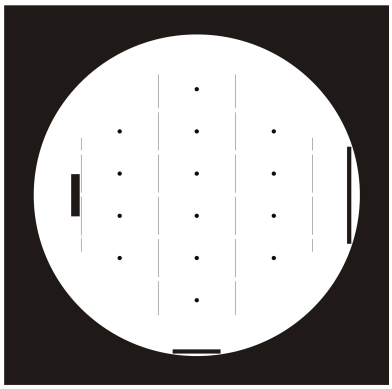

Figure 3.8: Gold Dot Pattern for 5 mm SiNx wafers

To fabricate silicon-nitride top membranes to monitor temperature, an RTD pattern is incorporated with the reflective dot shown in Figure 3.8. Figure 3.9 illustrates this combined pattern used on some 10 mm SiNx membranes.

Figure 3.9: Combined Pattern for 10 mm SiNx Membranes

After fully processing the front side gold pattern, the wafer is ready for wet etch and silicon nitride membrane creation as discussed in section 3.6.2. After etching, the membranes are diced and ready for use in engine operation.

3.4.2 Evaporator Membrane Fabrication

Fabrication of all evaporator membranes begins with a standard substrate wafer as described in Section 3.1. Gold is deposited via sputtering on both sides of the substrate wafer to a thickness of 500 nm on the wafer backside and 300 nm on the wafer top. 500 nm of gold on the wafer backside is necessary to serve as the etch mask during the wet etch process. After gold deposition, photo resist is spun onto both sides of the wafer to serve a dual purpose. First, the photoresist can be patterned into the desired mask to allow for effective gold etching as described in Section 3.3. Second, it is of utmost importance to protect the deposited gold from accidental removal during any of the fabrication steps. Consider that the gold etch process will effectively remove any gold not masked by photoresist. As such, patterning of one side of the wafer could accidentally lead to gold removal on the opposite unless the photoresist is used as a protective layer. Because of this, the photoresist, patterned or unpatterned, is left on both sides of the wafer until all gold processing steps are completed.

Standard Evaporator Membranes

After photoresist has been spun onto the wafer, backside patterning is performed using one of two masks. For 8 mm evaporator membrane creation, Figure 3.10 is used in a process described by Section 3.3. 5 mm evaporator membranes can also be patterned using the mask shown in Figure 3.6.

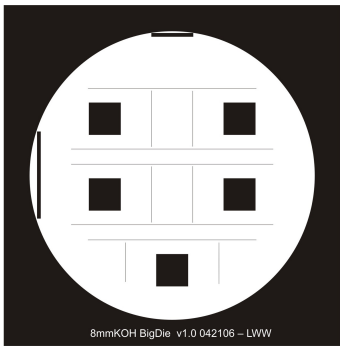

Figure 3.10: Oxide Mask for 8 mm Evaporator Membranes

After removal of the gold and TiW layers, the wafer is emersed in BOE for 10 minutes to remove the exposed oxide layer and reveal the base silicon. This prepares the wafer for wet etch as described in Section 3.6. Figure 3.11 shows the wafer cross-section after completed backside patterning.

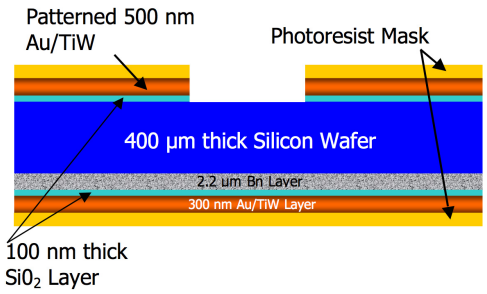

Figure 3.11: Patterned Evaporator Wafer Backside

With backside patterning completed, the front side gold is now patterned using the same photoresist that was spun in the initial fabrication step. Exposure to BOE does not alter its quality and because of this, it is used as the gold etch mask for the wafer top side. The gold is etched using processes previously described with a pattern that creates both an electrical heater and an outer RTD. Figure 3.12 illustrates the details of this dual heater and RTD design for an 8 mm evaporator membrane. Note that the top side mask used is aligned such that it matches the backside patterns already etched into the wafer.

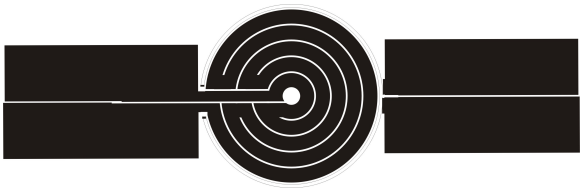

Figure 3.12: 8 mm Evaporator Membrane Heater and RTD Pattern

This produces a wafer with both sides now fully gold etched (with the backside experiencing an additional BOE step). The remaining photoresist is now removed from both sides via an acetone bath and the gold is annealed at a temperature of 650 °C for a duration of ten minutes. Figure 3.13 shows the wafer cross-section following photoresist removal and annealing.

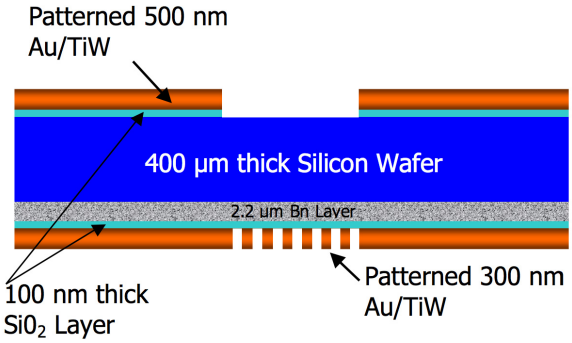

Figure 3.13: Fully Patterned Evaporator Wafer

After the gold is annealed, the evaporator wafer is ready to have wicks fabricated on its surface. Wicks are used to maintain a thin layer of working fluid atop the electrical resistance heater via capillary action. Wick design involves consideration of several factors and is

described by Equation 2.1. Two different wick geometries can be fabricated. The first consists of channels 90 μm in width and 10 μm high. These channels are delineated by 5 μm thick walls of SU-8. The second type of wick constructed uses similar 5 μm walls and 90 μm channels, however, is constructed to a height of 40 μm. The process of SU-8 deposition and patterning is discussed in Section 3.5. Figure 3.14 shows fully processed 40 μm high channels.

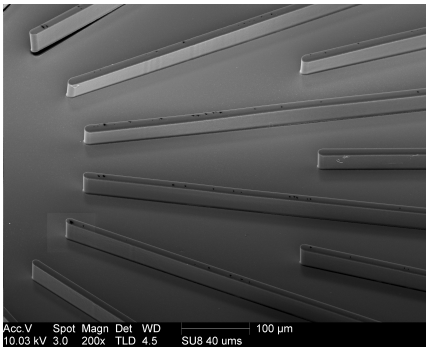

Figure 3.14: 40 μm High Wick Structure (courtesy T.Quy)

The SU-8 masks designed for use with these evaporator membranes are shown in Figures 3.15 and 3.16. In this design, SU-8 walls meet in the center of the evaporator to stiffen the membrane.

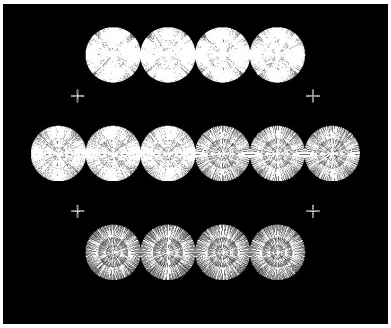

Figure 3.15: SU-8 Wick Mask

Figure 3.17 shows the completely patterned front side of the evaporator membrane with 40 μm high SU-8 wicks. Following these fabrication steps, the evaporator wafer is ready for the final processing step of backside wet etch to form the desired membrane structure (Section 3.6).

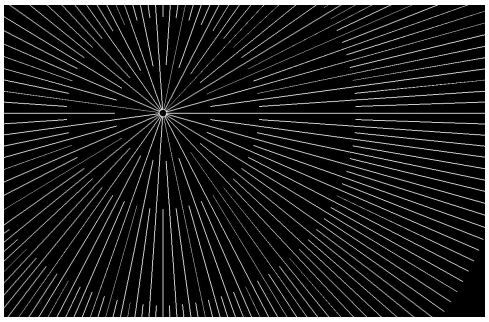

Figure 3.16: Center-Beam SU-8 Wick Mask Enlargement

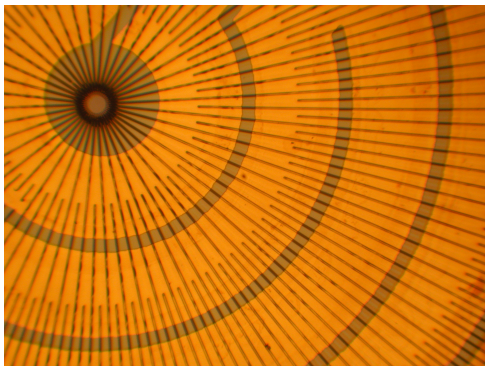

Figure 3.17: Patterned 8mm Evaporator Membrane, 40μm high Wicks

5 mm Heater and Dual RTD Pt Evaporator

On one rare occasion, a special 25 mm^2 evaporator membrane is used. Fabrication of this membrane is similar to those discussed to this point, however, platinum is used to fabricate the top side wafer patterns instead of gold. The process of platinum deposition and patterning is described in detail by Quy [70]. The mask used to pattern the platinum on the wafer top side is shown in Figure 3.18. Like the evaporator membranes patterned with gold, this design also uses a central resistance heater. Unlike the standard evaporator membranes, however, two RTDs are patterned concentrically around the heater. Once the wafer top and bottom sides are appropriately patterned and annealed, the wafer is ready for SU-8 wick deposition and wet etching to produce the final membrane.

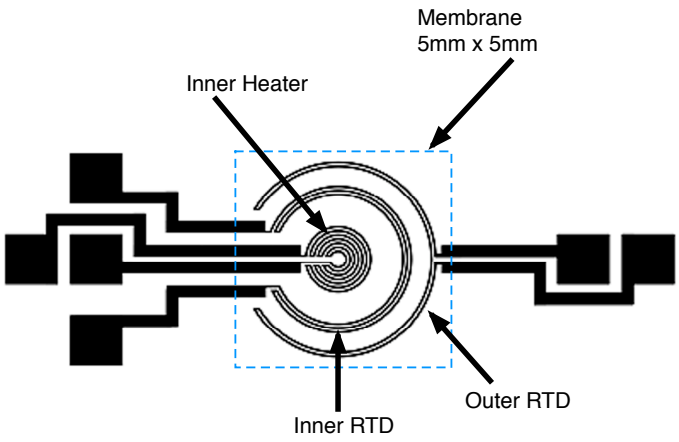

Figure 3.18: Evaporator Membrane Setup with Dual RTDs

9 mm Cross-Type Evaporator Membranes

Fabrication of 9 mm Cross-Type evaporator membranes follows the same fabrication steps as those for the 8 mm evaporator membranes. The cross-type membranes are unique in that instead of a single large membrane, the membrane is actually four distinct membranes of 4 mm side-length. Allowing for a .5 mm space between membranes, this creates an overall size of 9 mm. The oxide mask shown in Figure 3.19 is used to create the backside pattern for these membranes. Due to the increased size of the membrane, the front side of these 9

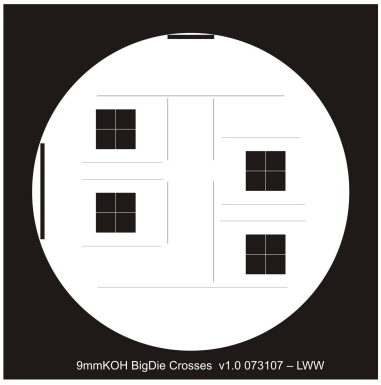

Figure 3.19: Oxide Mask for 9 mm Cross-type Evaporator Membranes

mm membranes is patterned using an alternative dual heater and RTD pattern as shown in Figure 3.20. As with the 8 mm evaporator membrane, the photoresist is removed after all

Figure 3.20: 9 mm Evaporator Membrane Dual Heater and RTD Pattern

gold etching is completed and the wafer is annealed at 650 °C for ten minutes. Figure 3.21 compares the structure of the 9 mm cross-type evaporator to the standard 8 mm evaporator membrane.

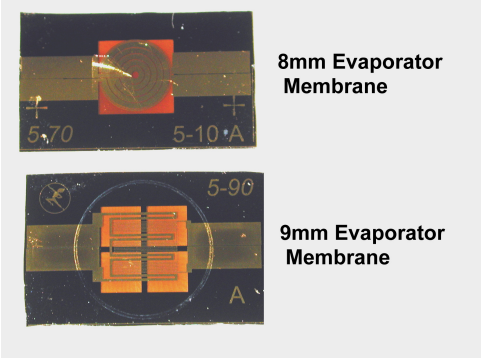

Figure 3.21: 8 mm and 9 mm Evaporator Membranes

After this processing has been completed, the wafer is ready for SU-8 application as described in Section 3.5 and wet etch as discussed in Section 3.6. The SU-8 wick patterns used are the same as those used for the 8 mm evaporator membranes. The fully patterned 9 mm evaporator is shown in Figure 3.22 with 10 μm high wicks. Only wicks of 10 μm height are used on 9mm cross-type evaporators.

3.5 SU-8 Deposition and Patterning

SU-8 is a robust, high-temperature capable polymer developed by MicroChem. SU-8 is selected for use on the evaporator membranes for a variety of reasons [64]. Among the most important is its ability to withstand the high temperatures attained by the electrical heaters. SU-8 is also capable of forming high-aspect ratio micro structures (14:1) in a procedure

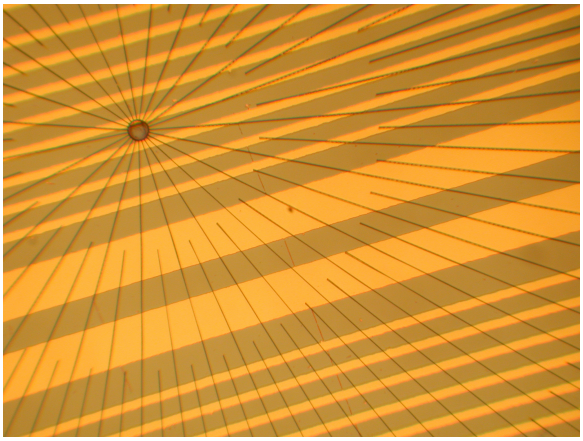

Figure 3.22: Fully Patterned 9mm Evaporator Membrane, $10\mu m$ Wicks

developed by Quy which is useful for the construction of the evaporator membrane wick structure [70]. Two types of SU-8 polymer are used. SU-8 2010 is used for wick structures with heights of 10 μm. SU-8 2100 is used for 40 μm high wick structures.

The deposition of SU-8 is done via spin-coating like photoresist, however, unlike photoresist its exposure and development is a negative process. The first step for either 10 μm or 40 μm high wicks is the spin-coating of Omnicoat as an adhesion layer. This is done at 3000 RPM for 30 seconds. After Omnicoat deposition, it is baked at 200 °C for two minutes. Next, SU-8 2010 or SU-8 2100 is spun and pre-baked using processes and specifications developed by both Carpenter and Quy [70, 71]. Following these guidelines, the SU-8 is exposed via UV light and then post-baked. With baking completed, the SU-8 is developed via agitation in MicroChem SU-8 developer. This leaves the desired SU-8 wicking structure atop the gold heaters and RTDs that have been patterned atop the evaporator membranes.

3.6 Wet Etching Techniques

Two types of anisotropic silicon wet etching are used as the final fabrication step in membrane creation. In the case of top silicon membrane fabrication, a mixture of ethylenediamine,

catechol, pyrazine and DI water (EDP) is used as the etchant. For all other membrane and switch component fabrication, a mixture of potassium-hydroxide (KOH) and DI water is used. EDP is used for top silicon membrane etching because of its ability to stop etching once in contact with the boron doped silicon layer in the wafer [69]. While the KOH is sensitive to the boron doped etch stop, it is not as sensitive as EDP. Because the top membrane of the engine is the work output membrane (and the calculated work output is directly coupled to the membrane pressure-deflection characteristics), repeatable fabrication is critical to top membrane fabrication. Variability in membrane thickness due to etch stop selectivity creates error in engine power output calculations.

Top membranes fabricated from silicon-nitride, are etched using KOH. Etch rates of SiNx by KOH are fully 1000 times slower than <100> silicon [67]. This produces a very predictable etch stop and hence, a repeatable fabrication step.

3.6.1 EDP Anisotropic Etching

The basic mixture for EDP is obtained pre-mixed from Transene Company, Inc. The EDP mixture is heated to temperatures between 105 and 110 °C and is ready for use. It should be noted that the etch rate is dependent on temperature. Because of this it is important to maintain the EDP at the prescribed 105 to 110 °C operating point [72].

The wafer to be etched is placed in a designated EDP holder and then submersed into the heated etchant for about six hours. EDP is a highly selective etch, preferring to etch the <001> plane of the wafer at a rate of about .75 μm/minute with a preference compared to the <111> plane of about 35:1 [67]. This results in "sloped," or non-vertical, sides to the substrate wafer behind the membrane as shown in Figure 3.23. The angle of slope is 54.7 °.

After etching through the plain silicon, the etch rate slows dramatically when the EDP comes into contact with the boron doped layer. This boron layer serves as an effective etch stop, allowing the reliable creation of membranes to the thickness set by the layer. The basic geometry of the membrane after EDP etching is shown in Figure 3.23. As the EDP etch step is the final step in membrane fabrication, the membranes are now ready to be diced from the substrate wafer and used in engine operation.

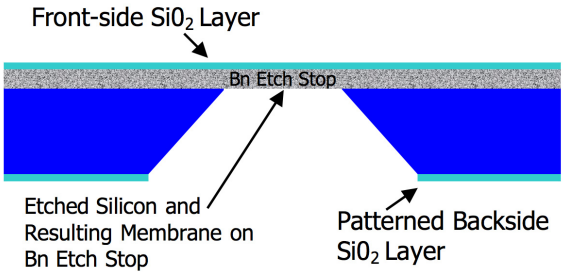

Figure 3.23: Si Membrane Creation Following EDP Anisotropic Wet Etch

3.6.2 KOH Anisotropic Etching

Like EDP, KOH is a highly selective wet etch used as the final fabrication step in membrane creation. KOH is mixed by the combination of 250 g of Potassium-Hydroxide dry pellets with 400 ml of DI water. It is then heated to a temperature between 70 and 80 °C and is ready for use.

The wafer is placed in a designated KOH holder and immersed in the etching solution for about 5.5 hours. KOH is highly dependent on temperature to control etch rate and care must be taken to monitor etching progress frequently. The backside gold that is used as an etch mask must also be of high quality. Poor gold adhesion and patterning on the wafer backside results in etching outside the exposed areas as the layer of gold lifts from the wafer surface. The benefit of KOH use, however, is that the wafer front sides remain unexposed to KOH vapor during the etch process. This is not true of the EDP process where slight

exposure to EDP vapor causes any SU-8 structures to lift from the top side wafer surface. Etching is completed when the bubbles that form on the etching surfaces slow and stop - indicating the KOH has finished etching the bare silicon and is now against the boron doped layer or the silicon nitride layer. Figure 3.24 shows a cross-section of the completely etched structure.

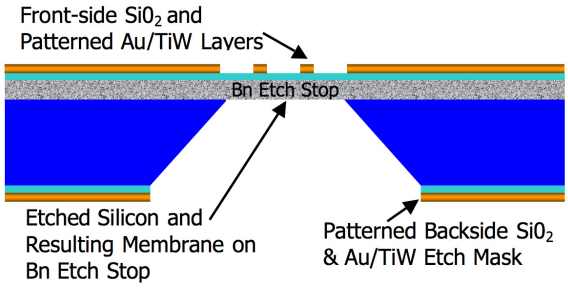

Figure 3.24: Si Membrane Creation Following KOH Anisotropic Wet Etch

Because KOH is highly resistant to etching silicon-nitride, SiNx serves as its own effective etch mask. After the RIE process and top side gold patterning, KOH is used to etch the wafer backside until the silicon has been removed. The etching rate slows (essentially stops) when it reaches the SiNx layer on the wafer top side. Figure 3.25 shows the resulting cross section after all fabrication steps have been completed and the wafer is ready for dicing.

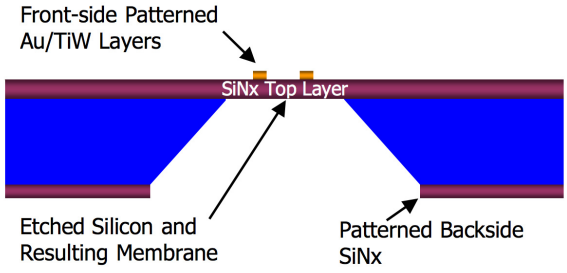

Figure 3.25: SiNx Membrane Creation Following KOH Anisotropic Wet Etch

3.7 Thermal Switch Fabrication

Many of the same techniques employed to create micro-engine components are also used to create the thermal switch. All switches start with the basic silicon substrate (Section 3.1) and, just as with evaporator membranes, gold is deposited on both sides of the wafer and patterned as described in Section 3.3. 500 nm is sputtered onto the wafer backside while 300 nm is sputtered on to the top side. The backside is patterned using the mask shown in Figure 3.26.

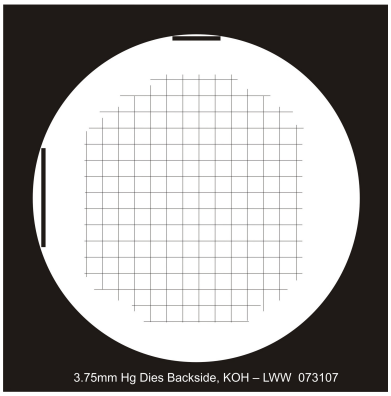

Figure 3.26: Backside Thermal Switch Die Mask

These lines prescribe the desired scribe lines that will allow the individual dies to be diced from the main wafer after wet etching. The front side of the thermal switch wafer is patterned to create 30 μm diameter gold dots or "targets" as described by Cho *et al.* [73]. After the gold has been patterned and the photoresist mask has been removed via acetone (Section 3.3), the gold patterns are annealed at 650 °C for 10 minutes.

Following annealment, a final photoresist layer is spun on top of the wafer. This photoresist is patterned such that small holes in the resist are opened around each gold target. This layer serves as a mask against accidental mercury deposition in areas of bare $Si0_2$ between targets. Figure 3.27 shows the top side of the switch die after this final photoresist spinning and patterning step.

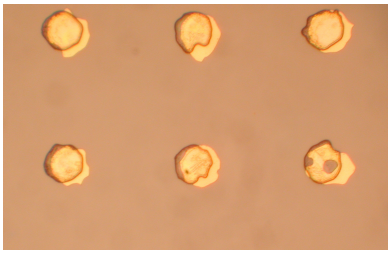

Figure 3.27: Patterned Thermal Switch Die

Next, the switch wafer is placed into a KOH bath and etched as described in Section 3.6.2. The KOH etches along the backside scribe lines and creates thermal switch die, ready for use as "dry contact" thermal switches (switches without mercury droplets) or exposure to mercury vapor when testing is done with "wet" thermal switches. The mercury deposition process is described in detail by Cho *et al.* [73]. In this process, mercury vapor preferentially condenses on the gold targets for one hour. The completed thermal switch with mercury droplets is shown in Figure 3.28.

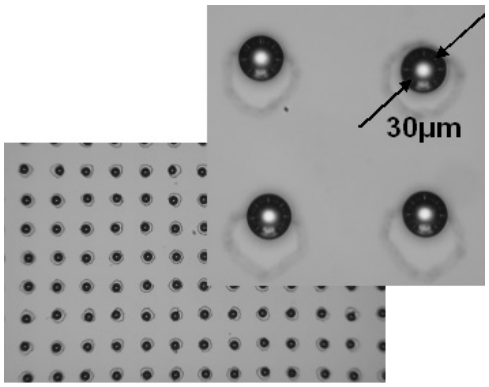

Figure 3.28: Completed Thermal Switch Die (courtesy J.Cho)

Chapter 4

Assembly

The assembly of the micro-engine and thermal switch presented in this dissertation is performed manually using fabricated components discussed in Chapter 3. The micro-engine is constructed using a lower evaporator membrane, a gasket, and a top expansion membrane. The working fluid is held between the two membranes. The thermal switch is assembled by placing a fabricated thermal switch die atop a constant temperature heat sink or source. The micro-engine and switch are then ready for operation as described in Chapter 5. A detailed look at engine and switch assembly is presented in this chapter.

4.1 Basic Engine Assembly

A cross-section of the fully constructed micro-engine is shown in Figure 4.1

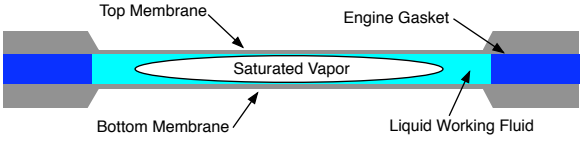

Figure 4.1: Basic Engine Cross-section

The three basic micro-engine components are the lower evaporator membrane, engine gasket, and top membrane. Key to the assembly of the micro-engine is the acrylic carrier. The carrier serves two functions. First, it provides a convenient way to safely handle assembled micro-engines. Second, it maintains a clamping force that seals the micro-engine together. A drawing of the basic carrier design is shown in Figure 4.2. Depending on the membrane sizes used in engine construction, the center access holes may be larger or smaller but retain the same locations. Appendix F shows detailed drawings of the acrylic carriers used during this work.

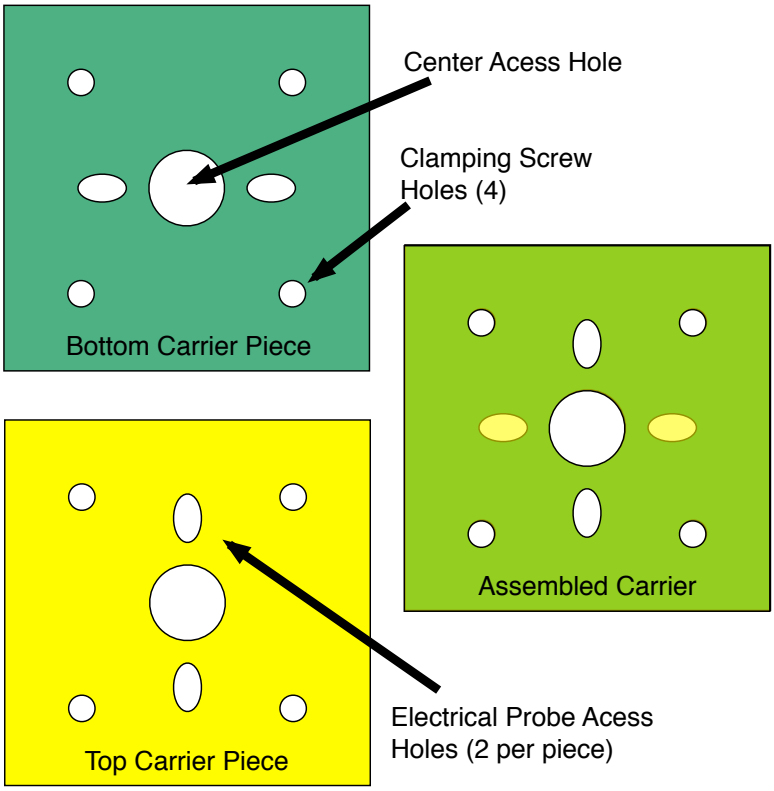

Figure 4.2: Engine Acrylic Carrier Pieces

The first step in micro-engine assembly involves placing an evaporator membrane over the central hole in the lower acrylic carrier piece. It is important that the membrane is centered above the hole so that proper alignment between thermal switch and micro-engine may take place (Section 5.2.1). The lower evaporator membrane is held in place with scotch tape as shown in Figure 4.3.

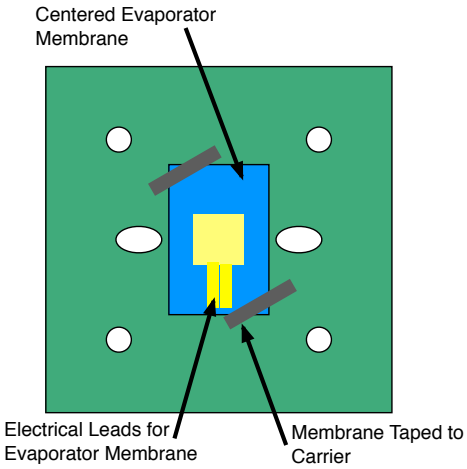

Figure 4.3: Mounted Evaporator Membrane on Bottom Carrier

Next, the cavity is fabricated and placed around the lower evaporator membrane. The cavity is constructed of gasket material made from semiconductor tape. The tape used has a thickness of 75 or 150 μm depending on the construction. The tape is cut via razor blade into a square section that surrounds the membrane outer edge. This is shown in Figure 4.4. Before placement, however, a layer of sealing grease is added to improve the micro-engine cavity seal. The grease used is a Radioshack heat sink compound (276-1372A) that is spread thinly across the area of contact with the gasket. Once in place, the top of the gasket is also treated with the compound for improved sealing.

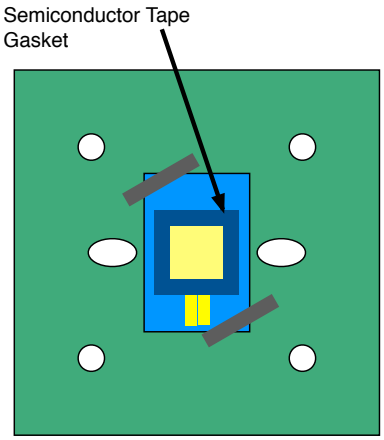

Figure 4.4: Mounted Gasket on Evaporator Membrane

With evaporator membrane and gasket in place, the top membrane is fixed to the upper carrier. It should be noted that between the top membrane and top carrier piece is a specially cut section of double-sided foam tape. This tape not only keeps the top membrane fixed to the top acrylic carrier piece, but also distributes the clamping load that results from assembly in the carrier. By evenly distributing the load, the seal is improved. Figure 4.5 shows views of the top membrane affixed to the top acrylic carrier.

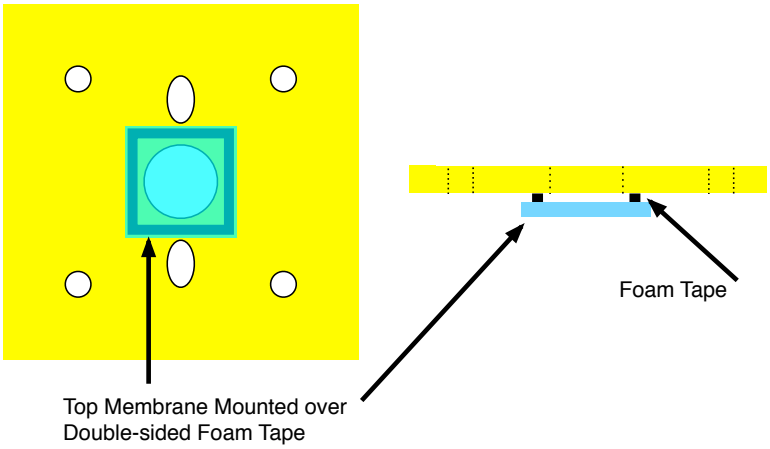

Figure 4.5: Top Membrane and Foam Tape

With the lower membrane, top membrane, and cavity in place, the micro-engine is ready for assembly. The actual process of assembly is fairly straightforward. First, bolts are placed through the bolt holes in the top carrier. These will serve as alignment guides, matching complementary holes and nuts in the lower carrier. After the bolts are in place, the cavity is filled to the top with working fluid.

The working fluid used in this engine is a combination of 3M^{TM} pf5060-dl and air. Air is present as a result of the assembly technique, but also due to the liquid dissolved gas content which can approach 50 % by volume [74]. After the cavity has been filled with working fluid, the two halves are brought together by lowering the top onto the bottom. When the top membrane contacts the gasket material and sealing compound, a seal is formed that encases the working fluid between the membranes. Care must be taken to obtain an

appropriate mixture of working fluid and vapor in the cavity. The micro-engine operates most efficiently when the primary means of mass transfer in the operating fluid is due to evaporation instead of nucleate boiling. To avoid boiling the working fluid, the liquid content is kept to a minimum. This is accomplished by gently lifting on one corner of the top carrier to temporarily break the seal between gasket and top membrane as shown in Figure 4.6. This releases working fluid liquid from the cavity and allows air and vapor to take its place. When enough fluid has escaped or evaporated, the top membrane is again seated on the cavity gasket. The goal for effective operation is a centrally located vapor bubble and a resulting liquid-vapor interface that is toward the edge of the cavity. Generally, a bubble that resides over 90 % of the cavity (by surface area) provides the best operating results.

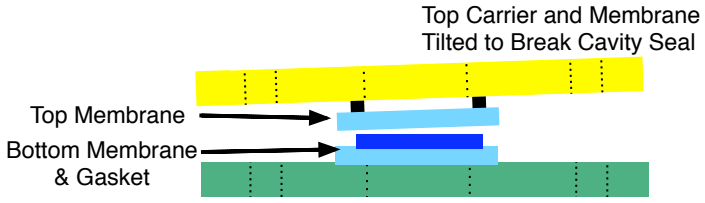

Figure 4.6: Tilted Top Carrier and Membrane

The final step in assembly is to engage the bolts, that were placed in the top carrier, to the nuts. This introduces a static clamping force that maintains effective cavity sealing and provides a robust carrier to handle the micro-engine. Figure 4.7 illustrates the fully assembled device within the carrier.

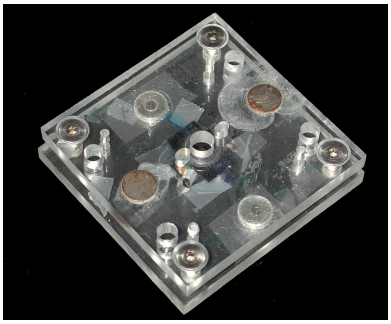

Figure 4.7: Fully Assembled Engine in Carrier

Figure 4.8 shows an interior look at a fully assembled micro-engine. The view is a top-down snapshot through the two membranes clamped between the carriers. Note the location of the liquid-vapor interface between the two membranes.

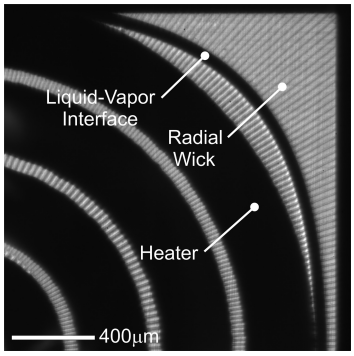

Figure 4.8: Assembled Engine. Courtesy S. Whalen

Finally, electrical contact is made with the micro-engine membranes via the insertion of electrical probes through the holes noted in Figure 4.2. These holes are designed to align precisely with the electrical leads that are patterned onto the membrane die during membrane fabrication.

4.1.1 Engine Assembly with Added Mass

In some situations, engines are assembled with an added mass on the top membrane. Figure 4.9 shows a cross-section of the engine with added mass. The procedure for placing mass on the top membrane is fairly simple, however, somewhat tedious.

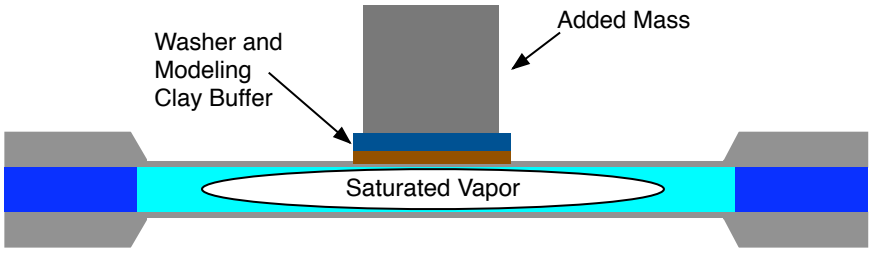

Figure 4.9: Cross-section of Engine with Added Mass

First, the micro-engine is completely assembled in an acrylic carrier as normal. It is important that the micro-engine be fully assembled so the mass may be added with minimum risk of top membrane failure. With the top membrane fully supported by the fluid enclosed in the engine cavity, it is less likely to fail when mass is added. The second step in mass addition is the placement of the buffer washer. The washer is placed on the top membrane first because it provides a solid platform for any subsequent mass. The lower side of the washer is evenly covered with a layer of modeling clay. The clay serves two purposes. First, the clay serves as a smooth surface without hard edges. Especially for engines assembled using SiNx top membranes, it is critically important to remove any possible hard edge that could shatter the membrane. Second, the clay is less conductive than the metal washer and added mass. This serves as an imperfect insulator between the engine cavity and heat sink of the applied mass. The buffer washer is then carefully lowered by hand onto the top membrane with a pair of tweezers. Care must be taken to avoid dropping the buffer washer onto the membrane as this will result in top membrane failure. Additional care must be taken to avoid pushing the washer onto the top membrane for the same reason. With buffer washer in place, the desired added mass may be positioned and placed atop the washer.

To obtain a laser-vibrometer signal from the top membrane/added mass, one additional step must be taken. A small piece of scrap wafer with gold on one side is placed atop the added mass to reflect the laser-vibrometer signal during testing (Chapter 5). This allows accurate mass deflections to be recorded.

4.2 Thermal Switch Assembly

Construction of the thermal switch is a simple procedure that places the fabricated switch die (Section 3.7) atop the constant temperature heat sink. This is accomplished by two different methods. The first involves a permanent bonding of thermal switch to heat sink.

In this method, a light coating of super glue is placed atop the thermal switch heat sink. The switch die is then carefully set on top. It can take several minutes for the die to completely adhere to the sink due to the smooth surface of the silicon. Figure 4.10 shows a schematic of the switch placed atop the heat sink.

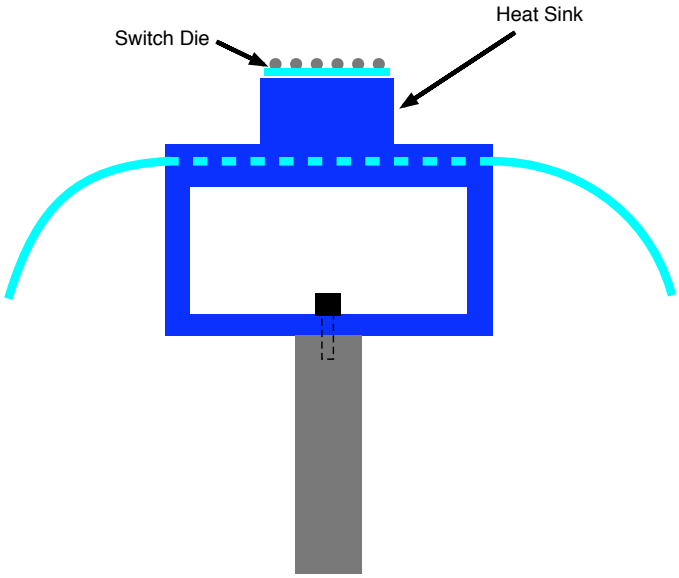

Figure 4.10: Thermal Switch Mounted Atop Heat Sink

In some testing, it is convenient to attach the thermal switch to the heat sink using a less permanent method. In these situations, Radioshack Heat Sink Compound is used to fix the switch in place and allow good heat conduction between switch and sink. The fully assembled micro-engine and switch is shown in Figure 4.11.

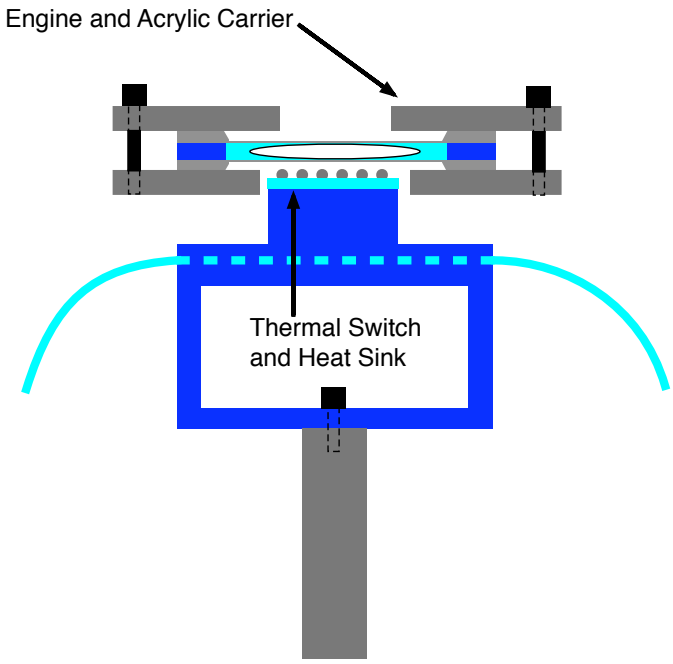

Figure 4.11: Fully Assembled Engine and Switch

Chapter 5

Experimental Methods

There are many different micro-engine operating modes and tests discussed in this dissertation. An important aspect to understanding the results presented is knowing the setups and calculations that serve as their foundation. This chapter examines the basic operating modes of the engine, the test setups that support them, and calculations that determine and model the engine operating characteristics. The calculation and measurement errors associated with these tests are discussed as well.

5.1 Basic Engine Operating Modes

As briefly discussed in Chapter 1, there are two basic modes of micro-engine operation. The first is a more simple sub-resonant operating mode. The second is engine operation at its resonant frequency. This section examines both operating modes in detail.

5.1.1 Sub-resonant Operation

The operation of the engine at sub-resonant conditions is relatively simple. First, an engine is assembled and aligned over a thermal switch as described in Chapter 4 and Section 5.2.1. The basic operation of the micro-engine involves heat input through the evaporator membrane and expansion of the working fluid within the engine cavity as a result. After expansion, the micro-engine cools and returns to its initial state. Figure 5.1 illustrates this operating mode.

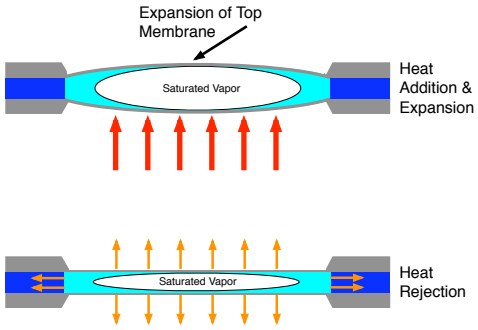

Figure 5.1: Engine Operation at Sub-Resonance

To help ensure enough heat is removed during heat rejection, a thermal switch is incorporated with many of the micro-engines operating at sub-resonance. It is translated into the evaporator membrane to intermittently conduct heat from the micro-engine. The various test setups in this chapter describe its operation while Chapter 6 specifically details its effect on engine operation.

Figure 5.2 shows the typical response of a micro-engine operated at sub-resonance versus time. The heat input, or heat addition, causes the top membrane to expand as a result of increasing cavity pressure. The heat rejection returns the micro-engine to its original state and readies it for the next heat addition.

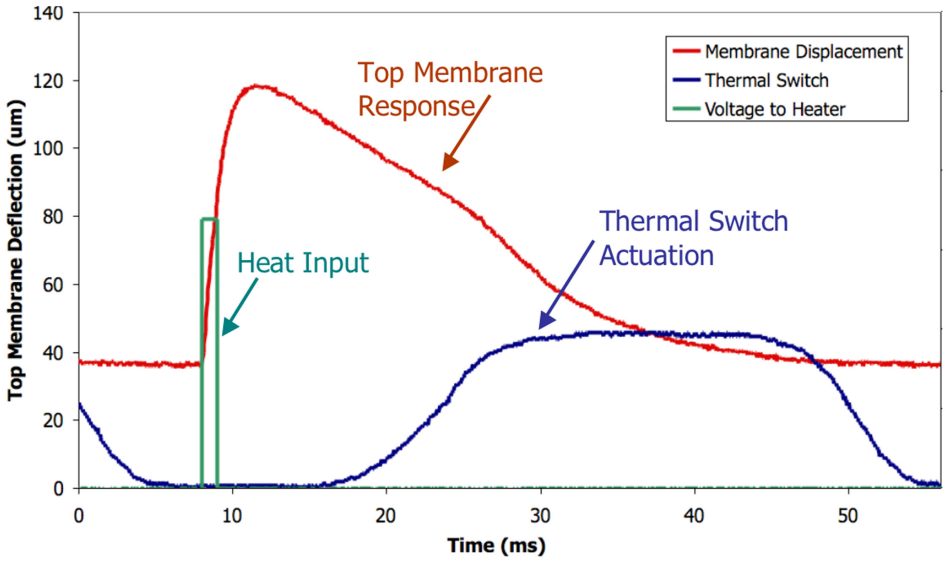

Figure 5.2: Engine Operation at Sub-Resonance

The basic pressure-volume curve for operation at sub-resonance is derived directly from the performance of the top membrane. A typical PV curve is shown in Figure 5.3. Details on the derivation and use of this curve to determine micro-engine performance are presented in Section 5.4.1.

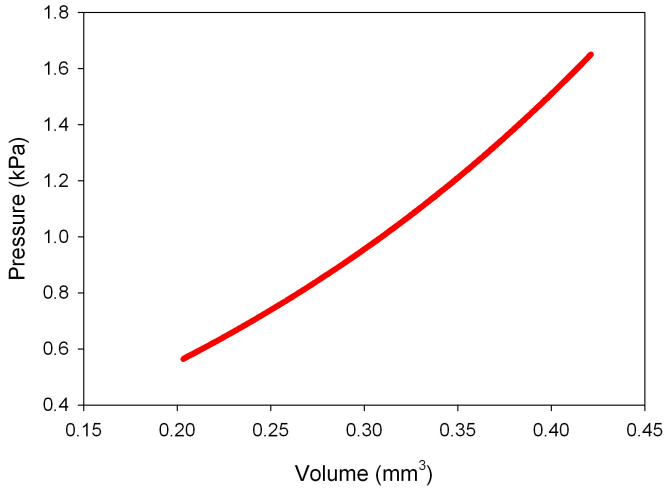

Figure 5.3: Typical P-V Plot for Sub-resonant Operation

5.1.2 Resonant Operation

Operation of the micro-engine at its resonant frequency is the second operating mode. This mode introduces compression into the expansion cycle noted during sub-resonant operation. Figure 5.4 shows the simplified micro-engine resonant cycle.

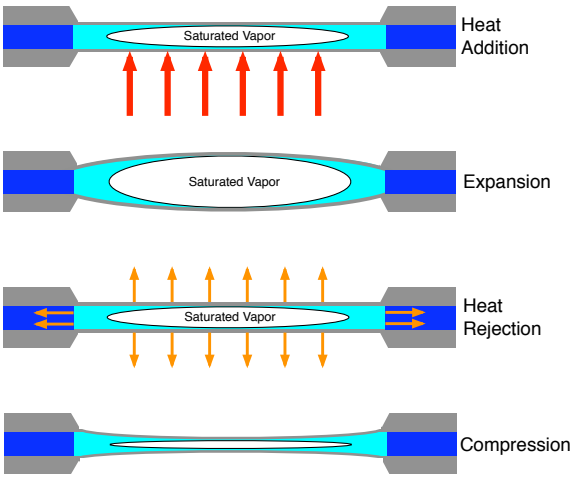

Figure 5.4: Engine Operation at Resonance

While the basic components of the micro-engine and switch are similar to those used in sub-resonant operation, some additional considerations are necessary. The natural frequency of a standard micro-engine ranges from about 500 Hz to 2 kHz depending on the components used. The key to achieving resonant operation is the reduction of the engine natural frequency to a more manageable 100 Hz where it can be successfully operated. The basic equation governing a system's natural frequency is given by Equation 5.1.

$$\omega_n = \sqrt{\frac{k}{m}} \tag{5.1}$$

ω_n: natural frequency
k: stiffness
m: mass

Using Equation 5.1 as a guide, the natural frequency of the engine can be lowered into a reasonable operating range by reducing micro-engine stiffness and increasing the engine mass. Because of this, only large engines are used in resonant testing. The selection of a large, 10 mm side-length, 300 nm thick SiNx top membrane reduces operating stiffness while the addition of a weight to the top membrane increases the overall system mass. The addition of mass to the micro-engine top membrane is detailed in Section 4.1.1. The natural frequency of an assembled micro-engine is checked by operating the device at sub-resonant speeds and monitoring the ring-out (or period between deflection oscillations) of the top membrane and mass. The size of mass used to achieve resonant operation ranges from 2.5 to 5.5 grams depending on the micro-engine. The key to successful resonant operation is matching the natural frequency of the engine with the performance capabilities of the thermal switch. In this work, micro-engines with resonant frequencies of about 100 Hz are assembled and tested.

During sub-resonant operation, the top membrane displacement is used to determine both pressure and volume characteristics for the micro-engine. During resonant operation, however, the pressure and volume are decoupled and must be measured independently. In this situation, the top membrane provides the volume of the micro-engine and the response of the lower membrane provides the pressure measurement. This is a critical step to determining the performance of the micro-engine at resonant conditions. Justification and verification of this pressure measurement technique is discussed in detail in Appendix E.

The deflections of top and evaporator membranes are recorded as described in Section 5.2.1. Figure 5.5 shows the operation of the electrically heated micro-engine at resonant conditions as a function of time. The evaporator membrane displacement is clearly operating out of phase compared to the top membrane displacement. This signals effective resonant operation. The lower membrane displacement in Figure 5.5 has been multiplied by a constant for comparison purposes.

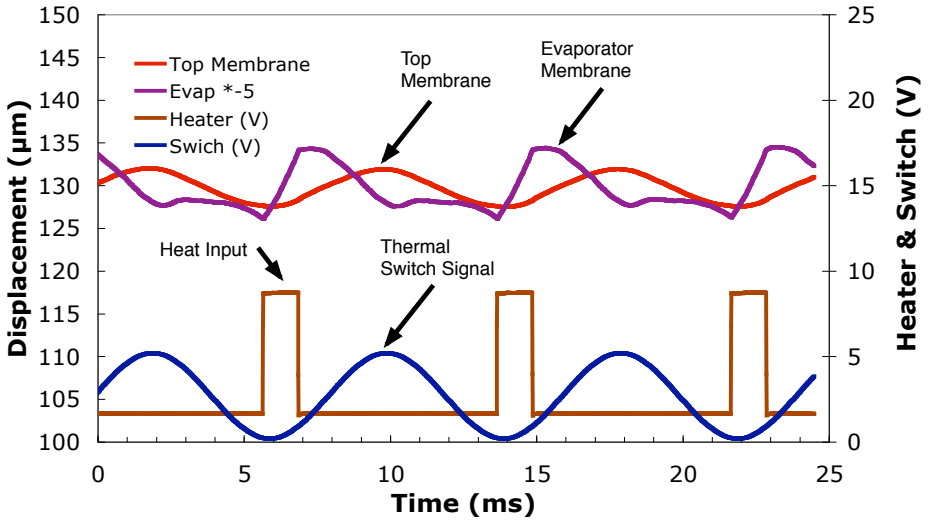

Figure 5.5: Resonant Operation of an Electrically Heated Micro-Engine

The conversion of these membrane deflections to pressure and volume are discussed in Section 5.4.2. A typical resonant cycle is shown in Figure 5.6. The four basic elements of heat addition, expansion, heat rejection, and compression are noted in the figure.

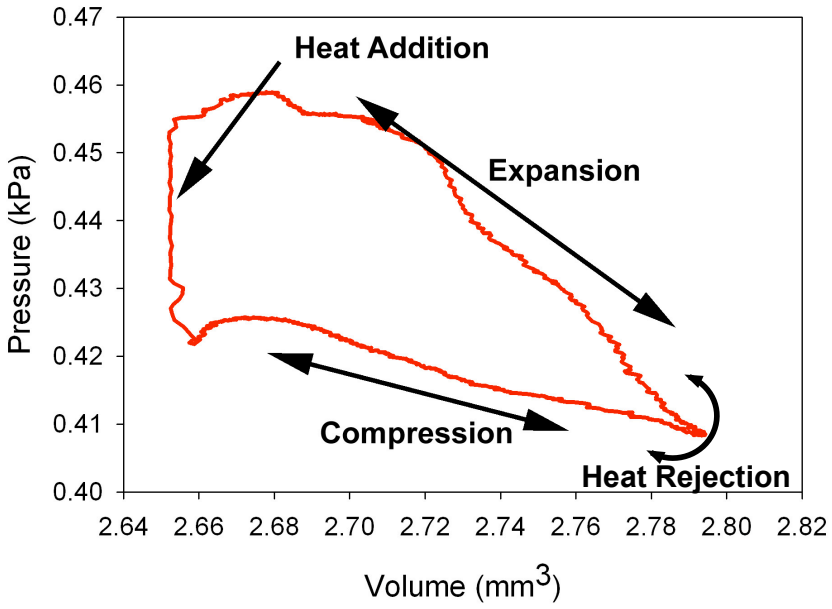

Figure 5.6: Basic Micro-engine Resonant Cycle

5.2 Engine and Thermal Switch Experimental Setups

The overall goal for each setup is simple: reproduce an environment to test the engine that is akin to the overall operational goals discussed in Chapter 1. There are several tests presented here including tests for both electrically heated micro-engines and those heated via thermal switch. Additionally, the setup for operation using two thermal switches (one to heat and the second to cool) is also discussed.

5.2.1 Electrically Heated Engine Operation

The electrically heated micro-engine with cooling thermal switch test is the most common used in these experiments. In this test, the micro-engine is constructed with standard components and housed in the standard acrylic carrier. The lower evaporator membrane is fabricated with a gold resistance heater so electrical power may be dissipated and the engine heated as a result. The micro-engine and carrier are visually aligned above the thermal switch. A schematic of this setup is shown in Fig 5.7.

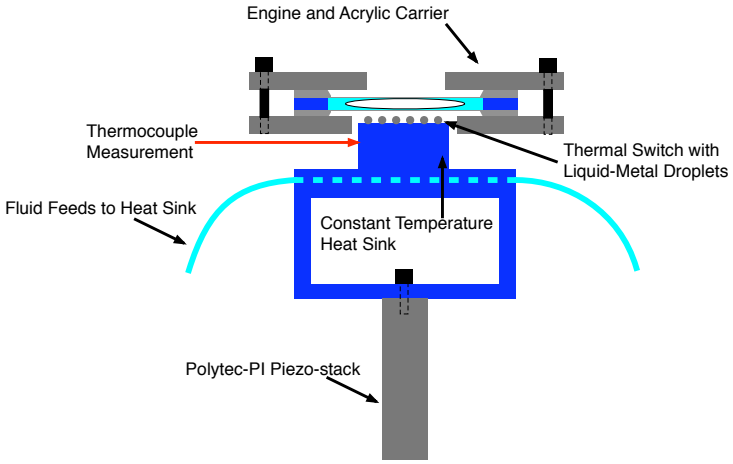

Figure 5.7: Assembled Engine and Thermal Switch

As noted in Figure 5.7, the micro-engine rests above the thermal switch which is attached

to a constant temperature heat sink. The entire switch and sink are mounted above a piezo-stack manufactured by Polytec-PI. Two different models of stack are used, however, the basic operation remains the same. The first model used is a PI-860.40. This stack is used for all sub-resonant tests with an electric heater. The PI-860.40 allows switch/sink movement up to 80 μm. The second model is a PI-601.40. This model allows an increased translation up to 150 μm. The PI-601.40 is used in all resonant testing with an electric heater. Fluid feeds to the heat sink determine the sink temperature and are controlled by a Neslab RTE-111 chiller. For all tests where the switch is used to cool the micro-engine, the fluid feeds are maintained at 4 °C. The temperature of the thermal switch is monitored via a Fluke 2176a Digital Thermometer using a T-type thermocouple mounted 1 mm below the thermal switch. Given fluid feeds maintained at 4 °C, the thermocouple typically records operating temperatures between 8 and 13 °C depending on the amount of switch-engine heat transfer.

Proper alignment between switch and evaporator membrane is critical to this test. One of the keys to heat rejection to the switch is maximizing the area of contact between evaporator membrane and switch. Because of this, the switch, heat sink, and actuator are mounted above a series of positioning stages that allow translation in vertical and horizontal directions. An additional tilt stage allows rotational alignment. The photograph in Figure 5.8 shows the thermal switch components and alignment stages used to position the switch.

Alignment is conducted visually using the thermal switch and a dummy membrane mounted above in an engine carrier. The switch is slowly raised into contact with the dummy membrane. Once in contact, the contact between the two is visually examined. Ideally, the switch engages a large area of the membrane. However, it is often necessary to use the tilt axis to realign the switch to maximize the area of contact. Once the contact area has been maximized, the dummy membrane is removed and the engine is placed above the switch, ready for operation.

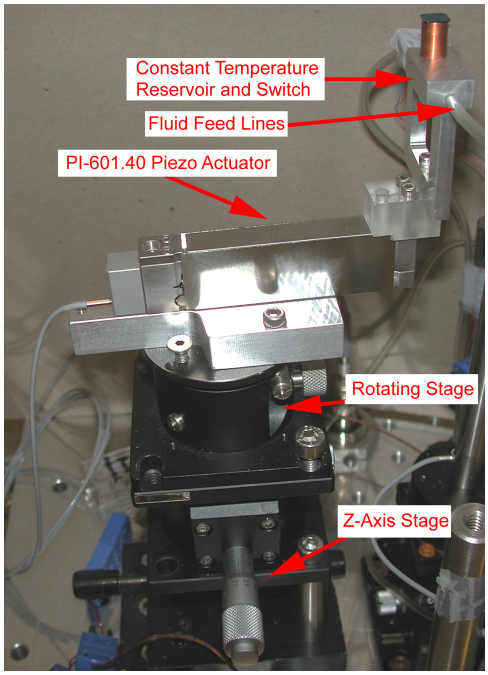

Figure 5.8: Thermal Switch and Alignment Stages

With the micro-engine and switch positioned correctly, electrical connections are made to heat the engine and operate the thermal switch. Figure 5.9 shows the combined micro-engine and switch system with the required electrical connections in place.

The timing between engine heat signal and switch cooling signal is critical. Because of this, Labview is employed to accurately time the two signals for each cycle. One signal is a square wave that controls heater operation. The second signal is a modified sine curve that controls the thermal switch actuation. Based on these signals, the micro-engine heater is activated via a TTL circuit that provides a square wave to the evaporator membrane resistance heater. Power to the resistance heater is controlled by varying the voltage of the attached power supply. The TTL circuit requires a voltage of 4.5V from Labview to initiate an electrical pulse to the evaporator membrane. Details of this TTL circuit design are further discussed by Whalen [64]. Figure 5.9 also shows the connection from the Labview interface board to the piezo amplifier. The amplifier is a combined PI-501 and PI-505 model that provides a 10x amplification of the incoming modified sine wave before sending it to the actuator.

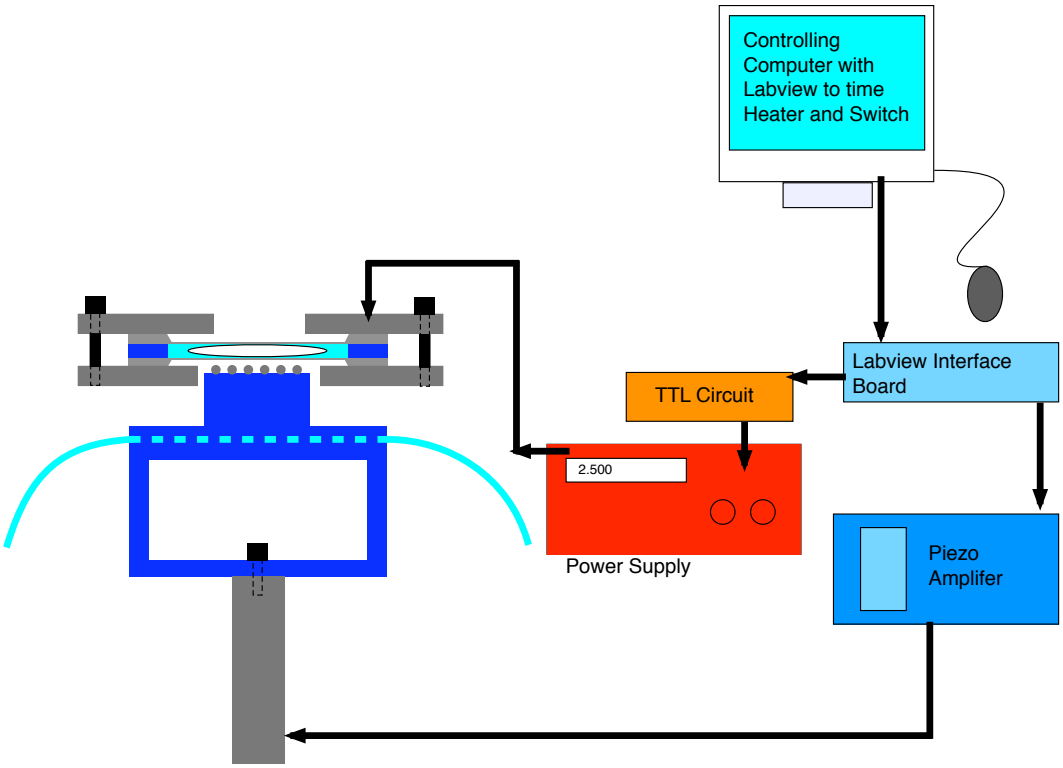

Figure 5.9: Electrically Heated, Switch Cooled Test Setup

The actuator itself operates linearly with respect to the incoming voltage from the amplifer. Typical signals generated by Labview to control heating and cooling are shown in Figure 5.10. This temporal timing represents the typical TTL signal versus switch actuation signal.

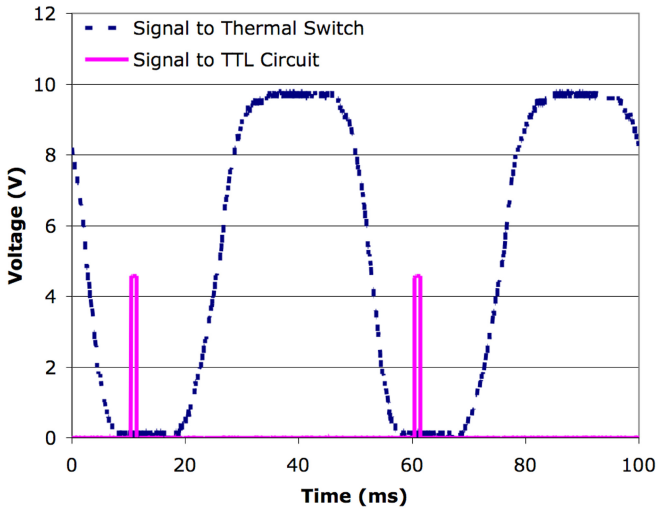

Figure 5.10: Engine Heater and Thermal Switch Timing

This timing is selected to allow the micro-engine to fully expand from heat addition before any heat rejection occurs via the thermal switch. The switch signal, therefore, is at its maximum between TTL pulses.

With the micro-engine and switch connected, operation of the system commences when heat is dissipated through the resistance heater on the evaporator membrane. This causes the micro-engine working fluid to evaporate. An increase in cavity pressure and expansion of the top membrane follows. Figure 5.11 shows the hardware used to measure the performance of the micro-engine.

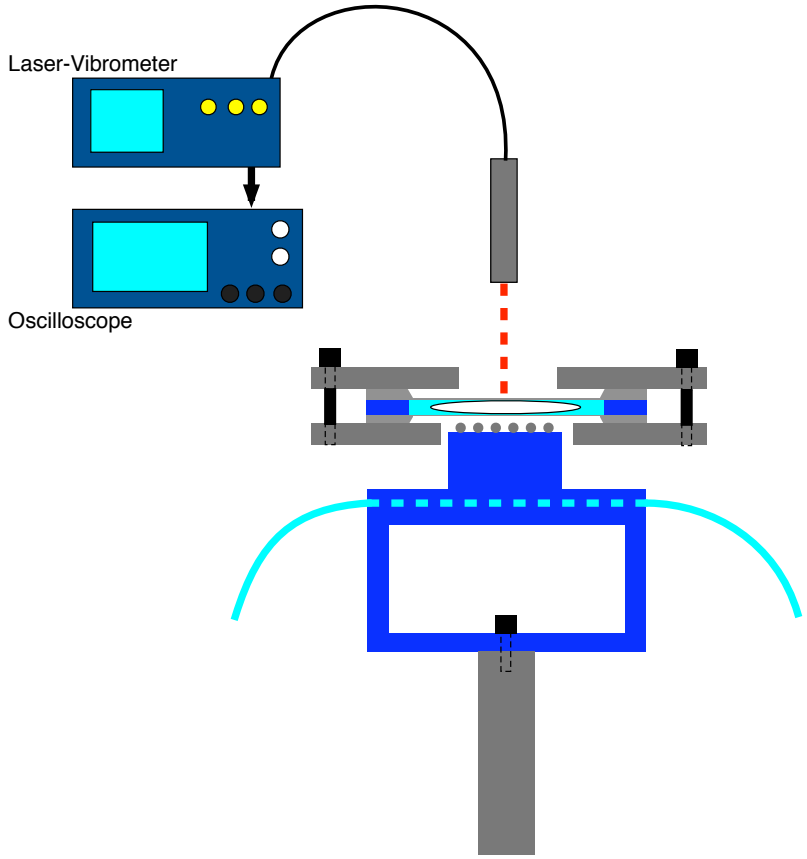

Figure 5.11: Setup for Measuring and Recording Engine Data

Membrane deflection is measured by a Polytec OFV-5000 laser vibrometer and then recorded by a Tektronix 5034b or 234a oscilloscope. The accuracy of deflection measurements is ± 17 nm. In the case of standard silicon top membranes, the vibrometer can accurately determine the membrane deflection from the silicon surface. The use of 300 nm thick SiNx membranes, however, presents a challenge. The thickness of the silicon-nitride is such that the laser vibrometer does not reflect from the surface, but instead penetrates the top membrane and reflects from the evaporator membrane. This is the key to determining the action of the lower membrane during resonant tests: focus of the laser vibrometer through the top membrane onto the evaporator membrane. However, even in resonant testing, the top membrane deflection must be recorded. To achieve this, a small gold pattern is used to reflect the vibrometer signal as described in Section 3.4.1. Moving the vibrometer to the side of the pattern allows it to focus again on the lower membrane. In this way, both top and bottom membrane deflections can be recorded.

The use of RTDs on the top or evaporator membrane allows the recording of membrane temperature during operation. Section 5.3.1 details the setup and use of the RTDs.

5.2.2 Switch Heated Engine Operation

The setup for micro-engine operation from a heated switch is similar to the setup described in Section 5.2.1. In this case, however, the switch is maintained at an elevated temperature and its contact with the evaporator membrane heats the engine. During these tests, the resistance heater is not used and the micro-engine is allowed to cool passively to the surrounding environment. An additional variation is the replacement of the PI piezo-stack actuator with a piezo-cantilever unit. Figure 5.12 shows the schematic for this engine and switch setup.

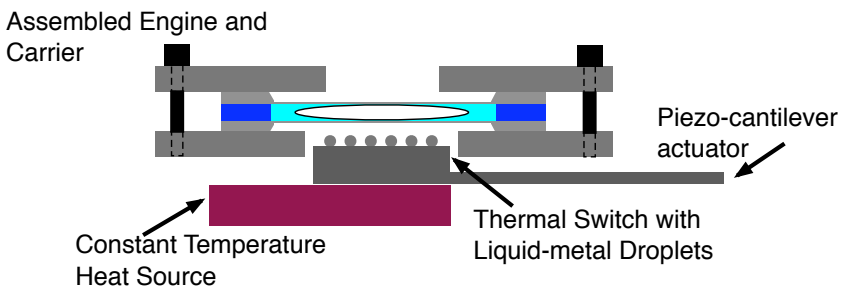

Figure 5.12: Heated Thermal Switch Test Setup

As with the cooled switch setup, the heated switch setup relies on the presence of a constant temperature heat source. The heat source conducts heat to the thermal switch surface and heats the switch to a temperature of 60 °C for these tests. The cantilever-based switch actuator shown in Figure 5.12 was manufactured at Washington State University in a process described by Cho *et al.* [59].

Control of the thermal switch is accomplished using the same PI 501-505 amplifer combination noted in Section 5.2.1 for PI piezo-stack control. The amplifier is fed a sinusoidal signal using a Sony AFG310 function generator. The action of the switch into contact with the engine initiates expansion of the cavity and stretching of the top membrane. As with the electrically heated setup, the performance of the micro-engine is monitored by the same laser-vibrometer and oscilloscope setup shown in Figure 5.11.

The use of this switch heated test is expressly for sub-resonant operations. Because only a single switch is used, there is no way to actively reject heat to a cold sink. This limits micro-engine operation to speeds below resonant frequency. This setup does, however, successfully produce sub-resonant operation of the micro-engine from a constant temperature heat source as outlined in the original design goals (Chapter 1).

5.2.3 Switch Heated and Switch Cooled Engine Operation

Because of the limited micro-engine operating speed when using a single thermal switch, an additional test is used to allow heating from one switch and cooling from a second. Operated out of phase, these switches independently conduct heat to or from the evaporator membrane and operate the micro-engine as a result. A schematic of the setup is shown in Figure 5.13.

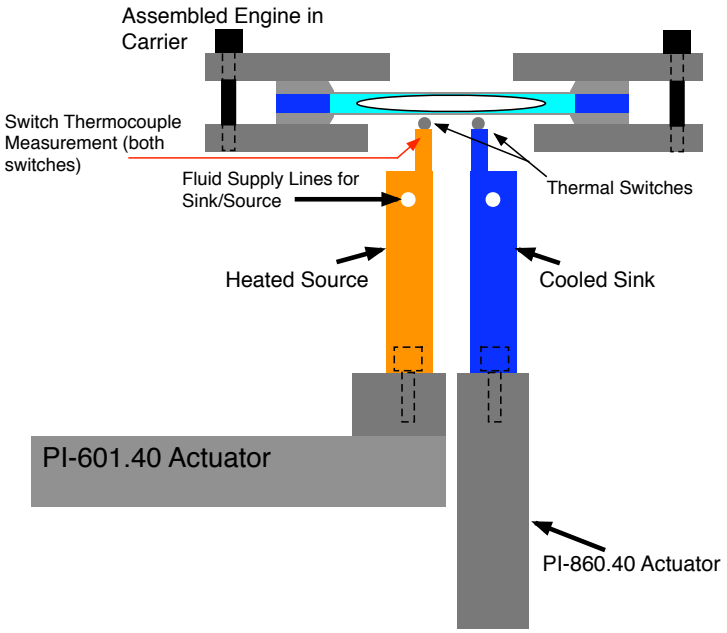

Figure 5.13: Dual Thermal Switch and Engine Setup

Much of the setup is the same as that described in Section 5.2.1, however, a second switch is added to replace the electrical heater. Figure 5.13 shows heated or cooled fluid is passed through the constant temperature heat source and sink. A thermocouple measurement is taken 1 mm below the switches as with the single switch setup. The use of both switches requires the use of both PI piezo-actutors (the PI-601.40 and PI-860.40) and two PI 500-501 amplifier setups. The PI-601.40 is used to translate the heated switch into contact with the evaporator membrane. The PI-860.40 is used to control the motion of the cooled switch into the evaporator membrane. The Labview program is employed to correctly time the actions of the two switches such that they operate 180° out of phase. In this setup,

the cooled switch is maintained at 14 °C using the Neslab RTE-111. The heated switch temperature is maintained by pumping hot water through the heat exchanger. A simple hot plate and aquarium pump provide the necessary flow. The temperature of the heated switch is maintained at 50 °C during dual switch testing. A photograph of the two constant temperature heat sinks and actuators is shown in Figure 5.14. As with the setup described

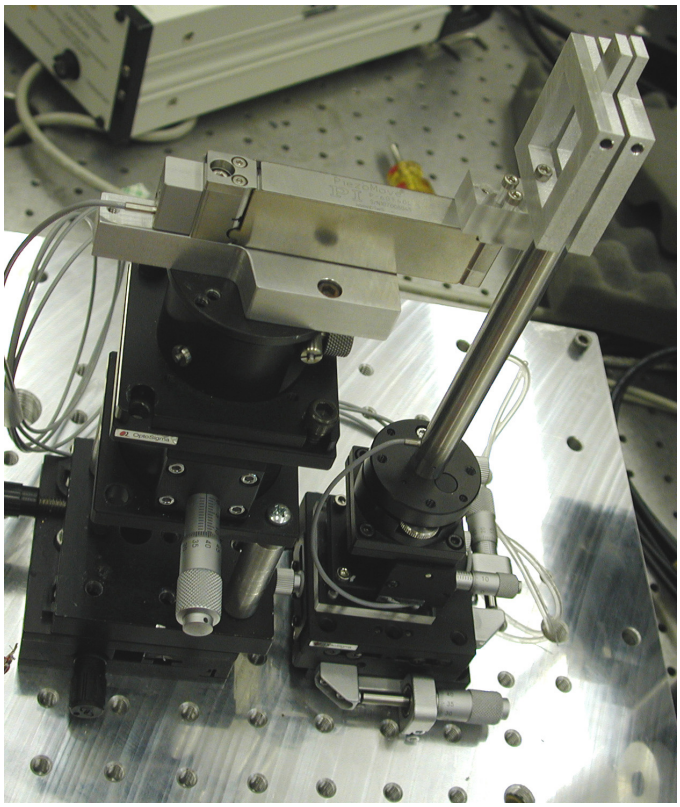

Figure 5.14: Dual Thermal Switch and Actuator Setup

in Section 5.2.1, care is taken to align the switches with a dummy membrane using multi-axis stages. This ensures the best engine-switch contact possible and best heat transfer characteristics as a result. As with other engine setups, the performance of the engine is monitored using the laser-vibrometer to measure membrane deflections and RTDs on the engine membranes to record temperature (Section 5.3.1).

5.3 Additional Tests and Measurements

There are several tests that are conducted to support operation of the micro-engine. This section describes these additional tests.

5.3.1 RTD Calibration and Use

RTDs, or Resistive Temperature Devices, are fabricated on the membranes to measure micro-engine operating temperatures as described in Chapter 3. The operation of these devices is based on a wheatstone bridge setup as described by Carpenter [71]. It is possible to monitor the changing resistance of the RTD as a function of temperature. However, use of an oscilloscope to monitor output as a function of time requires the RTD signal be in volts. Through use of the amplified bridge circuit, the changing resistance of the RTD results in a related voltage change that can be recorded. The key to this setup is the proper determination of the RTD temperature vs. voltage calibration curve.

To determine the RTD calibration, a water bath is used as shown in Figure 5.15. The membrane with patterned RTD is placed in an engine carrier then immersed in the DI water bath. A suspended thermometer is used to measure bath temperature. A Fluke 189 True RMS multimeter is used to measure the output from the amplified bridge circuit which is zeroed after the RTD is immersed. The hot plate provides heat to increase the temperature of the bath while the resulting temperature versus voltage output is recorded. This calibration setup provides an accurate temperature vs. voltage output calibration curve for each RTD used in engine testing.

To measure micro-engine temperature, the engine is first assembled with a calibrated RTD membrane. The membrane is then electrically connected to the same bridge amplification

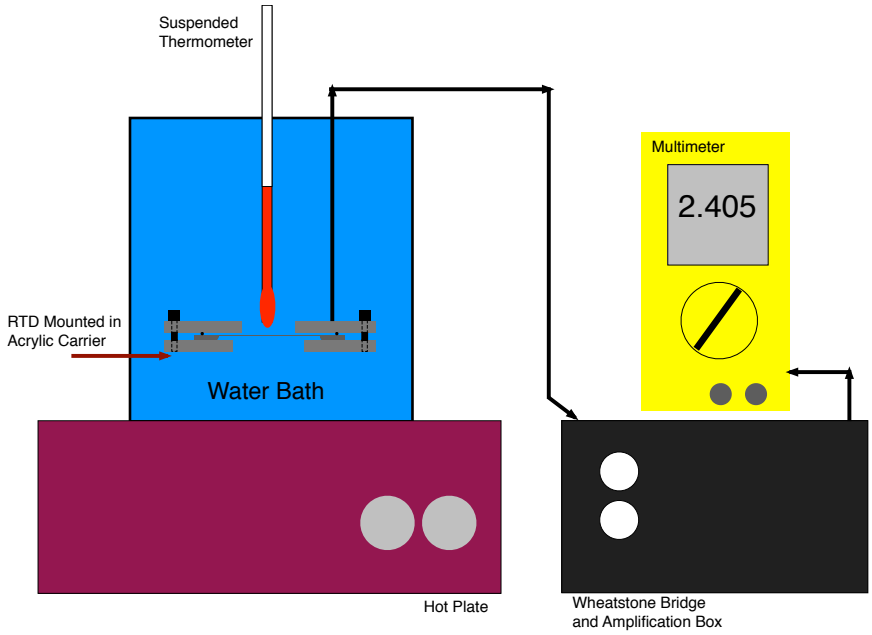

Figure 5.15: RTD Calibration Bath Setup

circuit as used during calibration. The voltage output from the circuit is recorded by a Tektronix 5034b or 234a oscilloscope. Using the known calibration curve, the recorded voltage is converted to temperature and the membrane operating temperature is known.

Two different types of RTDs are used in this work. The first are RTDs fabricated on the lower evaporator membrane. These lower RTDs have a measurement uncertainty of ±1.5 °C. The second RTD type is fabricated on the micro-engine top membrane. These RTDs have a measurement uncertainty of ±1.4 °C.

5.3.2 Simplified Switch Integration Setup

To measure the thermal characteristics of the interaction of the thermal switch with the micro-engine, a simplified test is conducted. Instead of the full setup noted in Section 5.2.1, this modified arrangement includes only an evaporator membrane mounted above a thermal switch. Figure 5.16 illustrates this simplified construction. In these tests, the PI 840.60

piezo actuator is used to control the switch position as determined by the displacement signal originated in Labview. The typical signal, causing an 80 μm displacement, is noted in Figure 5.10. As with the full micro-engine and switch integration setups, care is taken to properly align the switch beneath the evaporator membrane as described in Section 5.2.1.

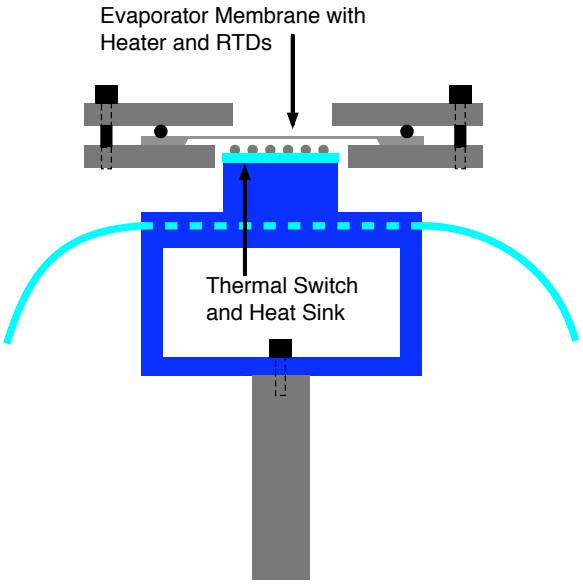

Figure 5.16: Experimental Setup for Switch Performance Testing

The evaporator membrane used in these experiments is a 5 mm, 2 μm thick Si design with a central resistance heater and two surrounding RTDs (Section 3.4.2). The switch can be operated at an elevated or depressed temperature relative to the membrane depending on the situation. The electric heater on the membrane allows the membrane temperature to be elevated by a constant DC current. Monitoring the RTD temperatures, as described in Section 5.3.1, while actuating the switch into the evaporator membrane, provides data on heat transfer from the membrane to the switch.

In these tests, care is taken to avoid high impacts between the switch and evaporator membrane. This is done to mimic the standard micro-engine and switch setup. High impact of the switch into the evaporator membrane of an engine causes mechanically forced deflection of the micro-engine top membrane. In this test, the laser-vibrometer is used to determine

the amount of evaporator membrane deflection due to switch impact. The deflection is maintained below 1 μm during these tests. Section 5.6 details the construction of a numerical finite-difference code that models this test.

5.3.3 Membrane Pressure-deflection Measurement

The determination of micro-engine operating pressure is critical to evaluating the micro-engine performance. The laser-vibrometer is used to measure the deflection of one of the membranes of the engine. The measured deflection is then converted into a pressure using a calibrated pressure-deflection curve. Pressure-deflection curves are determined via static pressure-deflection testing.

The process of static pressure-deflection testing is described in detail by Robinson [75]. To obtain the pressure-deflection curve, the membrane and surrounding die are bonded to an aluminum disk with a small central hole. The hole is attached to a variable pressure line. The pressure on the backside of the membrane is varied while a pressure sensor records the pressure. The laser-vibrometer is used to measure the resultant membrane deflection. Labview is used to monitor both the pressure sensor and vibrometer outputs to obtain a true pressure-deflection curve. Once obtained, the pressure-deflection curve for the membrane can be applied to any membrane deflection signal from the vibrometer. Pressure can then be determined from the membrane deflection. The uncertainty of this pressure is $\pm.05$ kPa.

5.4 Performance Calculations

The previous sections describe the different tests used to support the testing of the combined micro-engine and switch systems. This section examines the basic analysis that is used to determine micro-engine performance across the variety of operating conditions that are discussed.

5.4.1 Sub-resonant Work and Power Calculations

The work output from a micro-engine operating at sub-resonance is determined using indicated work, based on the top membrane deflection. As described in Section 5.3.3, the membrane deflection can be used to determine cavity pressure. For work calculation, however, the engine operating volume during the expansion process is also needed. Top membrane deflection is used to calculate the volume beneath it via the integration of Equation 2.5.

The expansion of the top membrane as a result of heat input can then be plotted on a pressure versus volume chart as shown in Figure 5.17. The area beneath this PV curve is

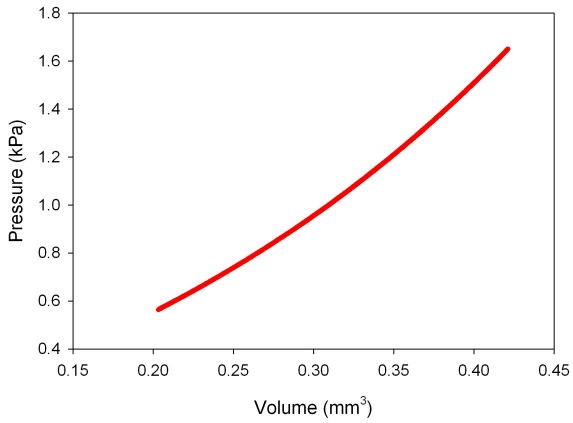

Figure 5.17: Typical Sub-resonance P-V Plot

the work output from the engine due to one expansion cycle. There are several methods to

calculate the area beneath this curve. The first is graphically with a program like Sigma Plot. Alternatively, it is possible to use the known pressure-deflection curve to analytically calculate the result. Both methods yield the same output. Figure 5.18 shows the area of interest on the measured pressure-volume plot.

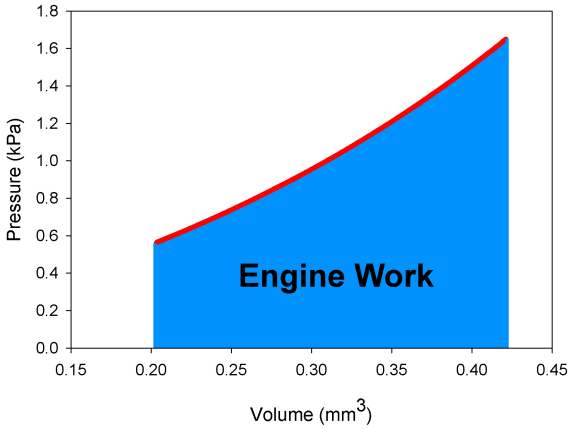

Figure 5.18: Work Output Area for Sub-resonant Engine Operation

To analytically determine the area beneath the plot, Equation 5.2 is evaluated across the engine operating volumes.

$$W = \int P dV \tag{5.2}$$

W: Work
P: Pressure
dV: Differential volume

This can be accomplished by first recognizing the form of the pressure-deflection curve: a cubic with odd ordered terms as shown in Equation 5.3.

$$P = C_1\delta + C_2\delta^3 \tag{5.3}$$

C_1, C_2: Curve-fit constants
δ: Membrane center point deflection
P: Pressure

Equation 5.3 represents the pressure in Equation 5.2. To describe the volume, Equation 2.5 must be integrated along the membrane edges as shown in Equation 5.4.

$$V(\delta) = \frac{\delta}{a^4} \int_{-a}^{a} \int_{-a}^{a} \left(a^2 - x^2\right) \left(a^2 - y^2\right) \left[1 + \frac{R}{a^2} \left(x^2 + y^2\right)\right] dxdy \tag{5.4}$$

V: Volume beneath membrane as function of δ
δ: Membrane center-point deflection
a: $\frac{1}{2}$ membrane side-length
x, y: Cartesian coordinates of membrane surface
R: Membrane constant, R=.31

Figure 5.19 shows the basic geometry for this integration. The center-point deflection, or δ, is measured in the positive "z" direction. The two membrane side lengths are measured in "x" and "y" directions. Integration of Equation 5.4 yields Equation 5.5.

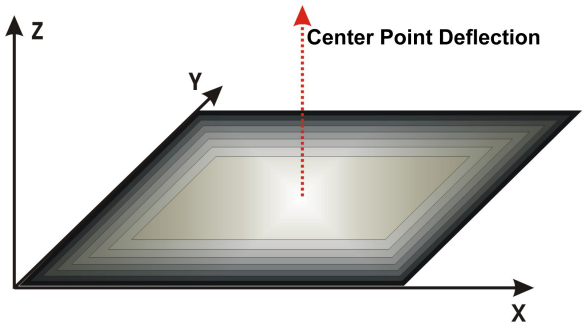

Figure 5.19: Membrane Geometry for Integration

$$V = \delta \frac{16}{45} a^2 \left(2R + 5\right) \tag{5.5}$$

Equations 5.3 and Equation 5.5 are incorporated into Equation 5.2 as shown in Equation 5.6. This effectively allows the integration over membrane center point deflection instead of volume.

$$W_{1,2} = \beta \int_1^2 \left(C_1\delta + C_2\delta^3\right) d\delta \tag{5.6}$$

W: Work done by expanding membrane
β: Combined constant based on membrane side-lengths and conversion factors
δ: Membrane center point deflection
Evaluated at minimum and maximum membrane deflections: 1, 2

Integration of Equation 5.6 yields Equation 5.7. The error associated with work output determination is $\pm 1.0 \times 10^{-7}$ J for micro-engines with 5 mm side-length top membranes. Work output error is $\pm 1.4 \times 10^{-7}$ J for micro-engines with 10 mm side-length top membranes.

$$W_{1,2} = \beta \left(C_1 \frac{\delta^2}{2} + C_2 \frac{\delta^4}{4} \right) \Big|_2^1 \tag{5.7}$$

Engine power output is determined by multiplying the amount of work per cycle by the number of cycles per second.

5.4.2 Resonant Work and Power Calculations

While sub-resonant micro-engine output power may be determined via Equation 5.7, resonant micro-engine output power cannot be determined in this way. This is because micro-engine operations at resonance no longer follow an expansion curve that can be expressed in the form of Equation 5.3. A typical resonant pressure-volume curve is shown in Figure 5.20. While sub-resonant operations do not produce cycle work, resonant operations do produce cycle work. The work is calculated by determination of the area shown in Figure 5.20. This area can be calculated by the use of a graphical analysis program like Sigma Plot. This area can also be calculated in a spreadsheet program by converting the overall area to many small rectangles. The individual rectangle height is the pressure, the width is the change in volume. Summation of the areas yields the cyclic work, or integrated area. It should be

noted that this method requires data capture with good resolution as in these tests. The error associated with cyclic work output is $\pm 2.5 \times 10^{-8}$ J. Power is calculated by multiplying the output work by the operating frequency in cycles/second.

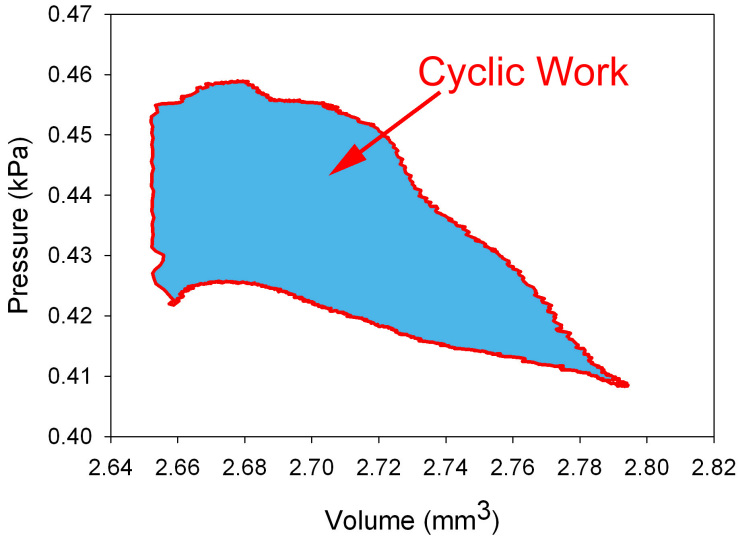

Figure 5.20: Work Output Area for Resonant Engine Operation

In these tests, the laser-vibrometer is used to measure the deflection of both the top and bottom membranes. As was the case for sub-resonant operations, the top membrane is used to determine the micro-engine operating volume via Equation 5.5. Unlike sub-resonant operations, however, the lower membrane is used to determine the operating pressure. A pressure-deflection curve is found for the evaporator membrane and this calibrated curve is used to calculate micro-engine pressure from the measured deflection. As the evaporator membranes are thick and stiff compared to top membranes, their resonant frequency is far higher than the micro-engine natural frequency. Because of this, the lower membranes respond to pressure changes in the engine cavity in a quasi-static fashion and provide an accurate view of engine operating pressure. The suitability of lower membrane pressure measurement is further discussed in Appendix E.

5.4.3 Electric Power Input Calculations

The electrical power input to the evaporator membrane is critical in determining the performance of the engine. Figure 5.21 shows the electrical circuit used to power the evaporator membrane heater as described in Section 5.2.1. Once activated, the TTL circuit allows current to flow in the membrane circuit for the duration of the incoming signal from Labview. To measure the power delivered to the resistance heater, an in-line load resistor is employed. The oscilloscope is used to measure a voltage drop across this load resistor. The current flowing to the electrical resistance heater is determined using Ohm's law. This current value is then used to determine the power delivered to the membrane using $P = IV$. The uncertainty associated with energy input is $\pm.15$ mJ. Uncertainty of the instantaneous power input is $\pm.03$ W.

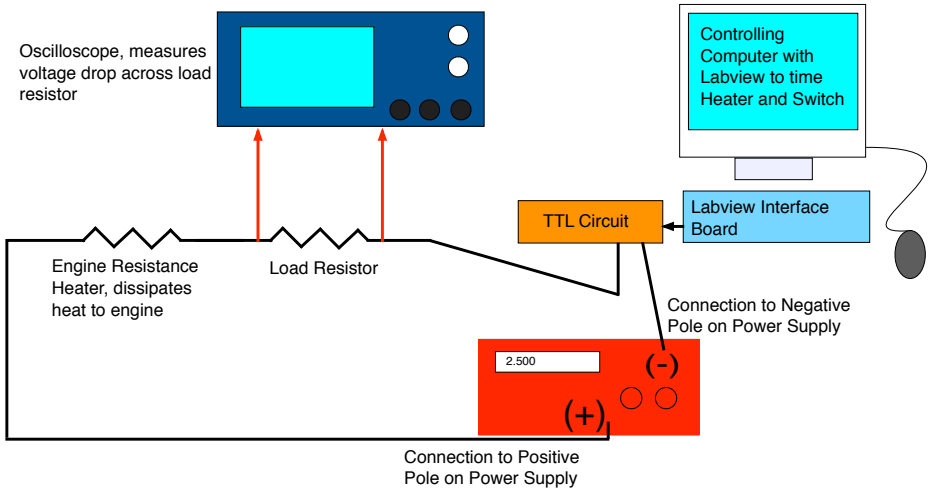

Figure 5.21: Circuit to Measure Electrical Power to Heater

5.4.4 Engine Efficiency Calculations

In this work, the micro-engine efficiency is defined as the engine work output divided by the input heat from the electric resistance heater located on the evaporator membrane. Equation 5.8 shows this relationship.

$$\eta = \frac{W}{Q_{elec}} \tag{5.8}$$

η=Engine operating efficiency
W: Work done by expanding membrane
Q_{elec}: Electrical heat input per cycle

The micro-engine work output is determined by methods discussed in Sections 5.4.1 and 5.4.2. The heat input energy is determined as described in Section 5.4.3. The error associated with efficiency calculation is $\pm 8.56 \times 10^{-4}$ % and $\pm 4.30 \times 10^{-4}$ % for micro-engines with 5 mm and 10 mm side-length top membranes respectively.

5.4.5 Peak Engine Applied Force Calculation

To determine the peak force a micro-engine is capable of producing, mass of a known value is added to the top membrane as described in Section 4.1.1. The engine is operated and monitored as described in Section 5.2.1. The deflection of the top membrane/mass is recorded via laser-vibrometer. Once heat has been added to the micro-engine via resistance heater, the top membrane and mass begin to translate. The initial change in their displacement represents the location of peak force. This is because the initial change in displacement equates to the maximum acceleration experienced by the top membrane/mass.

The recorded deflection value is input to a graphical analysis program and a curve-fit is used to establish a mathematical description for the initial motion. The first derivative of this curve yields the initial velocity. The second derivative of the deflection curve yields acceleration. The peak acceleration is used in Equation 5.9 with the mass to calculate the peak applied force. This measurement of force has an error of $\pm$ .018 N.

$$F = ma \tag{5.9}$$

F: Applied force
m: Mass placed on micro-engine
a: Acceleration determined via second derivative of deflection

5.5 Uncertainty Determination

This section reviews uncertainties associated with the measurements and calculations described in this chapter. Appendix B details the calculations that underlie these values.

5.5.1 Measurement Uncertainties

Table 5.1 compiles the various measurement uncertainties.

Measurement Errors		
Measurement	**Error**	**% of Typical Value**
Energy Input	± .15 mJ	± .1
Average Power Input	± .006 W	± .6
Instantaneous Power Input	±.03 W	± .35
Deflection	± 17 nm	± .02
RTD Temperature - Evaporator Membrane	± 1.5 °C	± 5.0
RTD Temperature - Top Membrane	± 1.4 °C	± 4.7

Table 5.1: Typical Engine Measurement Uncertainties

5.5.2 Calculation Uncertainties

The error associated with calculated quantities, in large part, is based on the uncertainty of the measured values that contribute. Table 5.2 summarizes the calculated errors for common operating conditions. Where appropriate, the differences between micro-engines assembled with 5 mm and 10 mm side-length top membranes are noted.

Calculation Errors		
Calculation	**Error**	**% of Typical Value**
Pressure	$\pm$ .05 kPa	$\pm$ .1
Volume - 5mm	$\pm$ 2.14×10^{-3} mm^3	$\pm$ .45
Volume - 10mm	$\pm$ 8.59×10^{-3} mm^3	$\pm$ .90
Work - 5mm	$\pm$ .10 μJ	$\pm$ 1.7
Work - 10mm	$\pm$ .14 μJ	$\pm$ 1.4
Cyclic Work	$\pm$ .025 μJ	$\pm$ 1.0
Efficiency - 5mm	$\pm$ 8.56×10^{-4} %	$\pm$ 8.0
Efficiency - 10mm	$\pm$ 4.3×10^{-4} %	$\pm$ 4.0
Force	$\pm$ .018 N	$\pm$ 42

Table 5.2: Typical Engine Calculation Uncertainties

5.5.3 Engine Performance Variability

It is important to recognize that while the error and uncertainty values discussed in this section accurately reflect the performance related to any single engine, performance varies from engine to engine outside of these values. Engine to engine variance is a function of many factors including the specific assemblies themselves. Chapter 4 notes the construction of these micro-engines is performed entirely by hand. This allows parameters such as working fluid amount and cavity sealing force (due to the engine carrier) to vary. These variables lead to performance variability across different engine constructions. In this work, every effort is made to ensure the reported engine performance values are reflective of typical operation and assembly. For operations at sub-resonant conditions, multiple micro-engines are assembled and tested to extract peak performance values from repeatable performance trends. Additionally, resonant operations rely on the testing of multiple engines to draw fundamental conclusions about operations at and around the resonant point.

Table 5.3 shows the variability associated with typical micro-engine operations at sub-resonant conditions. These values are based on a conservative 68 % confidence interval as described in Appendix B.

Engine to Engine Performance Variability					
Engine	**Wicks**	**Deflection (μm)**	**Work (mJ)**	**Effic. (%)**	**Power (mW)**
5 mm Si	10 μm	6.95	.0013	.004	.05
	40 μm	13.0	.0030	.012	.17
5 mm SiNx	10 μm	18.7	.0044	.030	.28
	40 μm	14.0	.0049	.013	.29
10 mm Si	10 μm	16.8	.0041	.005	.13
	40 μm	31.2	.0080	.012	.45
10 mm SiNx	10 μm	16.8	.0034	.005	.16
	40 μm	22.4	.0028	.007	.11

Table 5.3: Micro-engine Performance Variability

Appendix C examines the average peak deflection, work output, efficiency, and power output for the different micro-engine types constructed. Additionally, the standard deviation of these performance parameters is calculated.

5.6 Numerical Methods

The simplified switch integration test discussed in Section 5.3.2 is modeled via an axi-symmetric finite-difference heat conduction code. The code is used to provide more extensive insight into the operation of the thermal switch. Model predictions include switch performance parameters like thermal resistance ratio (R_{off}/R_{on}), temperatures, and maximum switch heat transfer capabilities. The foundation for the finite difference heat conduction code lies in the balance of heat transfer into and out of various elements defined by model nodes. Heat conduction is predicted by the standard heat conduction equation as shown in Equation 5.10. Equations relating to the heat transfer into and out of the elements are written to define temperature distribution and heat flux.

$$\frac{\partial T}{\partial t} = \kappa \frac{\partial^2 T}{\partial x_i^2} \tag{5.10}$$

T: Temperature
x_i: Cartesian coordinate
κ: Thermal diffusivity, $\kappa \equiv \frac{k}{\rho Cp}$
k: Thermal conductivity
ρ: Density
Cp: Specific Heat

A simplified schematic is shown in Figure 5.22 which outlines the basic nodal arrangement. Note the axis of symmetry represents a radius of zero as well as the rotational axis for elemental area and volume calculations.

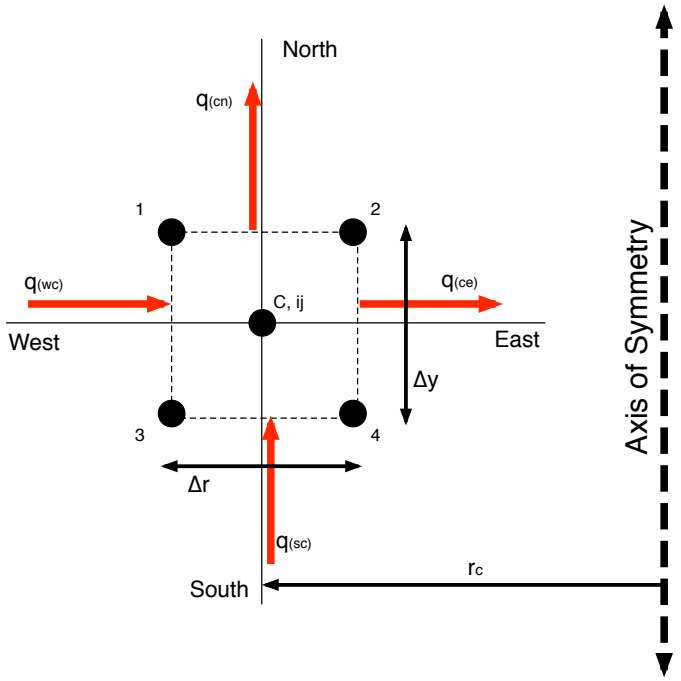

Figure 5.22: Simplified Model Setup

The total energy balance for the central node is given in Equation 5.11. q_s is the amount of heat stored as defined by the element surrounding the central node.

$$q_{wc} + q_{sc} - q_{ce} - q_{cn} = q_s \tag{5.11}$$

Newton's law of cooling is used to define the heat fluxes and is shown in Equation 5.12.

$$q_i = -k_i A \frac{\partial T}{\partial x_i} \tag{5.12}$$

q_i: Heat transfer in "i" direction

The change in energy stored in the central node element is given by Equation 5.13.

$$q_s = \rho C p V \frac{\partial T}{\partial t} \tag{5.13}$$

q_s: Energy stored in central element
V: Volume of central element

To allow solution via numerical methods, geometric approximations are applied as indicated in Equations 5.14 and 5.15.

$$\frac{\partial T}{\partial t} \sim \frac{T_{ij}^{l+1} - T_{ij}^{l}}{\triangle t} \tag{5.14}$$

i,j: nodal indicies
l: Time step index

$$\frac{\partial T}{\partial x_i} \sim \frac{\triangle T_{ij}^{l+1}}{\triangle x_i} \tag{5.15}$$

The "time step index" noted in these equations is a reference to the equation solver's current or previous solutions. The time step $l + 1$ is the next time step being considered by the solver. Time step l is the previous step. The indicies (i,j) relate the equation to the proper nodal location being considered by the code. Equation 5.16 shows the entire energy balance equation set for the central node in Figure 5.22.

$$
\begin{aligned}
q_{wc} &= -kA_r \frac{T_w^{l+1} - T_c^{l+1}}{\triangle r} \\
q_{sc} &= -kA_s \frac{T_s^{l+1} - T_c^{l+1}}{\triangle y} \\
q_{ce} &= -kA_r \frac{T_c^{l+1} - T_e^{l+1}}{\triangle r} \\
q_{cn} &= -kA_s \frac{T_c^{l+1} - T_n^{l+1}}{\triangle y} \\
q_s &= \rho C p V \frac{T_c^{l+1} - T_n^{l}}{\triangle t}
\end{aligned} \tag{5.16}
$$

Equation 5.17 shows the element areas and volumes used in Equation 5.16.

$$
\begin{aligned}
A_r &= 2\pi \triangle y \left(\frac{\triangle r}{2} + r_c \right) \\
A_s &= \pi \left[\left(r_c + \frac{\triangle r}{2} \right)^2 - r_c^2 \right] \\
V &= \triangle y A_s
\end{aligned} \tag{5.17}
$$

By combining the equations into the overall balance (Equation 5.11), the energy balance for the central node may be solved based on the temperatures of the nodes around it. This requires a recursive solution technique as an equation similar to Equation 5.11 must be written for each node in the model. By combining and rearranging the terms listed in Equation 5.16, a simplified matrix form (which includes equations for every node in the model) may be adopted as shown in Equation 5.18.

$$
[\mathbf{A}] \cdot [\mathbf{x}] = [\mathbf{c}] \tag{5.18}
$$

[**A**] : Matrix of constants with dimensions i,j
[**x**]: Array of unknown temperatures, T_i^{l+1}
[**c**]: Array of known values including constants and T_i^l values

With the solution form set, a standard Gauss-Elimination approach is used to solve for the unknown temperatures of the center nodes. Figure 5.23 illustrates the basic material and geometric setup established to model the thermal switch test in Section 5.3.2.

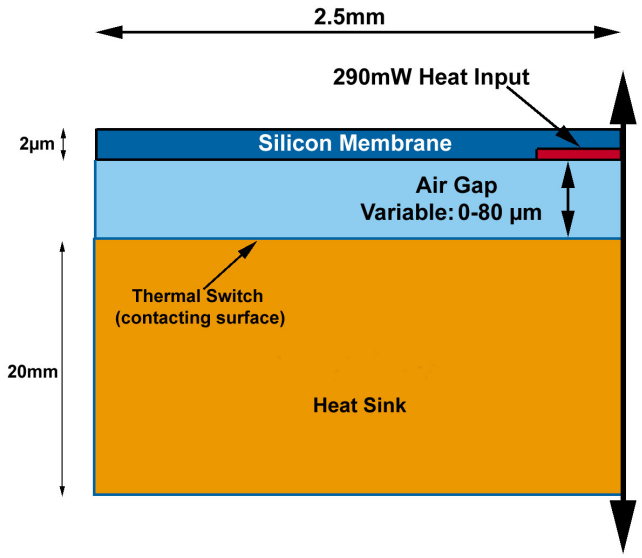

Figure 5.23: Axi-symmetric Model of Membrane and Thermal Switch

The model is split into an array of 18 by 20 nodes. Boundary conditions that define the model operation are established based on the experiment. A heat flux condition is maintained on the heat sink lower surface to accurately control temperature of the switch. Heat is input at the membrane center to simulate the heat addition in the experiment. The switch contact surface is modeled as a silicon contacting surface. A variable air gap between the silicon evaporator membrane and thermal switch allows the conduction between membrane and switch to vary with time. To allow the model to accurately reflect the surface contact of the real device, the air gap is maintained at 2.5 μm when the switch is in its highest or "contacting" position. This simulates the action of the thermal switch in the experiment. The model is shown to accurately predict membrane temperature in Figure 5.24. This validates model operation.

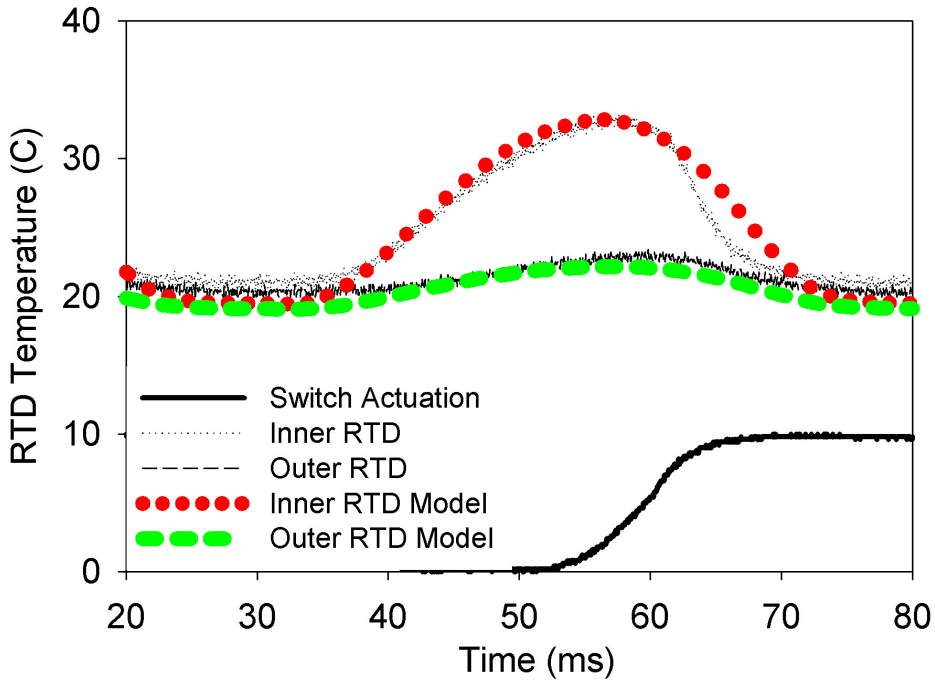

Figure 5.24: Comparison of Predicted and Measured Membrane Temperatures

Chapter 6

Engine and Switch Integration

This chapter discusses the results of integrating the micro-engine with a thermal switch. The motivation for thermal switch integration is twofold. First, it is desirable to provide a method of heat rejection to offset increasing micro-engine temperatures associated with high-speed operation. It was noted by Whalen that maximum operating speed of an electrically heated micro-engine using passive heat rejection was about 40 Hz [64]. By controlling the micro-engine temperature, performance and speed may be increased. Second, a method must be developed to introduce heat into the micro-engine from a constant temperature heat source. Integration of a thermal switch with the micro-engine addresses both of these needs.

The thermal switch operates by making and breaking contact with the micro-engine evaporator membrane as noted in Chapter 1. Several aspects of switch integration are examined in this chapter. First, the switch is operated in a simplified test setup where it provides heating or cooling to a membrane with dual RTDs. Two different switch contacts are examined. First, a surface with liquid-metal micro droplets is considered. Second, a bare silicon surface is considered. A finite difference heat conduction code is created to model specific heat transfers and characteristics of thermal switch operation. Finally, the thermal switch is

integrated with a micro-engine. The performance of the engine is examined when the switch is used as the primary means for heat rejection.

6.1 Thermal Switch Performance

To better understand the thermal performance of the thermal switch, measurements were made with a switch making and breaking contact with a membrane only. During these tests the switch was operated from both a cold reservoir (for heat rejection) as well as a heated reservoir (for heat addition). The switch performance was examined using two different contact surfaces. In the cooling set of experiments, the switch was operated without mercury droplets. When the switch was heated, both plain silicon and mercury droplet surface contact switches were considered. An axi-symmetric finite-difference heat conduction model was created to predict heat transfer and thermal switch performance based on these tests.

6.1.1 Cooled Thermal Switch Testing

The simplified experiment used in these switch integration tests is described in Section 5.3.2. An evaporator membrane was located above the thermal switch and heated by supplying a constant DC current to its resistance heater. The 5 mm evaporator membrane was constructed as described in Section 3.4.2. The switch, allowed to translate 80 μm beneath it, was maintained at a temperature of 14 °C. In this manner, the constantly heated membrane, was periodically cooled by contact with the thermal switch. Membrane temperatures were recorded by the two concentric RTDs.

The heater was supplied with a constant 290 mW. The switch contacted the evaporator membrane at a frequency of 20 Hz. Figure 6.1 shows the RTD temperatures recorded during the experiment. The experiment showed the effectiveness of the switch at removing heat from the evaporator membrane, cooling it by up to 14 °C near the membrane heater.

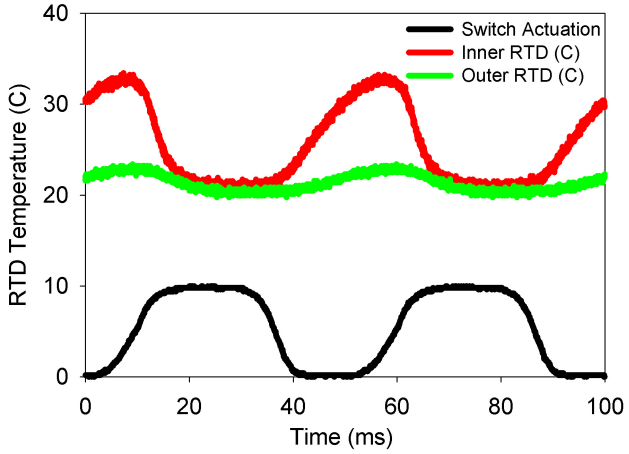

Figure 6.1: Evaporator Membrane RTD Temperature, 20 Hz Switch Actuation

6.1.2 Heated Switch and Contact Surface Testing

To address the question of how the contact surface impacted thermal switch performance, an experiment was performed using one switch with mercury micro-droplets as a contact and one switch with a bare silicon surface contact. The switch was maintained at a high temperature (60.5 °C) to simulate heating of a micro-engine and allowed to operate at 20 Hz. During these tests, no electrical heating was applied to the evaporator membrane. All heating was accomplished via thermal switch. Figure 6.2 shows the temperatures (from the inner RTD) as the switch contacted and heated the membrane.

The figure shows minimal difference between the two membrane temperatures for the switch with mercury droplet contact and the switch with no micro-droplets (dry contact). This was because care was taken to limit the switch contact with the evaporator membrane. This was

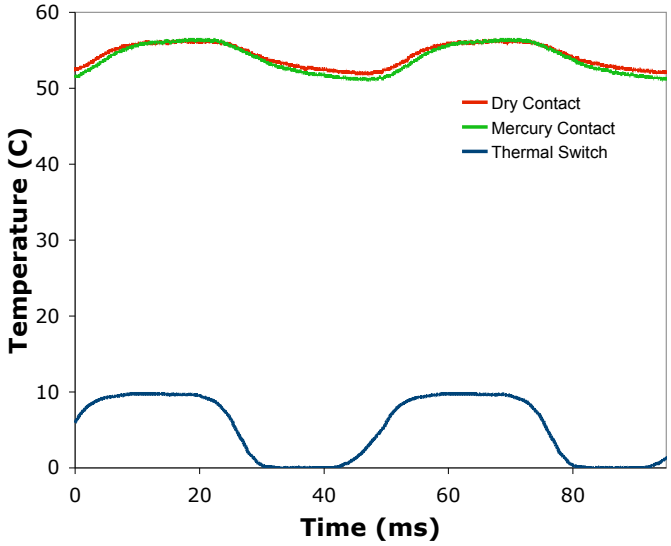

Figure 6.2: Membrane Heated by Thermal Switch with Dry and Hg Contact Surfaces

done to mimic the situation of a thermal switch in contact with a real micro-engine. Because the micro-engine could respond to a force from either internal evaporation or mechanical switch contact, care was taken to limit switch impact on the evaporator membrane. This effectively limited the quality of switch/micro-engine contact and thus the amount of heat transfered as well. This also limited the effectiveness of mercury droplets on the thermal switch.

6.1.3 Finite-Difference Thermal Switch Modeling

To better understand the complexities of thermal switch integration, a heat conduction code was created based on the cooling switch experiment in Section 6.1.1. Section 5.6 discusses the details of the code and its development. Boundary conditions for the system were set to maintain a heat sink temperature of 14 °C as in the experiment. 290 mW was supplied to

the nodes simulating the membrane heater.

Switch performance parameters were calculated from the model. The model indicated that the performance of the switch was limited due to its small translation beneath the membrane (only 80 μm) and poor contact with the evaporator membrane. Due to these limiting factors, the ratio of thermal resistances between the switch and membrane was predicted to be only a factor of $R_{off}/R_{on} = 3$. This result indicated the switch was somewhat effective in its role to cyclically reject heat from the heated engine. However, this result also indicated an area for improvement.

Another characteristic determined via the model was the maximum heat transfer the switch was capable of handling. The peak heat transfer was calculated to be 200 mW.

6.2 Engine and Cooled Switch Integration Results

With the basics of thermal switch operation understood, the switch was integrated with a full micro-engine as described in Section 5.2.1. In these tests, the operating mode for the micro-engine was sub-resonant. Heat addition was controlled via the electrical resistance heater fabricated on the surface of the evaporator membrane. After fully expanding, the micro-engine was actively cooled by allowing the thermal switch to translate 80 μm until it contacted the evaporator membrane. The thermal switch was maintained at a temperature of 14 °C. The piezo-stack actuator then pulled the switch away from the evaporator membrane and the micro-engine was again cycled via the electrical resistance heater.

The micro-engine was assembled using 5 mm side-length membranes. The evaporator membrane was fabricated with 10 μm high wicks and a standard gold resistance heater. The micro-engine cavity thickness was 75 μm. The top membrane used was a 2 μm thick silicon

membrane. The micro-engine was operated at a speed of 40 Hz and given 1.5 mJ of heat every cycle. In the initial test, the switch was allowed to gently contact the evaporator membrane and conduct heat from the engine. In the second test, the switch was not used to remove heat from the micro-engine. The switch used in these experiments was operated without mercury droplets on its contacting surface. Figure 6.3 shows the micro-engine top membrane deflection results for these operating conditions.

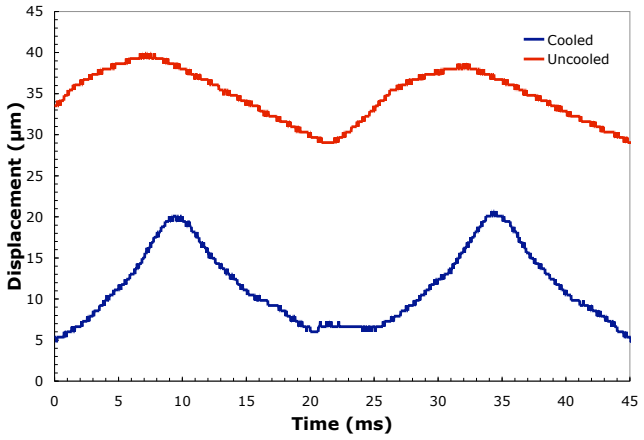

Figure 6.3: Top Membrane Deflection With and Without Thermal Switch

Figure 6.3 illustrates several important aspects of thermal switch integration. First, use of the thermal switch to control heat rejection reduced the minimum top membrane deflection by a factor of six. This was due to the higher average temperature of the uncooled micro-engine. During operation, this higher temperature resulted in increased cavity pressure and increased average membrane displacement. Additionally, the peak-to-peak top membrane deflection increased by 20 % with the use of the thermal switch. As the micro-engine was operating at a cooler temperature, there was more working fluid available for evaporation. This resulted in increased peak-to-peak top membrane deflections. Based on this test, the benefit of thermal switch integration was clear: reduced average cavity pressure (allowing effective operations beyond 40 Hz) and increased peak to peak top membrane deflections.

6.3 Thermal Switch Integration Summary

Overall, these switch integration tests showed mixed results. Clearly the switch did improve the micro-engine operation, allowing increased operating speeds and improved peak-to-peak performance via active heat rejection. The micro-engine showed the potential to operate beyond 40 Hz and peak to peak deflection was increased by 20 %.

Despite these improvements in micro-engine operation, the combination of limited contact and small switch translation resulted in the low thermal resistance ratios noted by the model. These results also indicated that the switch was most effective at lower frequencies, but lost effectiveness as operating speed increased. At increased operating speeds, the need for heat rejection could surpass 200 mW.

In terms of resonant operation, these results indicate an important tradeoff: the micro-engine must be run fast enough to resonate, however, slow enough to allow the thermal switch to provide effective heating or cooling. This tradeoff was taken into consideration when designing a micro-engine capable of resonance near 100 Hz.

These results also showed a reduction in switch capability as compared to steady state switch operations [57]. In steady state tests, the switch showed a thermal resistance ratio of $R_{off}/R_{on} = 15$ using mercury droplets to improve switch contact and with an atmospheric pressure air gap between switch and membrane. While it was disappointing that the switch did not perform better when integrated with the micro-engine (especially when using mercury droplets on the contacting surface), the reasons for this limited performance are known.

Chapter 7

Sub-resonant Engine Operation Results

This chapter discusses the results of micro-engine operation at sub-resonant conditions. Sub-resonant operation is detailed in Section 5.1.1. Two different heat addition methods were used in these tests. First, the micro-engine was heated electrically and cooled via thermal switch as described in Section 5.2.1. Electrically heated tests were used to map the operating characteristics of the micro-engine. Second, the micro-engine was operated from a constant temperature heat source as described in Section 5.2.2. These tests showed the viability of operation from a steady state heat source.

The evaluation of micro-engine operation using electric heat addition considered many different design iterations. Two micro-engine sizes were used. The first used membranes with 5 mm side-lengths (called 5 mm engines). The second used an evaporator membrane 8 mm on a side and top membrane 10 mm on a side (called 10 mm engines). There were several engine components evaluated during these tests. First, the top membrane was varied. A 2 μm thick silicon top membrane and a 300 nm thick silicon-nitride top membrane were used.

Second, the wick height on the evaporator membranes was varied. Both 10 μm and 40 μm tall wick heights were used. Assembly of the engines was performed as described in Chapter 4 using a cavity thickness of 75 μm in all cases. The thermal switch was maintained at 10 °C during these tests. The micro-engine and switch were operated at 20, 40, and 100 Hz. Many engines were assembled and tested to establish valid trends and repeatability. Because of this, peak top membrane deflections, engine work outputs, engine power outputs, and operating efficiency were evaluated during these tests as well as the average peak values and standard deviation across the tested micro-engines. The peak values attained from the most effective micro-engines are presented in this chapter. Appendix C presents the average peak results with standard deviations.

Operation of the micro-engine from a constant temperature heat source was evaluated using engines constructed of 5 mm side-length membranes. Top membrane deflection and power outputs were monitored with increasing frequency from 1 to 29 Hz.

7.1 Electrically Heated 5 mm Engine Operation

Many different micro-engines were constructed and tested using differing wick structures and top membranes. The engine work outputs, efficiency, and top membrane deflections were monitored for each construction and each operating frequency. This section details results of micro-engines constructed using 25 mm^2 evaporator and top membranes as they were operated with increasing heat input to the point of engine failure. In these tests, no liquid-metal droplets were used on the thermal switch contacting surface.

7.1.1 Silicon Top Membrane Results

Micro-engines were constructed using evaporator membranes having 10 μm high wick channels and 40 μm high wick channels. The top membrane used was a 2 μm thick silicon type. Several results are noted in the following figures. Figure 7.1 shows the maximum top membrane deflections versus input energy per cycle. The engines constructed using 40 μm high wicks showed increased deflections compared to those using 10 μm high wicks. This increased performance was likely due to increased fluid evaporation from the tall wick channels. Maximum deflection was 124 μm recorded at 100 Hz with 40 μm high wicking channels.

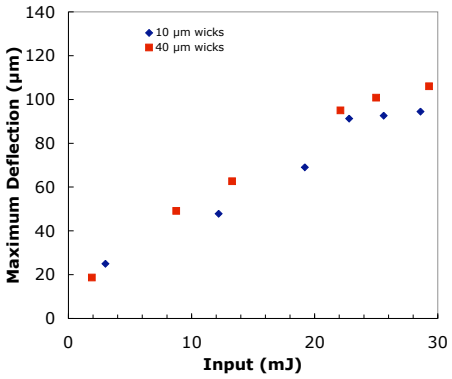

(a) 20Hz

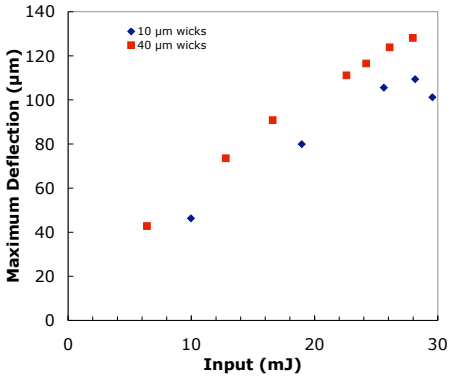

(b) 40Hz

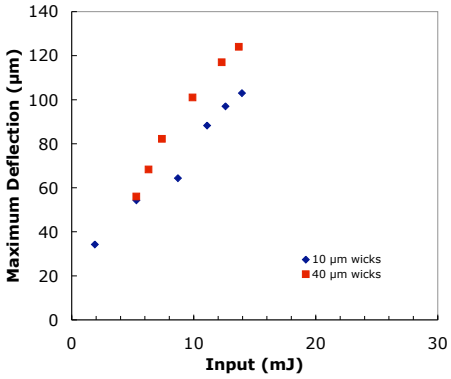

(c) 100Hz

Figure 7.1: 5 mm Si Top Membrane Maximum Deflections

Figure 7.2 shows the peak work output from the top membranes of these micro-engines. The advantage of the 40 μm wicks can be noted.

Table 7.1 summarizes the maximum operating efficiencies measured for these micro-engines. As with work output, efficiency was maximized when using 40 μm high wicks. Table 7.2 summarizes the maximum power output of these micro-engines.

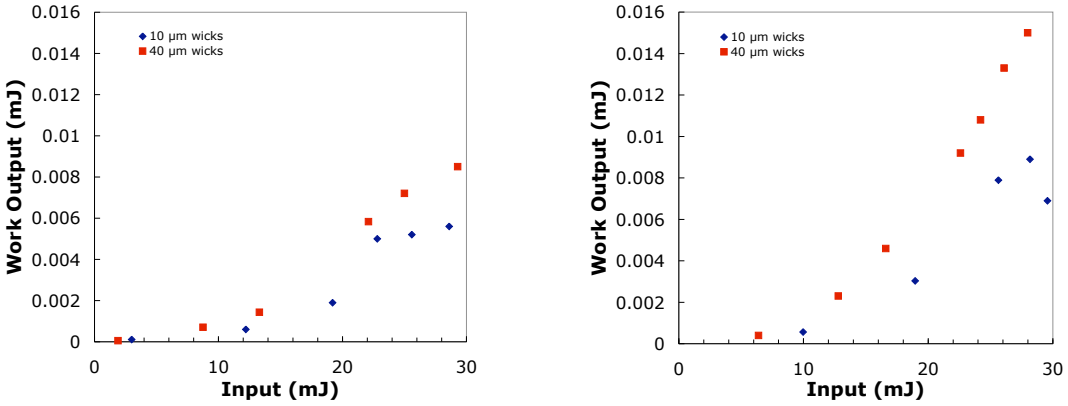

(a) 20Hz

(b) 40Hz

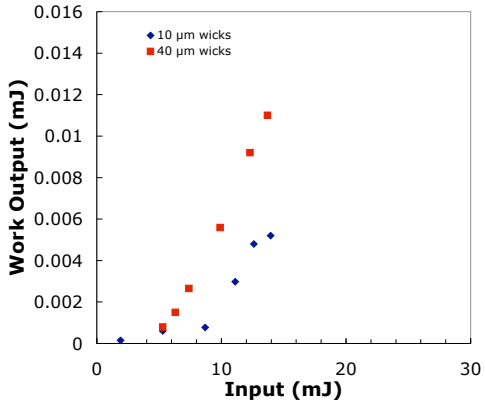

(c) 100Hz

Figure 7.2: 5 mm Si Work Output and Peak to Peak Deflection

Maximum Efficiency Outputs				
Engine	**Wicks**	**20 Hz**	**40 Hz**	**100 Hz**
5 mm Si	10 μm	.020 %	.032 %	.037 %
5 mm Si	40 μm	.029 %	.054 %	.078 %

Table 7.1: 5 mm Silicon Micro-Engine Efficiency

Peak to peak deflection at 20 Hz and 100 Hz for a micro-engine assembled using 40 μm high wicks is shown in Figure 7.3. This result showed the limitations of the thermal switch as operating speed increased and was typical of all sub-resonant operation. At 20 Hz, with

Maximum Power Outputs				
Engine	**Wicks**	**20 Hz**	**40 Hz**	**100 Hz**
5 mm Si	10 μm	.11 mW	.36 mW	.52 mW
5 mm Si	40 μm	.17 mW	.60 mW	1.1 mW

Table 7.2: 5 mm Silicon Micro-Engine Power Outputs

the switch operating effectively, the peak-to-peak deflections were highest. The maximum values recorded were 74.7 μm . However, as operating frequency increased, the time allotted to cool the micro-engine per cycle was reduced. This limited the performance of the thermal switch. 38 μm was the recorded maximum peak-to-peak deflection at 100 Hz. Hence, while maximum deflection was increased as a result of increased operating speed, the peak-to-peak deflection was actually reduced. Despite this, power output increased with operating frequency. This occurred because of the cubic relationship between pressure and membrane deflection noted in Equation 5.3 and the increasing cycles per second.

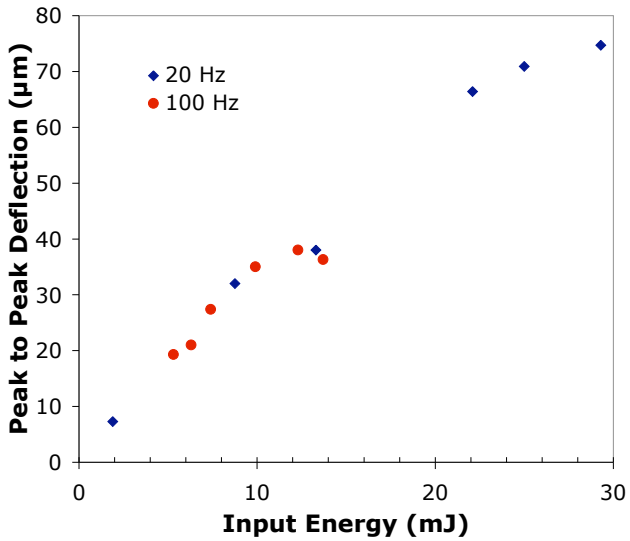

Figure 7.3: 5 mm Si Peak to Peak Deflection: 20, 100 Hz

7.1.2 Silicon-nitride Top Membrane Results

Micro-engines were assembled again using 10 and 40 μm high wick structures. Instead of a 2 μm thick silicon top membrane, however, a 300 nm thick SiNx top membrane was used. This was done to increase membrane flexibility (allow increased deflections for a given pressure) and reduce the thermal mass of the membrane. As expected, engines assembled with silicon-nitride top membranes performed significantly better than their silicon top membrane counterparts. Figure 7.4 shows maximum deflections from the top membrane with the micro-engines operating at 20, 40, and 100 Hz. The maximum deflection attained was 191.6 μm using 40 μm high wicking channels at 100 Hz. Unlike micro-engines constructed with silicon top membranes, the use of 40 μm high wicking structures did not result in significant deflection improvements. This result was also noted when the maximum micro-engine work outputs were determined. Figure 7.5 shows the work output per cycle. Maximum work output was .022 mJ at 100 Hz using 10 μm high wicks.

Table 7.3 summarizes the maximum operating efficiencies for these micro-engines. Table 7.4 summarizes the maximum power output of these micro-engines. Little difference in operation was found between 10 and 40 μm high wicked engines using a SiNx top membrane. This result was repeatable. This result was also noted in 10 mm micro-engine operations. It was unclear what caused this result.

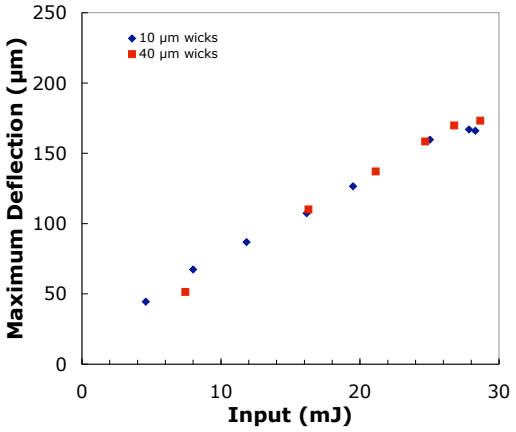

(a) 20Hz

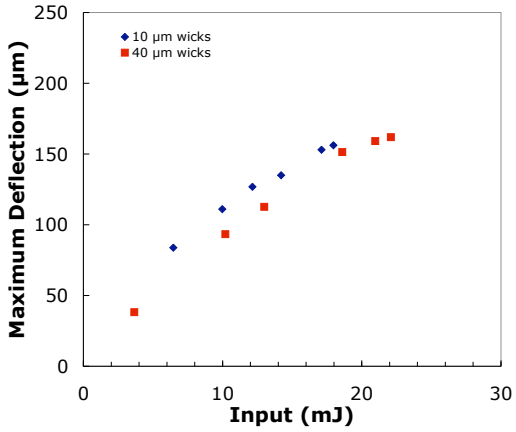

(b) 40Hz

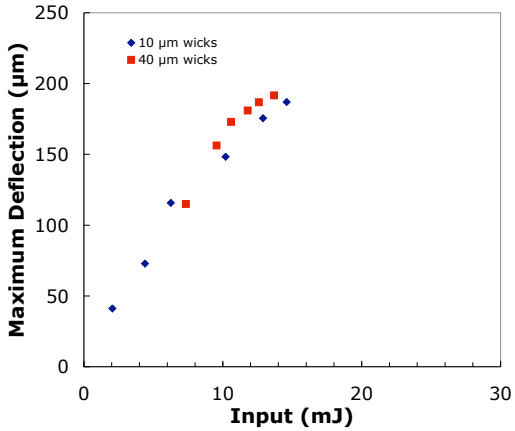

(c) 100Hz

Figure 7.4: 5 mm SiNx Top Membrane Maximum Deflections

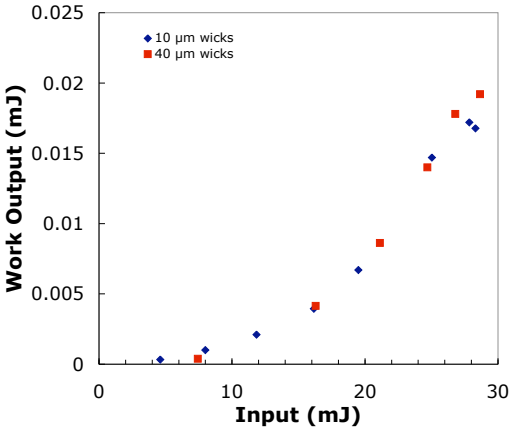

(a) 20Hz

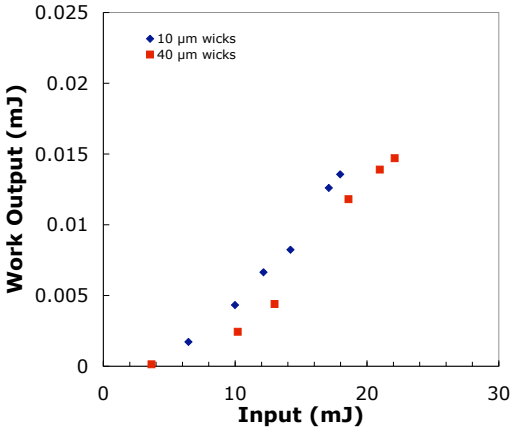

(b) 40Hz

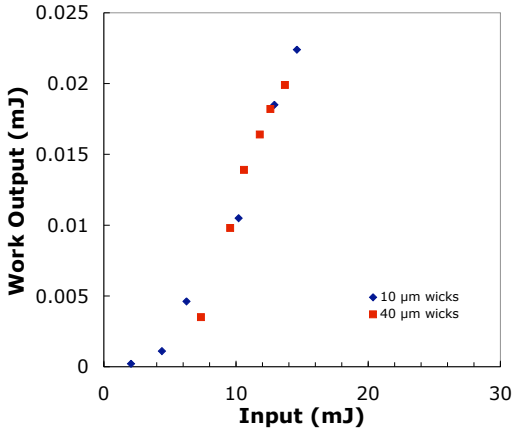

(c) 100Hz

Figure 7.5: 5 mm SiNx Work Outputs

Maximum Efficiency Outputs				
Engine	**Wicks**	**20 Hz**	**40 Hz**	**100 Hz**
5 mm SiNx	10 μm	.062 %	.075 %	.154 %
5 mm SiNx	40 μm	.067 %	.067 %	.145 %

Table 7.3: 5 mm Silicon-nitride Micro-Engine Efficiency

Maximum Power Outputs				
Engine	**Wicks**	**20 Hz**	**40 Hz**	**100 Hz**
5 mm SiNx	10 μm	.34 mW	.54 mW	2.2 mW
5 mm SiNx	40 μm	.38 mW	.59 mW	2.0 mW

Table 7.4: 5 mm Silicon-nitride Micro-Engine Power Outputs

7.2 Electrically Heated 10 mm Engine Operation

Micro-engines were constructed using larger membranes. The evaporator membranes used were 64 mm^2. The top membranes were 100 mm^2. As with smaller engines, two different wick geometries were used (10 μm and 40 μm high) and two different top membranes were used (2 μm thick Si and 300 nm thick SiNx). No liquid-metal droplets were used on the thermal switch contacting surface. All engines were operated at 20, 40, and 100 Hz.

7.2.1 Silicon Top Membrane Results

Micro-engines were constructed using top membranes fabricated of 2 μm thick silicon. Evaporator membranes had 10 μm high wick channels or 40 μm high wick channels. Figure 7.6 shows the maximum top membrane deflections versus input energy per cycle. For the most part, the engines constructed using 40 μm high wicks showed increased deflections compared to those using 10 μm high wicks. Maximum deflection was 268 μm recorded at 100 Hz with 40 μm high wicking channels.

Operation at 20 Hz showed the best results using 10 μm high wick structures. This was because evaporators constructed with 40 μm high wick channels proved less tolerant of

membrane flexing during heat loading. The use of a stiff 40 μm high wicking structure on a larger membrane (as compared to a 5 mm side-length evaporator membrane) tended to slightly buckle the membrane at its edge. This placed a stress concentration near the membrane boundary and increased the likelihood of failure due to flexing at high heat input. This caused evaporator membrane failure at lower heat inputs than membranes with 10 μm high wick structures. As operating frequency increased from 20 to 100 Hz, the amount of energy input per cycle diminished, thus eliminating this failure mode.

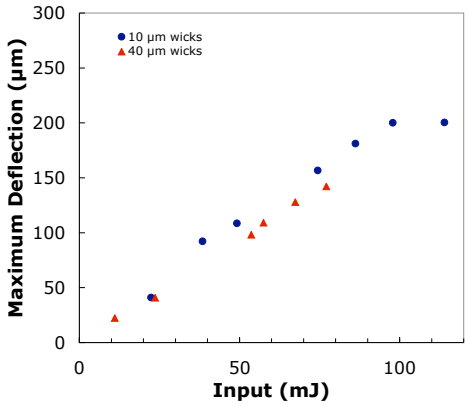

(a) 20Hz

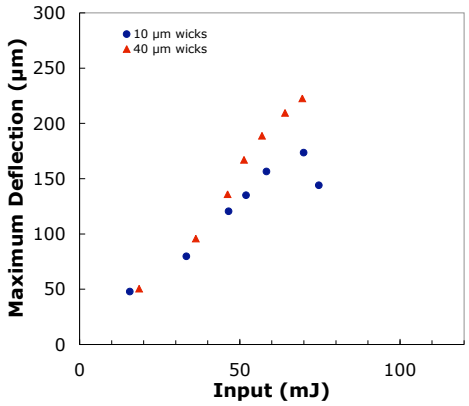

(b) 40Hz

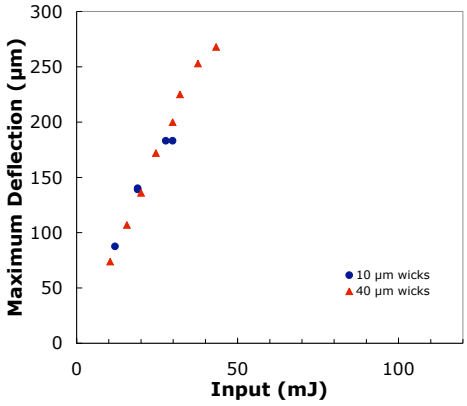

(c) 100Hz

Figure 7.6: 10 mm Si Top Membrane Maximum Deflections

Work outputs from the micro-engine are shown in Figure 7.7. Maximum work performed by the micro-engine was .037 mJ recorded at 40 Hz using 40 μm high wick channels. The maximum operating efficiencies are shown in Table 7.5. Table 7.6 summarizes the maximum power output of these micro-engines.

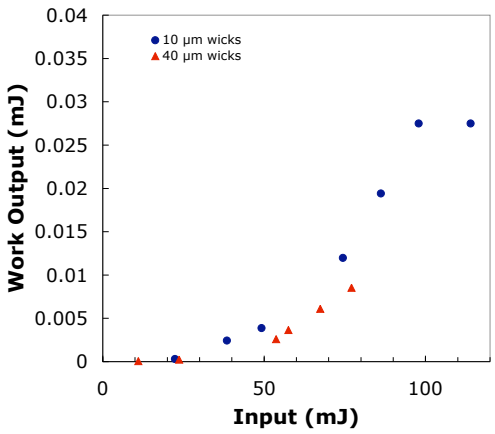

(a) 20Hz

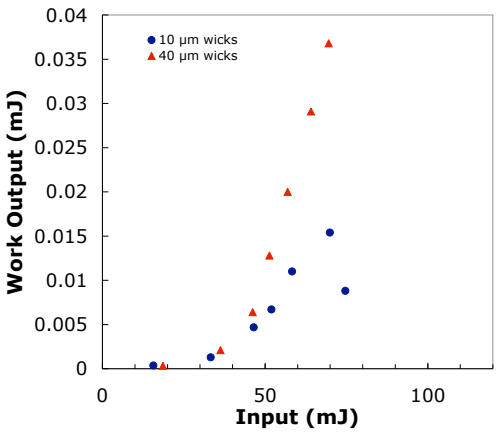

(b) 40Hz

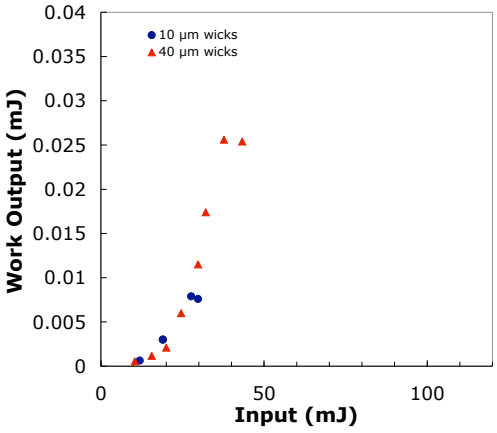

(c) 100Hz

Figure 7.7: 10 mm Si Work Outputs

Maximum Efficiency Outputs				
Engine	**Wicks**	**20 Hz**	**40 Hz**	**100 Hz**
10 mm Si	10 μm	.028 %	.022 %	.029 %
10 mm Si	40 μm	.011 %	.053 %	.068 %

Table 7.5: 10 mm Silicon Micro-Engine Efficiency

Maximum Power Outputs				
Engine	**Wicks**	**20 Hz**	**40 Hz**	**100 Hz**
10 mm Si	10 μm	.55 mW	.62 mW	.79 mW
10 mm Si	40 μm	.17 mW	1.5 mW	2.6 mW

Table 7.6: 10 mm Silicon Micro-Engine Power Outputs

7.2.2 Silicon-nitride Top Membrane Results

Micro-engines were assembled using 10 and 40 μm high wicking structures. Instead of a 2 μm thick silicon top membrane, however, a 300 nm thick top membrane was used. Figure 7.8 shows maximum deflections from the top membrane with the micro-engines operating at 20, 40, and 100 Hz. The maximum deflection attained was 275 μm using 10 μm high wicking channels at 40 Hz. As with 5 mm SiNx engines, the use of 40 μm high wick structures did not result in significant operating improvements.

Figure 7.9 shows the work outputs for these engines per cycle. A maximum work output of .031 mJ was attained at 40 Hz using 10 μm high wicks. Peak efficiencies for these micro-engines are shown in Table 7.7. Table 7.8 summarizes the maximum power output of these micro-engines.

The utilization of a silicon-nitride top membrane improved some aspects of 10 mm micro-engine operation compared to a standard silicon membrane. The efficiency of operation was increased, however, the maximum power output was reduced. This was due to engine failure before increased power output could be attained. The delicacy of the 10 mm silicon-nitride top membrane was responsible for this.

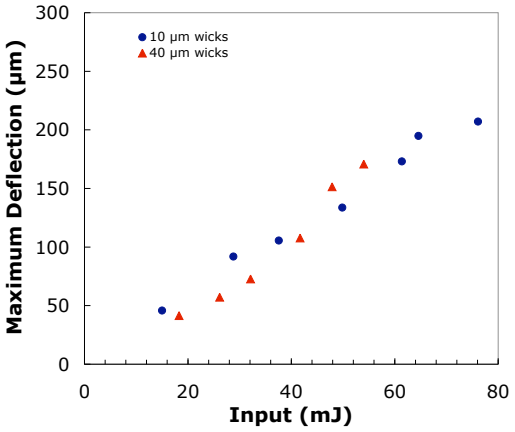

(a) 20Hz

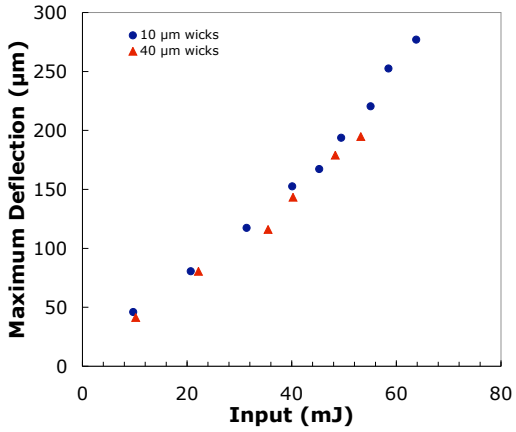

(b) 40Hz

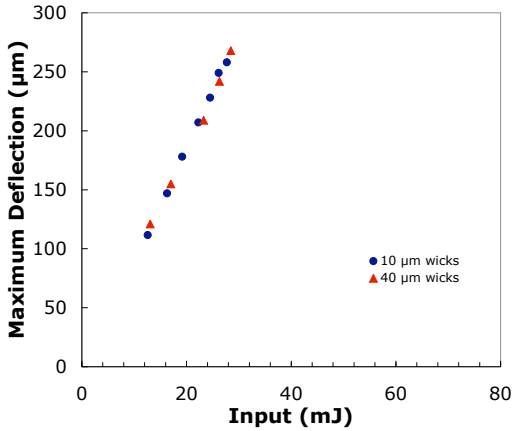

(c) 100Hz

Figure 7.8: 10 mm SiNx Top Membrane Maximum Deflections

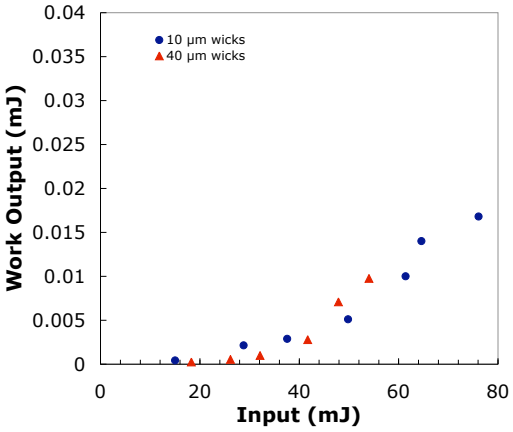

(a) 20Hz

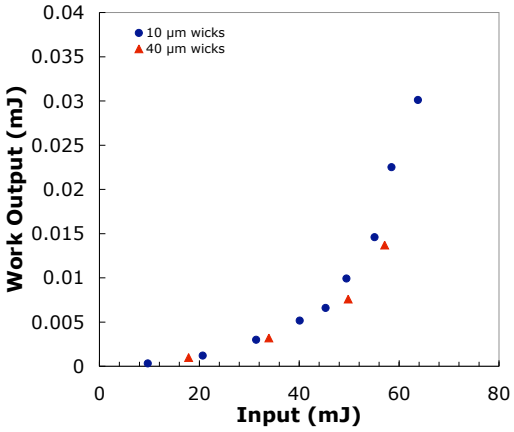

(b) 40Hz

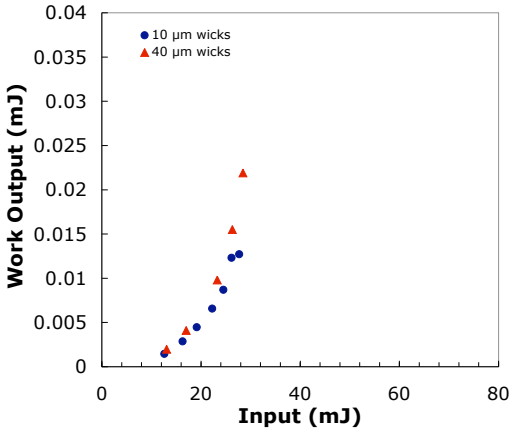

(c) 100Hz

Figure 7.9: 10 mm SiNx Work Outputs

Maximum Efficiency Outputs				
Engine	**Wicks**	**20 Hz**	**40 Hz**	**100 Hz**
10 mm SiNx	10 μm	.022 %	.047 %	.046 %
10 mm SiNx	40 μm	.018 %	.023 %	.078 %

Table 7.7: 10 mm Silicon-nitride Micro-Engine Efficiency

Maximum Power Outputs				
Engine	**Wicks**	**20 Hz**	**40 Hz**	**100 Hz**
10 mm SiNx	10 μm	.35 mW	1.2 mW	1.3 mW
10 mm SiNx	40 μm	.20 mW	.55 mW	2.2 mW

Table 7.8: 10 mm Silicon-nitride Micro-Engine Power Outputs

7.3 Engine Applied Force

Tests were run to evaluate the force a micro-engine could apply to a mass added to the engine top membrane. An engine was constructed with an added mass of 1.2 grams as described in Section 4.1.1. The micro-engine was constructed using an 8 mm side-length silicon evaporator membrane with 10 μm wicks, a 75 μm thick cavity, and a 10 mm side-length, 300 nm thick silicon-nitride top membrane. The addition of the mass allowed the determination of the engine applied force when moving the mass. The engine was operated at 20 Hz and heated electrically with 30 mJ of input energy. It was cooled via thermal switch (without liquid-metal surface contact droplets) as described in Section 5.2.1. Deflection of the top membrane (and therefore the added mass) was used to determine the applied force as described in Section 5.4.5

Figure 7.10 shows the top membrane/mass deflection when operated at 20 Hz. Also noted in the figure is the time of the mass deflection considered for applied force analysis.

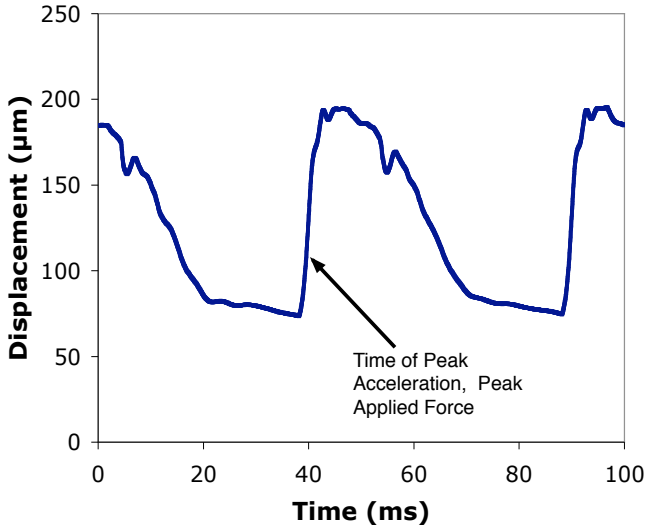

Figure 7.10: Deflection of Top Membrane with Added Mass

Figure 7.11 shows the calculated acceleration for the expansion event indicated in Figure 7.10. Figure 7.12 shows the force applied to the added mass as a result of the recorded deflection. The maximum force was 43 mN which compared favorably to the force outputs of various actuators detailed in literature [32, 37, 38].

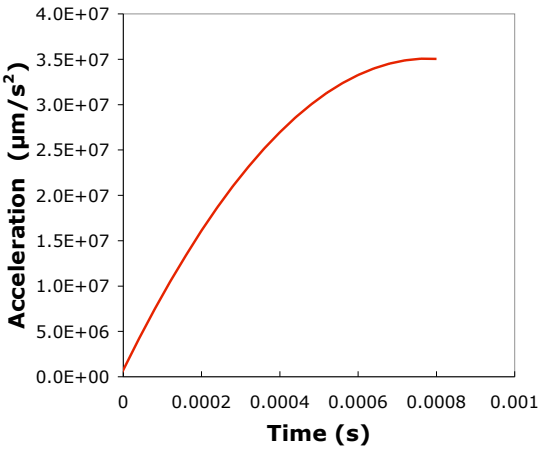

Figure 7.11: Acceleration of Added 1.2 g Mass

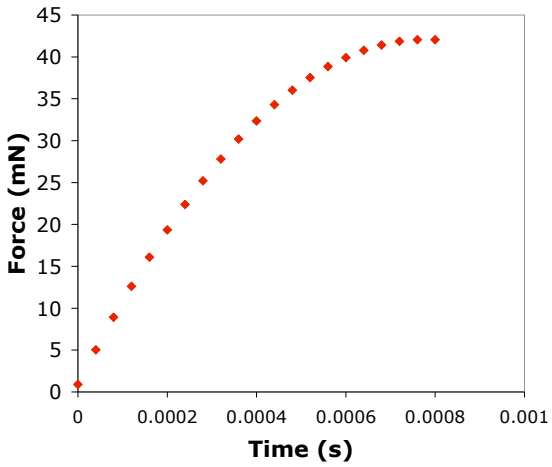

Figure 7.12: Applied Force to Added 1.2 g Mass

7.4 Thermal Switch Heated Engine Operation

A micro-engine was assembled using standard techniques described in Chapter 4. The lower membrane was a 25 mm^2 evaporator with 10 μm high wicks. The engine cavity thickness was 75 μm. The top membrane was a 25 mm^2, 300 nm thick SiNx design. The engine was placed over a heated thermal switch as described in Section 5.2.2. In these tests, liquid-metal droplets were used on the thermal switch contacting surface. The switch was heated to 60 °C and allowed to periodically contact the evaporator membrane at frequencies from 1 to 29 Hz. Engine cooling was to the ambient surroundings.

Figure 7.13 shows the top membrane peak to peak deflections as a function of increasing operating speed. The maximum peak to peak deflection of 234.2 μm occurred at a cycle speed of 1 Hz. As operating frequency increased, the peak to peak deflections declined as a result of lack of cooling. Like the peak to peak deflection, work output per cycle also declined with increasing operating frequency as shown in Figure 7.14.

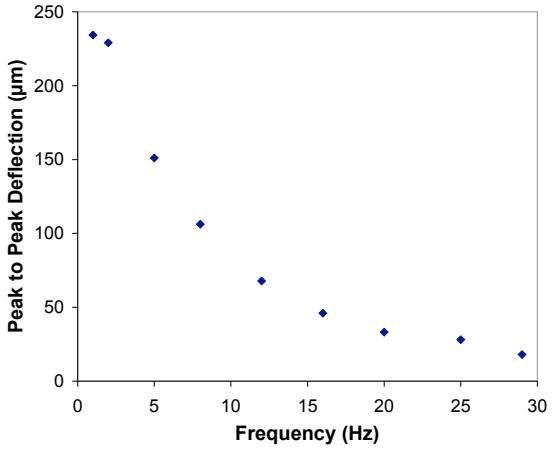

Figure 7.13: Thermal Switch Heated Peak to Peak Deflections

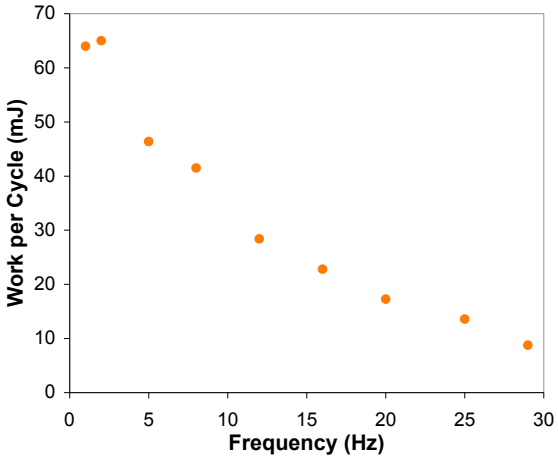

Figure 7.14: Thermal Switch Heated Work Output per Cycle

Power output for the micro-engine heated via thermal switch benefitted from increasing operating frequency, however. Figure 7.15 shows the indicated power output as a function of operating frequency. Maximum power output of .36 mW occurred at 16 Hz.

These tests showed the viability of micro-engine operation from a constant temperature heat source as described in the original concept. Additionally, the results of operating this micro-engine without the benefit of active cooling were interesting for several reasons. First, the benefit of active cooling via thermal switch was obvious as the power output for the device

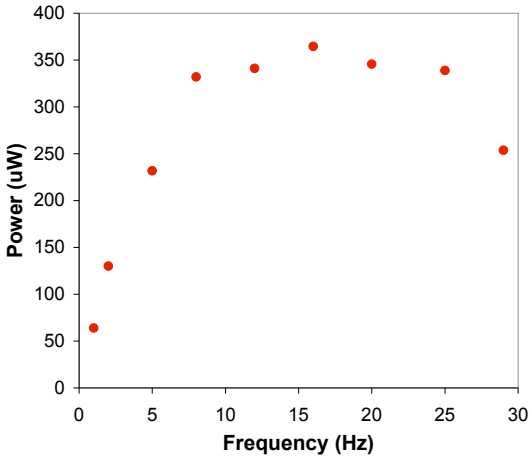

Figure 7.15: Thermal Switch Heated Power Output

fell dramatically after 25 Hz. This was consistent with previous work that estimated 40 Hz as the maximum operating speed for an engine operated without active heat rejection [64]. Second, despite the declining work output per cycle noted in Figure 7.14, the power output remained constant across a range of operating frequencies from 7 Hz to 25 Hz as work output fell. After 25 Hz, however, power output declined as well.

Chapter 8

Resonant Engine Operation Results

The integration of the thermal switch with the micro-engine allows active heat rejection to a low-temperature heat sink. This results in the ability to operate the micro-engine at increased frequency. By increasing the operating frequency to the natural frequency of the engine, resonant operation is achieved. This chapter describes the results of micro-engine operation in and around the resonant frequency.

Two different experimental setups were considered for resonant operation. The first used the basic experimental setup as described in Section 5.2.1. In these tests the evaporator membrane was heated electrically and cooled by thermal switch. The second set of experiments used two thermal switches to control micro-engine operation. One switch was maintained at an elevated temperature and provided heat addition. The second switch provided active heat rejection. The basic dual-switch setup is described in Section 5.2.3. The resonant operation of micro-engines is detailed in Section 5.1.2. The basic pressure-volume curve for a resonating micro-engine is reproduced in Figure 8.1. The four basic processes of heat addition, expansion, heat rejection, and compression are noted in the figure.

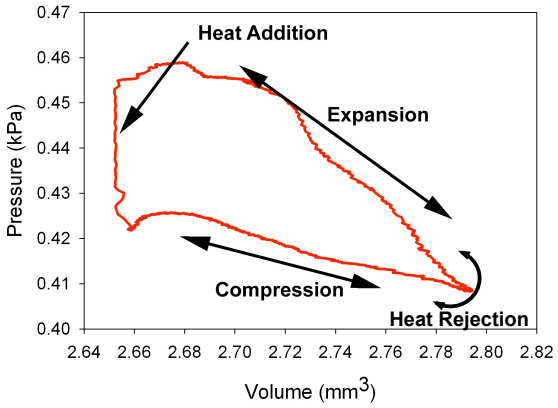

Figure 8.1: Basic Micro-engine Resonant Cycle

Constant volume heat addition is an interesting feature of this cycle. This is due to the fast heating of the evaporator membrane resistance heater. A similar constant volume heat rejection could be achieved if the thermal switch were altered to produce a more singular "on" and "off" heat transfer condition. In these tests, however, the switch closes on the evaporator membrane, contacts it, and moves away. The heat rejection rate varies continuously as a result.

8.1 Electrically Heated Resonant Operation

As described in Section 5.2.1, micro-engines with added mass were placed above a constant temperature thermal switch maintained at 10 °C. The thermal switch was used without liquid-metal droplets during these tests. Heat addition was controlled electrically through the evaporator membrane resistance heater. The micro-engines were allowed to operate at a variety of frequencies to fully document operation in and around their natural frequency.

8.1.1 Operation Through a Frequency Spectrum

A micro-engine was constructed with a 10 mm side-length, 300 nm thick SiNx top membrane, 150 μm cavity, and 9 mm cross-type evaporator membrane. An additional mass of 2.5 g was added to the top membrane. The micro-engine was cooled by contact with the thermal switch. The combined engine and switch system were operated at varying frequencies of 40, 60, 80, 90, 100, and 120 Hz. This allowed examination of micro-engine characteristics at varying speeds from below resonance to beyond resonance. Three operating regimes were noted during operation: sub-resonance, resonance, and super-resonance.

An engine cycle frequency of 40 Hz was the first operating point considered during these tests. Figure 8.2 shows the deflection measurement from top and lower membranes as well as temperatures recorded by RTDs on the membranes. The heat input to the micro-engine was 1.6 mJ per cycle. The engine ring-out is clear as a result of operation at this sub-resonant frequency.

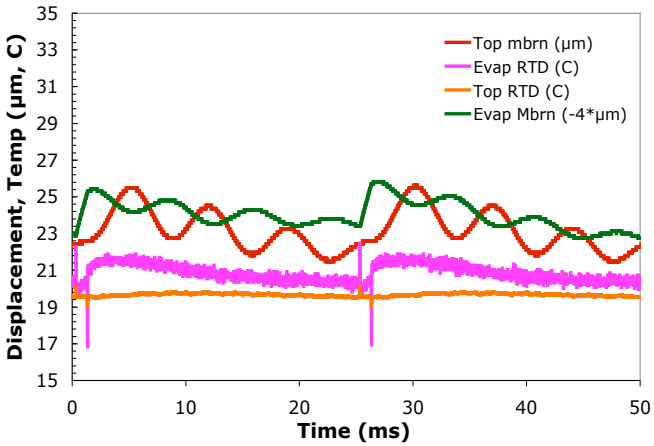

Figure 8.2: 40 Hz Operation of Micro-Engine with Added Mass

For comparison, an engine without added mass was operated with the same components and at the same conditions. Figure 8.3 shows the measurements taken from the engine without

added mass. The two engines presented several different operating characteristics. First, the

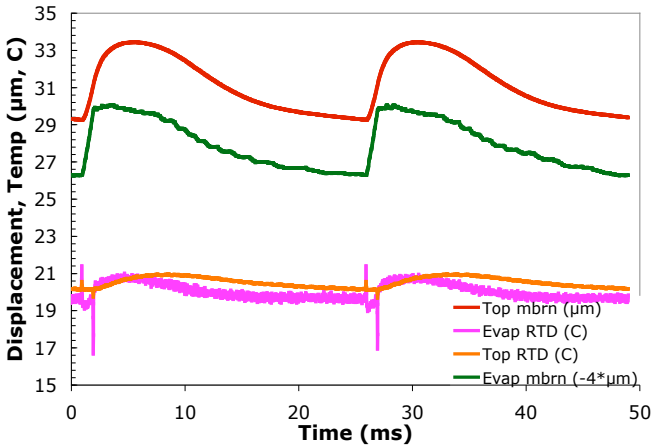

Figure 8.3: 40 Hz Operation of Micro-Engine without Added Mass

overall temperature of the engine without added mass was higher. This was especially true when comparing the temperatures of the top membrane. This was the result of the added mass serving as a heat sink. This effected the expansion of the top and bottom membranes. The engine without added mass had far greater membrane expansion. Additionally, the ringouts present in the micro-engine with added mass were absent from the standard micro-engine. This showed the mechanical results of adding mass to the system.

The engine with added mass was operated at 60, 80, and 90 Hz with the same energy input per cycle. The membrane deflections were recorded. Figure 8.4 shows the recorded deflections with respect to time. There are several key points. First, the overall deflections were significantly lower than similar engines operated without added mass. Second, as operating speed increased, the number of ringouts decreased as the micro-engine natural frequency was approached. Plotting the pressure-volume data for these sub-resonant conditions produced curves of great complexity. Once resonant speed was attained, however, the curves became more recognizable. Figure 8.5 shows the micro-engine pressure-volume curve near resonance at 90 Hz. The compression portion of the cycle can be easily noted as can the constant volume heat addition resulting from the electric heat input. The resonant frequency for this

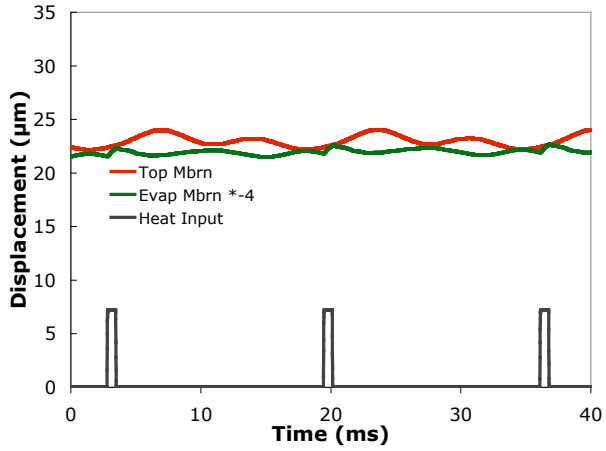

(a) 60Hz

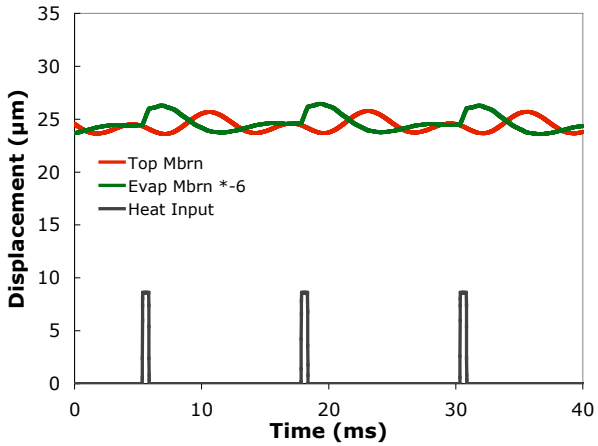

(b) 80Hz

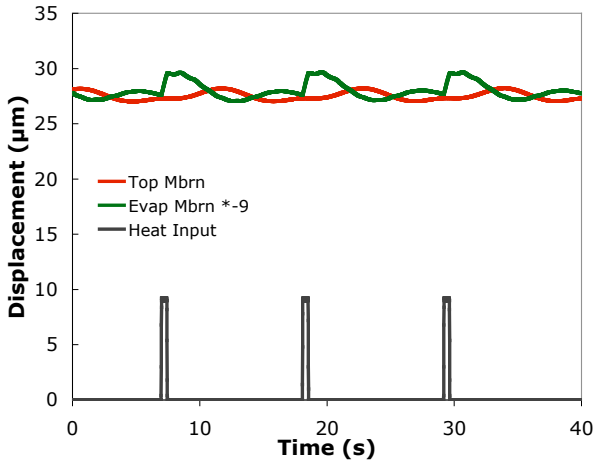

(c) 90Hz

Figure 8.4: Engine with Added Mass Operating at Increasing Frequency

micro-engine was 100 Hz. Figure 8.6 shows the out of phase deflection plots given 2 mJ input per cycle. Operation at the micro-engine resonant frequency produced the expected pressure-volume curve as well. Figure 8.7 shows the thermodynamic cycle of this engine at resonance.

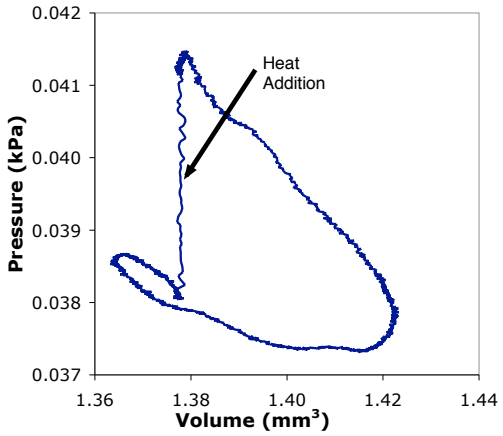

Figure 8.5: 90 Hz Pressurve-Volume Curve for an Engine Near Resonance

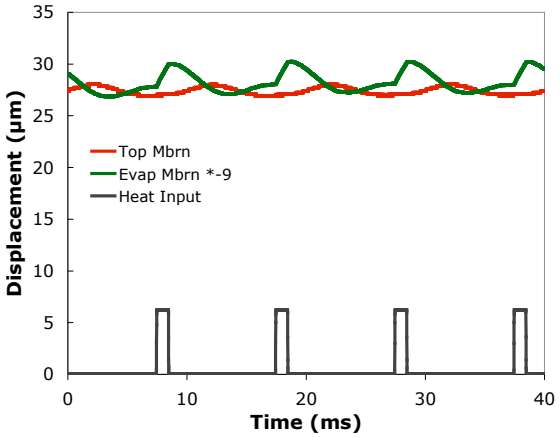

Figure 8.6: Engine with Added Mass Operating at Resonant Frequency, 100 Hz

As operating frequency increased beyond the resonant frequency of the micro-engine, however, the pressure and volume began to operate in phase. Figure 8.8 shows the membrane deflections and heat input location for this "super" resonance operating condition. Operation of the micro-engine at super-resonance returned the operating cycle to that of expansion without compression. It can be noted from Figure 8.8 that the increasing deflection of the evaporator membrane matched the increasing deflection of the top membrane. This placed the expansion of the micro-engine in phase with the increasing pressure. This operating mode was essentially the same as sub-resonant operation discussed in Chapter 7.

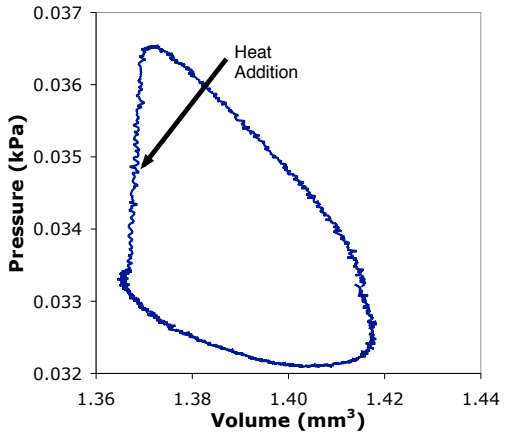

Figure 8.7: 100 Hz Pressurve-Volume Curve for an Engine at Resonance

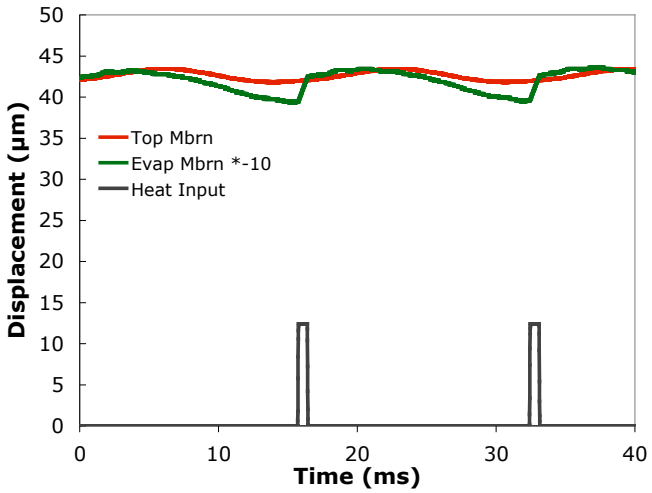

Figure 8.8: 120 Hz Operation of Engine with Added Mass

In summary, three different operating modes were noted during the frequency sweep performed on a micro-engine with added mass. The first showed multiple peaks, or expansions, between heat additions. This showed the engine ringing out as a result of heat addition. As the operating frequency increased, the number of peaks between heat additions declined until resonant frequency operation was achieved. Operation at resonant frequency produced the expected expansion and compression based cycle. The third operating mode was noted during micro-engine operation at frequencies above the resonant frequency. Operation at super-resonance returned the micro-engine to a cycle with pressure and volume in phase.

8.1.2 Resonant Cycles

There were a significant number of micro-engines constructed with added mass for the purpose of resonant operation. Overall, the cycles produced matched those discussed in Section 8.1.1 when the micro-engine was operated at resonant conditions. Each engine produced a slightly different resonant cycle from its peers. All, however, shared similar characteristics. These differences were the result of many factors including the actual engine components and assembly. There was one variation in the assembly of the micro-engines for these tests. Some were assembled using a 9 mm cross-type evaporator membrane while others used an 8 mm standard membrane. The results were indistinguishable and no effort was made to differentiate them in this section. All micro-engines were assembled with 5.5 g of added mass.

The pressure-volume plots in Figure 8.9 show several cycles obtained during the resonant operation of various micro-engines. The electrical heater supplied 3.1 mJ per cycle for the micro-engine operating at 120 Hz. 2.8 mJ per cycle was supplied to the micro-engine operating at 135 Hz. 2.6 mJ per cycle was supplied to the micro-engine operating at 140 Hz.

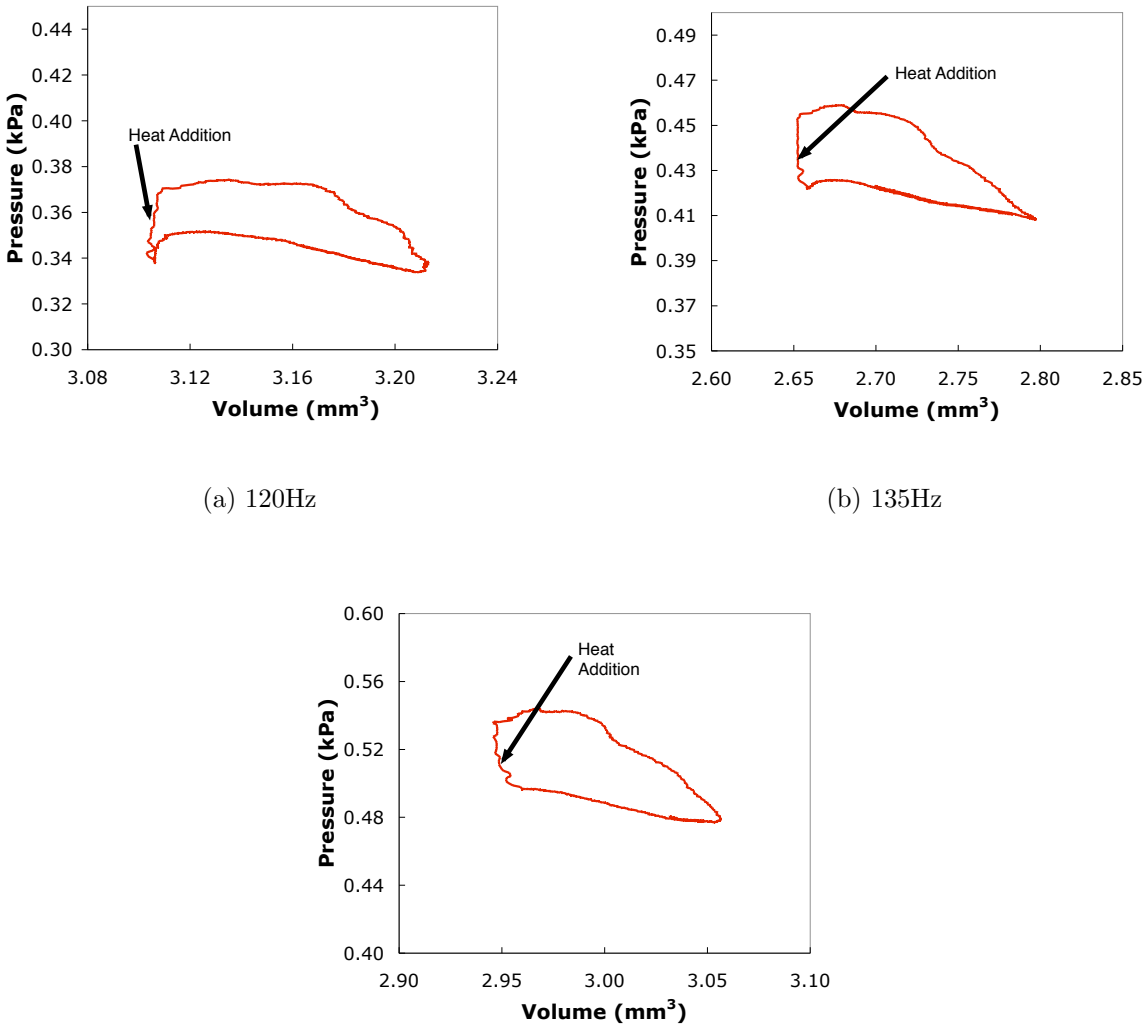

(a) 120Hz

(b) 135Hz

(c) 140Hz

Figure 8.9: Various Engine Resonant P-V Cycles

Generally, the cyclic work output from these operations was small, on the order of 1 μW. All showed the same basic characteristics of constant volume heat addition, expansion, and compression. An improved output of 6.7 μW was obtained from an engine operated at 125 Hz. Figure 8.10 shows the thermodynamic cycle obtained from the resonant operation of this micro-engine.

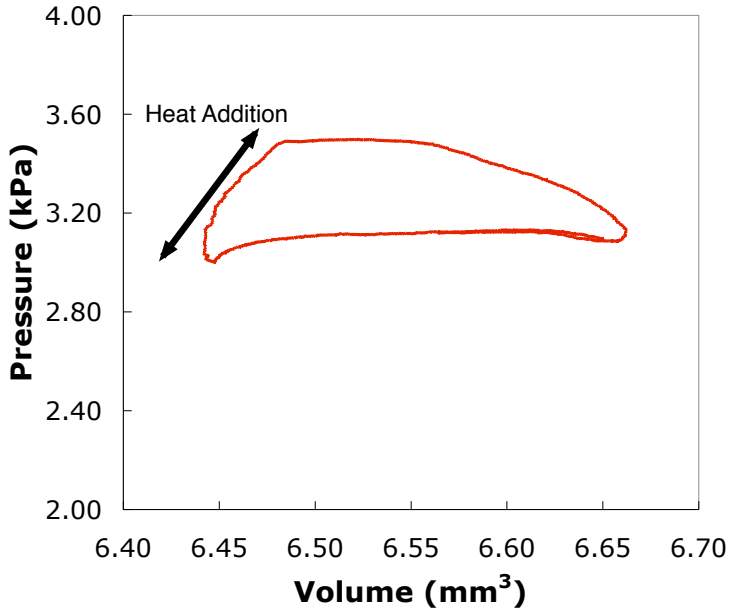

Figure 8.10: 125 Hz Engine Resonant Cycle

The cycle shown in Figure 8.10 shows slight variations as compared to others noted in this section. One difference is that the heat addition is not solely constant volume. By slightly varying the timing of the heat addition versus heat rejection, slight alterations in the engine thermodynamic cycle were possible. This particular micro-engine operated with a retarded heat addition, yielding the unusual result.

The cyclic power output from the resonating micro-engines was small. Nonetheless, their successful resonant operation showed the potential of this operating mode. Figure 8.11 shows the power outputs of various micro-engines operated at resonance. It should be noted that these micro-engines were each operated at resonant conditions, however, each engine had a slightly different resonant frequency. The range of operating frequencies represented in Figure 8.11 is 120 to 140 Hz.

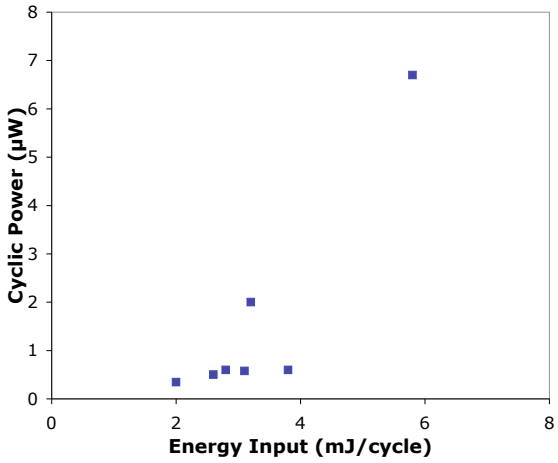

Figure 8.11: Cyclic Work Outputs During Resonant Frequency Operation

8.2 Thermal Switch Controlled Resonant Operation

To show the viability of resonant micro-engine operation from constant temperature heat sources, a micro-engine with added mass was placed above two thermal switches as detailed in Section 5.2.3. The cooling thermal switch was maintained at 14 °C. The heating thermal switch was maintained at 50 °C. The thermal switches used in these tests had liquid-metal droplets on their contacting surfaces. The electric heater on the evaporator membrane was not used during these experiments.

Two thermal switches were used in these resonant tests; one for heat addition and a second for heat rejection. In Section 7.4, the micro-engine was heated via thermal switch. That engine was unable to operate effectively over 25 Hz because active cooling was needed. To achieve resonant frequency operation near 100 Hz, a second switch was added to allow active heat rejection.

The micro-engines used in this work were assembled with 5.5 g of added mass and operated at their resonant frequencies. Figure 8.12 shows a typical pressure-volume plot from an engine resonating at 90 Hz.

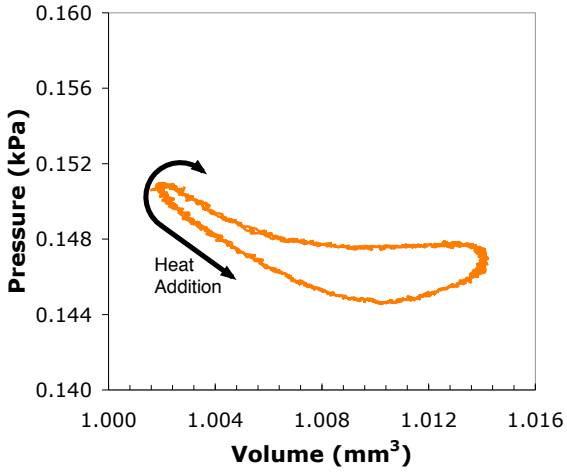

Figure 8.12: 90 Hz Resonant Cycle from Heat Sink Operation

As seen in Figure 8.12, micro-engine resonant operation from constant temperature heat sinks showed many of the same features as resonant operation using electric heat addition. Several differences were noted, however. First, the overall output was reduced. Chapter 6 noted several limitations of the thermal switch. These limitations adversely effected resonant operation. Not only was cooling limited, but limitations were introduced to the heat addition process as well. This resulted in poor heat transfer into and out of the micro-engines and reduced cyclic power. Figure 8.13 shows evaporator membrane temperatures (at resonant conditions) for a thermal switch controlled micro-engine operating at 80 Hz and an electrically heated micro-engine operating at 90 Hz.

The peak to peak temperature was .5 °C for the engine heated and cooled by thermal switches. The peak to peak temperature was 1.5 °C for the engine heated electrically and cooled via thermal switch. Not only was the peak to peak temperature reduced when heated via switch, but the average temperature of the micro-engine increased. This was the result of continuous heat "leakage" across the gap between high-temperature switch and evaporator membrane. The lower peak to peak temperature resulted in reduced cycle work.

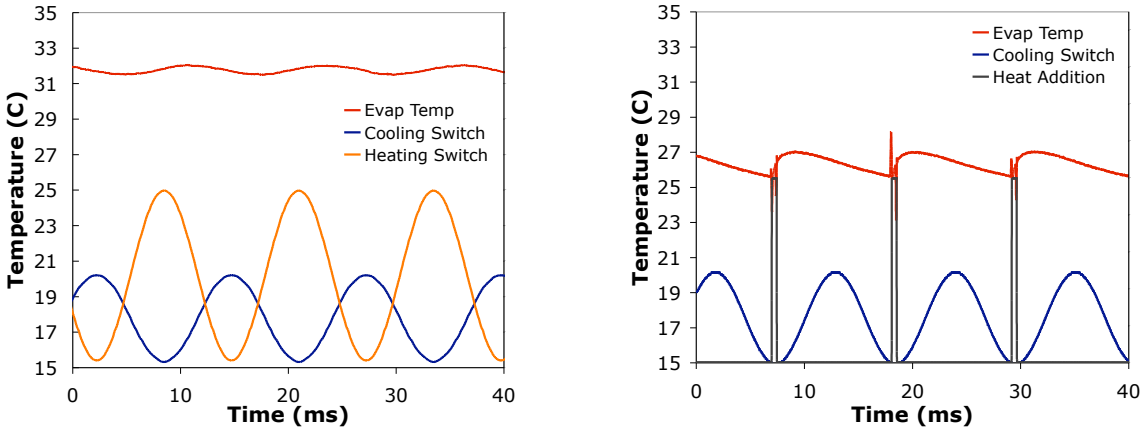

(a) 80 Hz, Two Switches

(b) 90 Hz, Electrically Heated

Figure 8.13: Engine Temperatures at Resonance

Second, while the basic shape of the cycle remained the same (including a compression and expansion component), the constant volume heat addition was lost. This was due to the action of the heating thermal switch. The heat addition switch showed a variable heating similar to the variable cooling of the cooling switch. The slow and variable heating and cooling resulted in the oval shape of Figure 8.12 and the temperature profiles in Figure 8.13 as well. Compared to the fast temperature rise of the electrically heated micro-engine, the switch controlled micro-engine demonstrated a more sinusoidal temperature trace.

In summary, the cyclic output from resonating micro-engines operated from two constant temperature heat sinks was small. The possibility of resonant operation via thermal switch was demonstrated, however. The basic behavior of these micro-engines during resonance was similar to electrically heated engines. However, there were differences due to the altered nature of the heat transfer into the engine.

Chapter 9

Conclusions

9.1 Conclusions

A micro-engine has been operated with a thermal switch integrated to allow active heat rejection. Compared to engines operating with passive heat rejection, micro-engine operating temperatures were reduced while peak to peak top membrane deflections increased 20 %. Maximum operating frequency increased from 40 Hz to over 100 Hz. The thermal switch was found to have a thermal resistance ratio $R_{off}/R_{on} = 3$ and a maximum heat transfer capacity of 200 mW.

The micro-engine was operated in two modes. The first was sub-resonant operation. The second was resonant operation. During sub-resonant operation, the thermal switch was used to actively reject heat. Several micro-engine designs were constructed and tested including engines fabricated with 5 mm side-length top membranes and 10 mm side-length top membranes. Additionally, different wick heights were employed on the evaporator membrane to aid working fluid evaporation. The maximum power output was 2.6 mW obtained from a

micro-engine operating at 100 Hz with a 10 mm side-length, silicon top membrane and 40 μm high wicks. The maximum operating efficiency obtained was .15 % for a micro-engine operating at 100 Hz using a 5 mm side-length silicon-nitride top membrane and 10 μm high wicks. Maximum applied force was also studied using a micro-engine fabricated with a 10 mm side-length, silicon nitride top membrane. Maximum applied force was 43 mN at 20 Hz.

The use of the thermal switch to control heat addition to the micro-engine from a constant temperature heat source was investigated. Operation from a heated source maintained at 60 °C showed a maximum power output of 350 μW at 16 Hz. Due to a lack of heat rejection, power output from the micro-engine was found to decline significantly at frequencies above 25 Hz.

Operation at resonance was made possible through mass added to the micro-engine top membrane and the increased heat rejection attained via thermal switch integration. Engine resonant frequencies varied dependent on the micro-engine, however, most ranged between 100 and 130 Hz. Resonant cycles showed compression and expansion processes. Electrically heated resonant operation showed nearly constant volume heat addition. The maximum cyclic work measured during resonant operation was 6.7 μW from an electrically heated micro-engine operating at 125 Hz.

Micro-engines were also operated at resonance from constant temperature heat sources. Two thermal switches were used and maintained at 50 °C and 14 °C. The switches were allowed to control heat transfer to/from the micro-engine. The resulting resonant cycle showed some of the same characteristics as resonant cycles from electrically heated micro-engines. The cycle included both an expansion and compression event. Resonant operation from two constant temperature heat sinks showed the possibility of operating the micro-engine as intended in the original concept.

9.2 Observations and Recommendations

The combined micro-engine and thermal switch system is one that contains tradeoffs. Many attempts to improve operation resulted in the performance reduction of some other aspect of operation. Because of this, care must be taken when designing and operating these engines. Based on the results obtained during this work, the following observations and recommendations are included.

9.2.1 Sub-resonant Operation

The successful operation of the micro-engine at any condition (sub-resonance or resonance) is dependent on the successful heat transfer into and out of the device. The micro-engine showed some success operating from a constant temperature heat source at sub-resonant conditions. To amplify this success, improved heat transfer is needed into and out of the micro-engine. The thermal switch was shown to have several limitations when integrated fully with the engine, despite notably improved engine performance. Improving the conduction between evaporator membrane and switch is key to micro-engine output. While the addition of micro-droplets on the switch surface was shown to improve switch operation outside of the engine environment, they showed little effect during engine operation. Because of the dynamic nature of switch translation, the vibrations associated with its operation may play a role in determining its effective contact with the evaporator membrane. Attempting to eliminate any vibration resulting from switch operation may improve its performance.

9.2.2 Resonant Operation

As discussed in Section 9.2.1, the thermal switch limitations apply equally to resonant operation. In addition to thermal switching issues, the construction of micro-engines for resonant operation included an additional operating limitation. The added mass, placed atop the top membrane to reduce the resonant frequency of the device, had the positive effect of reducing natural frequency as intended. However, the added mass also provided a large heat sink that hampered performance. This was obvious in the small cyclic work outputs from engines operating at resonant conditions. The low temperatures recorded during operation, particularly from the top membrane, indicated this mass to be the source of the problem. Improved operation could be attained by establishing an improved thermal isolation of the added mass from the micro-engine. The clay buffer used in these tests had a low conductivity, however, its large area of surface contact allowed heat transfer to the added mass.

There exist a few possibilities to improve this situation. Any reduction in surface area contact between top membrane and added mass should result in higher cyclic work output. This is a complicated proposition, however; the top SiNx membranes used in resonant operation were particularly likely to break when contacted with small, sharp areas. They also showed an ability to deform around structures placed on them. This presents a problem when attempting to limit contact as the membrane can easily re-establish contact because of its flexibility. While the challenges associated with resonant engine operation are fundamental, fixing them requires some ingenuity.

Bibliography

[1] S. Beeby, M. Tudor, and N. White, "Energy harvesting vibration sources for microsystems applications," *Measurement Science and Technology*, vol. 17, no. 12, pp. R175–R195, 2006.

[2] J. Heywood, *Internal Combustion Engine Fundamentals*. McGraw-Hill, Inc, 1988.

[3] J. Heywood, *Internal Combustion Engine Fundamentals*, pp. 733–736. McGraw-Hill, Inc, 1988.

[4] A. Epstein, S. Jacobson, J. Protz, and L. Frchette, "Shirtbutton-sized gas turbines: The engineering challenges of micro high speed rotating machinery," *Proceedings of the 8th Int'l Symposium on Transport Phenomena and Dynamics of Rotating Machinery (ISROMAC'8), Honolulu, Hawaii,*, 2000.

[5] H. Aichlmayr, D. Kittelson, and M. Zachariah, "Miniature free-piston homogenious charge compression ignition engine-compressor concept -part 1: performance estimation and design considerations unique to small dimensions," *Chemical Engineering Science*, vol. 57, pp. 4161–4171, 2002.

[6] C. Lee, K. Jiang, P. Jin, and P. Prewett, "Design and fabrication of a micro wankel engine using mems technology," *Micro-electronic Engineering*, vol. 73-74, pp. 529–534, 2004.

[7] L. Frechette, C. Lee, S. Arslan, and Y. Liu, "Design of a microfabricated rankine cycle steam turbine for power generation," *Proceedings of the 2003 ASME IMECE*, no. IMECE2003-42082, 2003.

[8] H. Fujita, "Microactuators and micromachines," *Proceedings of the IEEE*, vol. 86, no. 8, 1998.

[9] E. Muntz, G. Shiflett, D. Erwin, and J. Kunc, "Transient energy-release pressure-driven microdevices," *Journal of Microelectromechanical Systems*, vol. 1, no. 3, pp. 155–163, 1992.

[10] S. Jacobson and A. Epstein, "An informal survey of power mems," *The International Symposium on Micro-Mechanical Engineering*, December 1-3, 2003.

[11] J. Cui, Y. Wei, X. Zheng, H. Wang, and Y. Wu, "The study on mems-based micro pump technology," *Proceedings of SPIE, 2005*, vol. 6040, 2005.

[12] X. Yang, C. Grosjean, and Y. Tai, "A low power mems silicone/parylene valve," *Solid-State Sensor and Actuator Workshop, Hilton Head Island, SC, June 7-11, 1998*, 1998.

[13] P. Bergstrom, J. Ji, Y. Liu, M. Kaviany, and K. Wise, "Thermally driven phase-change microactuation," *Journal of Microelectromechanical Systems*, vol. 4, no. 1, pp. 10–17, 1995.

[14] X. Yang, C. Grosjean, and Y. Tai, "Design, fabrication, and testing of micromachined silicone rubber membrane valves," *Journal of Microelectromechanical Systems*, vol. 8, no. 4, pp. 393–402, 1999.

[15] W. Sim, H. Yoon, O. Jeong, and S. Yang, "A phase-change type micropump with aluminum flap valves," *Journal of Micromechanics and Microengineering*, vol. 13, pp. 286–294, 2003.

[16] L. Klintberg, M. Karlsson, L. Stenmark, J. Schweitz, and G. Thornell, "A large stroke, high force paraffin phase transition actuator," *Sensors and Actuators A*, vol. 96, pp. 189–195, 2002.

[17] A. Henning, "Comprehensive model for thermopneumatic actuators and microvalves," *Journal of Microelectromechanical Systems*, vol. 15, no. 5, pp. 1308–1318, 2006.

[18] S. Whalen, C. Richards, D. Bahr, and R. Richards, "Characterization and modeling of a microcapillary driven liquidvapor phase-change membrane actuator," *Sensors and Actuators A*, vol. 134, pp. 201–212, 2007.

[19] M. Kim, Y. Lee, B. Lee, D. Sohn, and K. Kuk, "Actuating performance of non-passivated micro heaters," *Proceedings of the IMECE2006, November 5-10, 2006, Chicago*, no. IMECE2006-13505, 2006.

[20] Y. Song and T. Zhao, "Modeling and test of a thermally-driven phase-change non-mechanical micro pump," *Journal of Micromechanics and Microengineering*, vol. 11, pp. 713–719, 2001.

[21] Y. Çengel and M. Boles, *Thermodynamics an Engineering Approach.* McGraw Hill, fifth ed., 2006.

[22] M. Strasser, R. Aigne, C. Lauterhach, T. F. Stvr, M. Franosch, and G. Wachutka, "Micromachined cmos thermoelectric generators as on-chip power supply," *TRANSDUCERS '03. The 12th International Conference on Solid State Sensors, Actualors and Microsystems, Boston. June 8-12,2003*, pp. 45–48, 2003.

[23] V. Leonov, P. Fiorini, S. Sedky, T. Torfs, and C. V. Hoof, "Thermoelectric mems generators as a power supply for a body area network," *TRANSDUCERS'O5. The 13th International Conference on Solid-state Sensors, Actuators and Microsystems, Seoul, Korea, June 5-9,2005*, pp. 291–294, 2005.

[24] N. Satol, H. Ishii, M. Urano, T. Sakata, J. Teradal, H. Morimura, S. Shigematsu, K. Kudou, T. Kamei, and K. Machida, "Novel mems power generator with integrated thermoelectric and vibrational devices," *TRANSDUCERS'O5. The 13th Intemarional Conference on Solid-state Sensors, Actuators and Microsystems, Seoul, Korea, June 5-9,2005*, vol. 77, pp. 295–298, 2005.

[25] W. Wang, F. Jia, Q. Huang, and J. Zhang, "A new type of low power thermoelectric micro-generator fabricated by nanowire array thermoelectric material," *Microelectronic Engineering*, vol. 77, pp. 223–229, 2005.

[26] H. Bottner, J. Nurnus, A. Gavrikov, G. Kuhner, M. Jagle, C. Kunzel, D. Eberhard, G. Plescher, A. Schubert, and K. Schlereth, "New thermoelectric components using microsystem technologies," *Journal of Microelectromechanical Systems*, vol. 13, no. 3, pp. 414–420, 2004.

[27] H. Fang, L. Liu, and T. Ren, "Modeling and design optimization of large-deflection piezoelectric folded cantilever microactuators," *IEEE Transactions on Ultrasonics, Ferroelectrics, and Frequency Control*, vol. 53, no. 1, 2006.

[28] L. Zheng and M. Lu, "A large-displacement cmos micromachined thermal actuator with comb electrodes for capacitive sensing," *Sensors and Actuators A*, vol. 136, pp. 697–693, 2007.

[29] V. Dhuler, E. Hill, and A. Cowen, "In-plane mems thermal actuator and associated fabrication methods," *US Patent 6211598*, 1999.

[30] G. Gray and P. Kohl, "Modeling and performance of a magnetic mems wiping actuator," *Journal of Microelectromechanical Systems*, vol. 15, no. 4, pp. 904–911, 2006.

[31] Y. Zhang, G. Ding, S. Fu, and B. Cai, "A fast switching bistable electromagnetic microactuator fabricated by uv-liga technology," *Mechatronics*, vol. 17, pp. 165–171, 2005.

[32] J. Wright, Y. Tai, and S. Chang, "A large-force, fully-integrated mems magnetic actuator," *TRANSDUCERS '97, 1997 lnternational Conference on Solid-state Sensors and Actuators Chicago, June 16-19*, pp. 793–796, 1997.

[33] C. Jeon, J. Park, S. Lee, and C. Moon, "Fabrication and characteristics of out-of-plane piezoelectric micro grippers using mems processes," *Thin solid Films*, vol. 515, pp. 4901–4904, 2007.

[34] J. Baborowski, "Microfabrication of piezoelectric mems," *Journal of Electroceramics*, vol. 12, pp. 33–51, 2004.

[35] Q. Zhang, S. Gross, S. Tadigadapa, T. Jackson, F. Djuth, and S. Trolier-McKinstry, "Lead zirconate titanate films for d33 mode cantilever actuators," *Sensors and Actuators A*, vol. 105, pp. 91–97, 2003.

[36] S. Gross, S. Tadigadapa, T. Jackson, S. Trolier-McKinstry, and Q. Zhang, "Lead-zirconate-titanate-based piezoelectric micromachined switch," *Applied Physics Letters*, vol. 83, no. 1, pp. 174–176, 2003.

[37] N. Conway, Z. Traina, and S.-G. Kim, "A strain amplifying piezoelectric mems actuator," *Journal of Micromechanics and Microengineering*, vol. 17, pp. 781–787, 2007.

[38] Y. Lai, E. Bordatchev, S. Nikumb, and W. Hsu, "Performance characterization of in-plane electro-thermally driven linear microactuators," *Journal of Intelligent Materials Systems and Structures*, vol. 17, no. 10, pp. 919–929, 2006.

[39] A. Mehra, X. Zhang, A. Ayon, I. Waitz, M. Schmidt, and C. Spadaccini, "A six-wafer combustion system for a silicon micro gas turbine engine," *J.MEMS*, vol. 9, no. 4, 2000.

[40] S. Zhang and J. Wang, "Novel micro free-piston swing engine and its feasibility validation," *Tsinghua Science and Technology*, vol. 10, no. 3, pp. 381–386, 2005.

[41] K. Fu, A. J. Knobloch, F. Marinez, D. Walther, C. Fernandez-Pello, A. Pisano, and D. Liepmann, "Design and fabrication of a silicon-based mems rotary engine," *Proceedings of the 2001 ASME IMECE*, vol. 2001, no. MEMS-23925, 2001.

[42] L. Frechette and C. Lee, "Design of a microfabricated rankine cycle steam turbine for power generation," *Proceedings of the 2003 ASME IMECE,*, vol. 2003, no. IMECE2003-42082, 2003.

[43] K. Isomura, S. Tanaka, S. Togo, H. Kanebako, M. Murayama, N. Saji, F. Sato, and M. Esashi, "Development of micromachine gas turbine for portable power generation," *JSME International Journal, Series B*, vol. 47, no. 3, 2004.

[44] H. Aichlmayr, D. Kittelson, and M. Zachariah, "Miniature free-piston homogenious charge compression ignition engine-compressor concept -part 2: modeling hcci combustion in small scales with detailed homogeneous gas phase chemical kinetics," *Chemical Engineering Science*, vol. 57, pp. 4173–4186, 2002.

[45] D. Lee, D. Park, E. Yoon, and S. Kwon, "A mems piston-cylinder device actuated by combustion," *Journal of Heat Transfer*, vol. 125, pp. 487–193, 2003.

[46] D. Lee, D. Park, J. Yoon, S. Kwon, and E. Yoon, "Fabrication and test of a mems combustor and reciprocating device," *Journal of Micromechanics and Microengineering*, vol. 12, pp. 26–34, 2002.

[47] K. Fu, A. Knobloch, F. Martinez, D. Walther, C. Fernandez-Pello, A. Pisano, and D. Liepmann, "Design and fabrication of a silicon-based mems rotary engine," *Proceedings of the ASME Int'l Mech Eng Congress and Expo, New York*, 2001.

[48] J. Heppner, D. Walther, and A. Pisano, "Arctic: A rotary compressor thermally insulated μcooler," *Proceedings of the IEEE Int. Conf. Micro Electro Mech. Syst.*, vol. 7, no. MEMS2005, pp. 287–294, 2001.

[49] L. Frechette, C. Lee, S. Arslan, and Y. Liu, "Preliminary design of a mems steam turbine power plant-on-a-chip," *PowerMEMS'03. Technical Digest*, 2003.

[50] T. Yamamoto, T. Furuhata, N. Arai, and K. Mori, "Design and testing of the organic rankine cycle," *Energy*, vol. 26, pp. 239–251, 2001.

[51] T. Hung, "Waste heat recovery of organic rankine cycle using dry fluids," *Energy Conversion and Management*, vol. 42, pp. 539–553, 2001.

[52] B. Liu, K. Chien, and C. Wang, "Effect of working fluids on organic rankine cycle for waste heat recovery," *Energy*, vol. 29, pp. 1207–1217, 2004.

[53] T. Slater, P. V. Gerwen, E. Masure, F. Preudhomme, and K. Baert, "Thermomechanical characteristics of a thermal switch," *Solid-State Sensors and Actuators*, vol. 2, pp. 341–344, 1995.

[54] M. Beasley, S. Firebaugh, R. Edwards, A. Keeney, and R. Osiander, "Mems thermal switch for spacecraft thermal control," *MEMS/MOEMS Components and Their Applications, Proceedings of SPIE*, vol. 5344, 2004.

[55] C. Hilbert, R. Nelson, J. Reed, B. Lunceford, A. Somadder, K. Hu, and U. Ghoshal, "Thermoelectric mems coolers," *16th International Conference on Thermoelectrics*, pp. 117–122, 1999.

[56] U. Ghoshal, "Solid state thermal switch.," *US Patent 6429137*, 2002.

[57] L. Weiss, J. Cho, K. McNeil., D. Bahr, C. Richards, and R. Richards, "Characterization of a dynamic micro heat engine with integrated thermal switch," *Journal of Micromechanics and Microengineering*, vol. 16, pp. S262–S269, 2006.

[58] A. Christensen, J. Jacob, C. Richards, D. Bahr, and R. Richards, "Fabrication and characterization of a liquid-metal micro-droplet thermal switch," *TRANSDUCERS '03, The 12th lnternalional Conference on Solid State Sensors, Actuators and Microsystems, Boston. June 8-12, 2003*, 2003.

[59] J. Cho, L. Weiss, D. Bahr, C. Richards, and R. Richards, "Power production by a dynamic micro heat engine with an integrated thermal switch," *Journal of Micromechanics and Microengineering*, vol. 17, 2007.

[60] J. Darabi, M. Ohadi, and D. DeVoe, "An electrohydrodynamic polarization micropump for electronic cooling," *Journal of Microelectromechanical Systems*, vol. 10, no. 1, pp. 98–106, 2001.

[61] J. Cheng, C. Leu, Y. Chao, and R. Tain, "Cooling performance of silicon-based thermoelectric device on high power led," *IEEE 2005 International Conference on Thermoelectrics*, 2005.

[62] D. Slasky, "Thermal switches and methods for improving their performance," *US Patent 6247524*, 2001.

[63] E. Smith, J. Parpia, and J. Beamish, "^{3}he gas heat switch for use in a cyclic magnetic refrigerator.," *Journal of Low Temperature Physics*, vol. 119, no. 3-4, 2000.

[64] S. Whalen, *Cycle Work from a MEMS Heat Engine and Characterization of the Liquid-vapor Phase Change Actuation Mechanism*. PhD thesis, Washington State University, 2004.

[65] D. Kim, K. Lee, T. Kwon, and S. Lee, "Micro-channel filling flow considering surface tension effect," *Journal of Micromechanics and Microengineering*, vol. 12, pp. 236–246, 2002.

[66] J. Vlassak and W. Nix, "A new bulge test technique for the determination of young's modulus ratio of thin film," *Journal of Material's Research*, vol. 7, no. 12, pp. 3242–3249, 1992.

[67] T. Hsu, *MEMS and Microsystems Design and Manufacture*. McGraw Hill, first ed., 2002.

[68] J. Judy, "Microelectromechanical systems (mems): Fabrication, design, and applications," *Smart Materials and Structures*, vol. 10, pp. 1115–1134, 2001.

[69] T. Kovacs, *Micromachined Transducers Sourcebook*. WCB McGraw Hill, first ed., 1998.

[70] T. A. Quy, "Characterization of micro-capillary wicking evaporators," Master's thesis, Washington State University, 2006.

[71] D. Carpenter, "Fabrication and characterization of a micro capillary evaporator for mems based power generation," Master's thesis, Washington State University, 2004.

[72] A. Reisman, M. Berkenblit, S. A. Chan, F. B. Kaufman, and D. C. Green, "The controlled etching of silicon in catalyzed ethylenediamine-pyrocatechol-water solutions," *Journal of the Electrochemical Society*, vol. 126, no. 8, pp. 1406–1415, 1979.

[73] J. Cho, T. Wiser, C.Richards, D. Bahr, and R. Richards, "Fabrication and characterization of a thermal switch," *Sensors and Actuators A*, vol. 133, pp. 55–63, 2007.

[74] K. Rainey, S. You, and S. Lee, "Effect of pressure, subcooling, and dissolved gas on pool boiling heat transfer from microporous surfaces in fc-72," *Journal of Heat Transfer*, vol. 125, pp. 75–83, 2003.

[75] M. Robinson, *Microstructural and Geometric Effects on the Piezoelectric Performance of PZT MEMS*. PhD thesis, Washington State University, 2007.

[76] H. Bardaweel, R. Richards, L. Weiss, and C. Richards, "Characterization and modeling of the dynamic behavior of a liquid-vapor phase change actuator," *Proceedings of IMECE07*, no. IMECE2007-42567, pp. 1–7, 2007.

Appendices

Appendix A

Cantilever Engine Operation and Results

This appendix reviews the construction, operation, and output of a modified micro-engine not discussed in the main dissertation text. This alternative engine was constructed using a PZT cantilever in place of the typical top membrane. There were several reasons for the examination of this cantilever engine, however, the primary motivation was to assess the viability of resonant frequency reduction via the added mass and flexibility of the cantilever. Overall the results were encouraging. This "cantilever engine" was shown to resonate at relatively low frequencies around 60 Hz and output about 19 μW of cycle work.

A.1 Cantilever Engine Construction and Operation

While a significant amount of the construction and testing of the cantilever engine closely resembled that of the standard micro-engine, there were a few key differences. This section examines the assembly and test setup of the cantilever engine.

A.1.1 Cantilever Engine Assembly

The cantilever engine was assembled using many of the same components used on the micro-engine. A standard 8 mm evaporator membrane was used as the cantilever engine lower bound. The evaporator membrane was equipped with 10 μm high wicks. A 75 μm cavity of semi-conductor tape was placed above the evaporator membrane as typical. The top membrane was replaced with a PZT cantilever. The cantilever was the same type used to actuate thermal switches as described by Cho *et al.* [59].

The evaporator membrane and semi-conductor tape cavity were placed atop a lower engine carrier and fixed in place. This constituted the lower half of the cantilever engine, essentially the same as lower half constructions for typical micro-engines detailed in Section 4.1.

The top half of the engine was constructed with a PZT cantilever fixed to a glass slide as shown in Figure A.1. The glass cover slide served as the replacement for the typical top membrane and was bonded to the cantilever. A small piece of reflective gold was added to

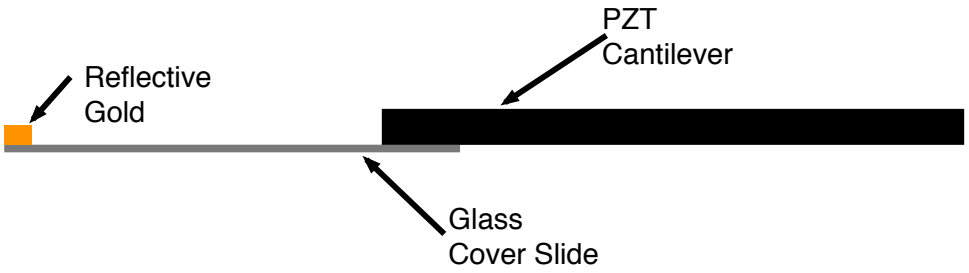

Figure A.1: Cantilever and Glass Slide

the tip of the cover slide. This allowed displacement measurements of the top slide/cantilever to be recorded via laser vibrometer. The cantilever was fixed to a set of rotational and z-axis stages similar to those used in thermal switch alignment and operation (Section 5.2.1).

The cantilever engine was assembled by placing the lower half beneath the cover-slide and bringing the cantilever/slide down into close proximity as shown in Figure A.2. The rota-

tional axis stage was used to assure parallel alignment between evaporator membrane and cover slide.

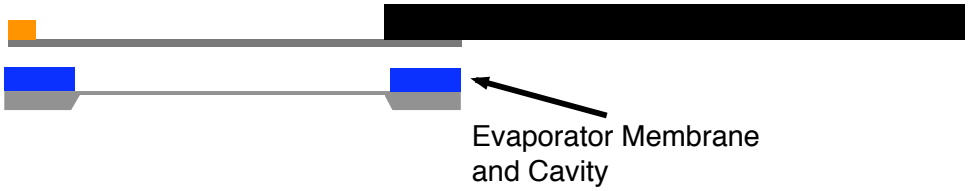

Figure A.2: Aligned Cantilever Engine Components

Like the standard micro-engine, working fluid was used to fill the cavity created by the semiconductor tape on the evaporator membrane. The working fluid used during these tests was 3M^{TM} FC77. Unlike the micro-engine, however, the cantilever engine employed a liquid seal between tape and cover slide. Figure A.3 shows this final assembled arrangement. The thickness of the liquid seal could be varied by adjusting the height of the cantilever and adding additional working fluid if needed.

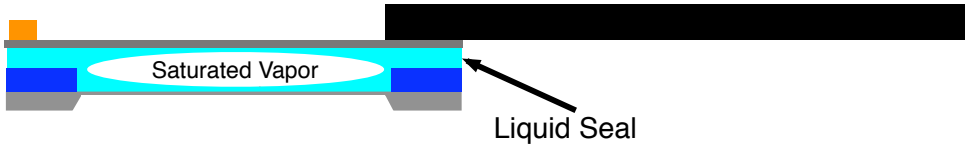

Figure A.3: Assembled Cantilever Engine

A.1.2 Experimental Procedures

The basic operation and test setup for cantilever engine operation is discussed in this section. There were many similarities to the operation of standard micro-engines, however, some differences are noted.

Cantilever Engine Operating Cycle

Like the standard micro-engine, the cantilever engine relied on heat addition to evaporate working fluid from the cavity. This increased cavity pressure and displaced the slide/cantilever as a result. The liquid seal and evaporator membrane also expanded as a result of heat addition. The cantilever engine was allowed to operate without active heat rejection. As a result, cooling after heat addition was due to passive heat rejection to the surroundings and conduction through the slide and cantilever.

As with the standard micro-engine, the cantilever engine could be operated at both sub-resonant and resonant conditions depending on operating frequency and liquid seal height. Sub-resonant operation of the cantilever engine was detailed by Bardaweel *et al.*, including the modeling of the system as a spring-mass-damper [76]. The liquid seal was key to achieving resonance. By increasing seal height (and thus adding working fluid), more mass was added to the system which reduced the cantilever engine natural frequency. The flexible nature of the seal also allowed more unrestricted movement of the slide and cantilever. This reduced the system stiffness and lowered the resonant frequency.

The resonant operating cycle showed many of the same characteristics as noted during the resonant operation of standard micro-engines. The pressure and volume de-coupled during resonant operation and resulted in compression and expansion cycle components.

Cantilever Engine Test Setup

Heat addition was controlled electrically via the resistance heater on the evaporator membrane. The controlling setup used in micro-engine operation was employed to operate the cantilever engine as well. Figure A.4 shows this basic setup. Calculations for determining heat addition amounts are located in Section 5.4.3.

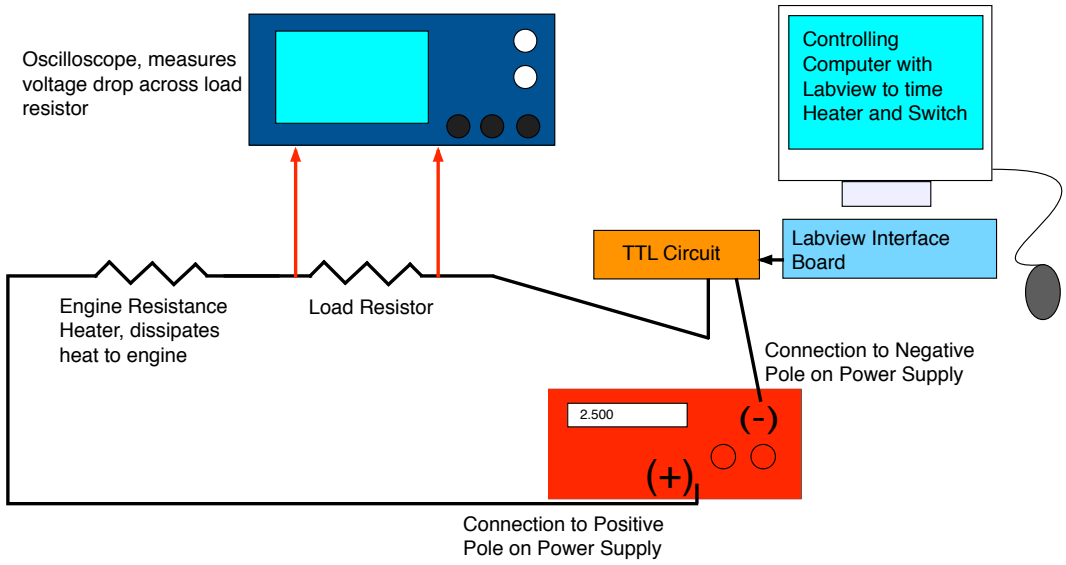

Figure A.4: Cantilever Engine Electrically Heated Setup

The laser-vibrometer was used to monitor the deflection of the slide/cantilever as well as the lower membrane. Figure A.5 shows this experimental setup. As with the standard

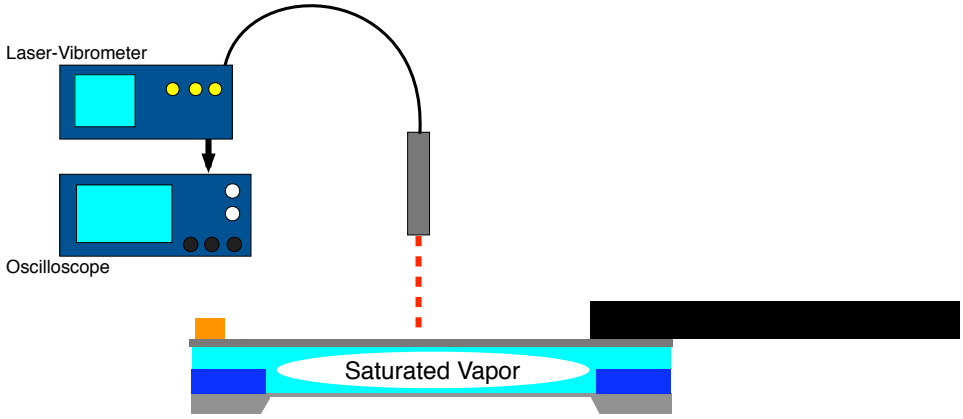

Figure A.5: Cantilever Engine and Vibrometer Setup

micro-engine, the vibrometer was focussed on either the reflective top gold piece (atop the cover slide), or on the evaporator membrane. The recorded deflections of these components were converted to volume and pressure as described in Section 5.4.2. Deflection of the lower membrane resulted in cavity pressure measurement. Deflection of the cover slide was used to determine the engine operating volume.

A.2 Cantilever Engine Operating Results

The cantilever engine was operated across a wide range of frequencies. The cavity thickness was adjusted to initiate resonant operation at 60 Hz. This section shows typical cantilever engine response at sub-resonant and resonant operation.

The cantilever engine was operated at 10 Hz (sub-resonance) and given 90 mJ of heat input. It was allowed to fully expand while the deflection of the cantilever was recorded. Figure A.6 shows the resultant deflection. The deflection plot resembled sub-resonant operation of micro-engines with added mass where a notable ringout was achieved.

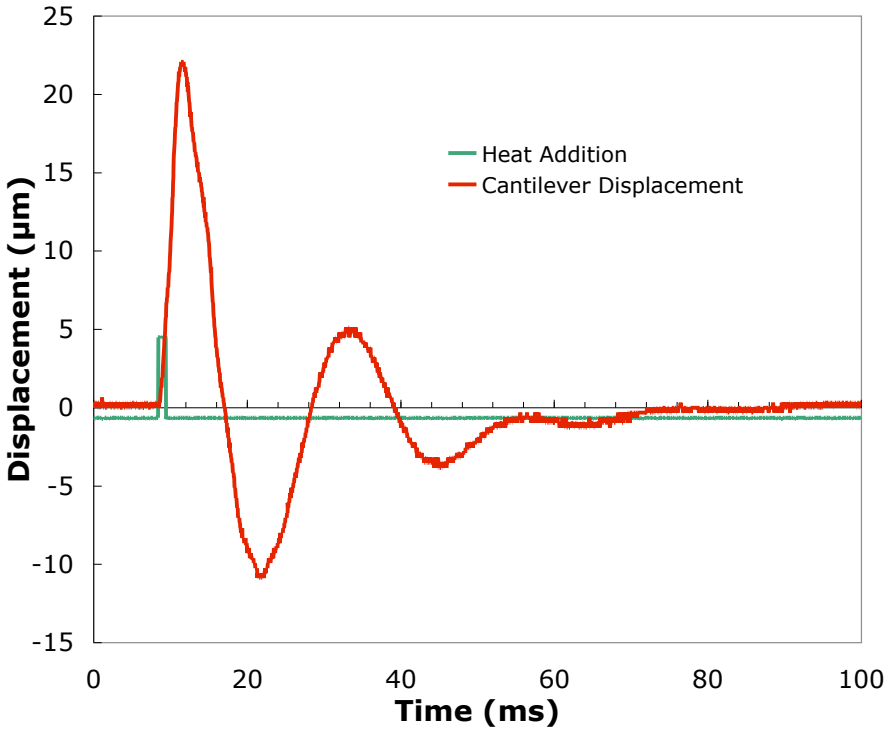

Figure A.6: Cantilever Engine 10 Hz Sub-resonant Operation

Unlike micro-engine operation, the cantilever showed that it could cross the "zero-plane" of deflection. This resulted in a negative deflection during parts of the ringout. This was due to the nature of the liquid seal. Because it was not rigid, it allowed negative displacement.

Also apparent from sub-resonant operation, the cantilever engine showed no tendency to operate with increased average deflection as input power increased. This behavior was again the result of the liquid seal. As operating temperature increased and average cavity pressure increased, the seal simply allowed the vapor within the cavity to expand and push the seal outwards. This resulted in the occasional need to replenish the seal with additional working fluid to maintain engine operation. Introduction of fresh working fluid to the seal also cooled the cavity, returning the cavity pressure to initial conditions. Seal replenishment was needed approximately two times per minute during typical operation.

Cantilever engine resonance was achieved by increasing the operating speed to 60 Hz and increasing the liquid seal thickness to nearly .5 mm. 24 mJ was delivered by the evaporator membrane resistance heater every cycle. Figure A.7 shows the resultant deflections of the cantilever and evaporator membrane. The de-coupled deflections are easily noted at this resonant condition.

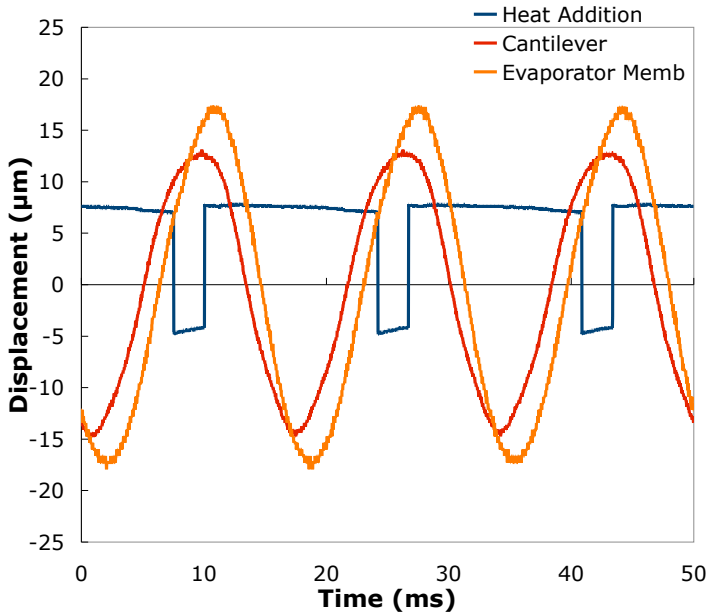

Figure A.7: Cantilever Engine 60 Hz Resonant Operation

The resonant operation of the cantilever engine produced 18.8 μW of cycle work as shown in Figure A.8.

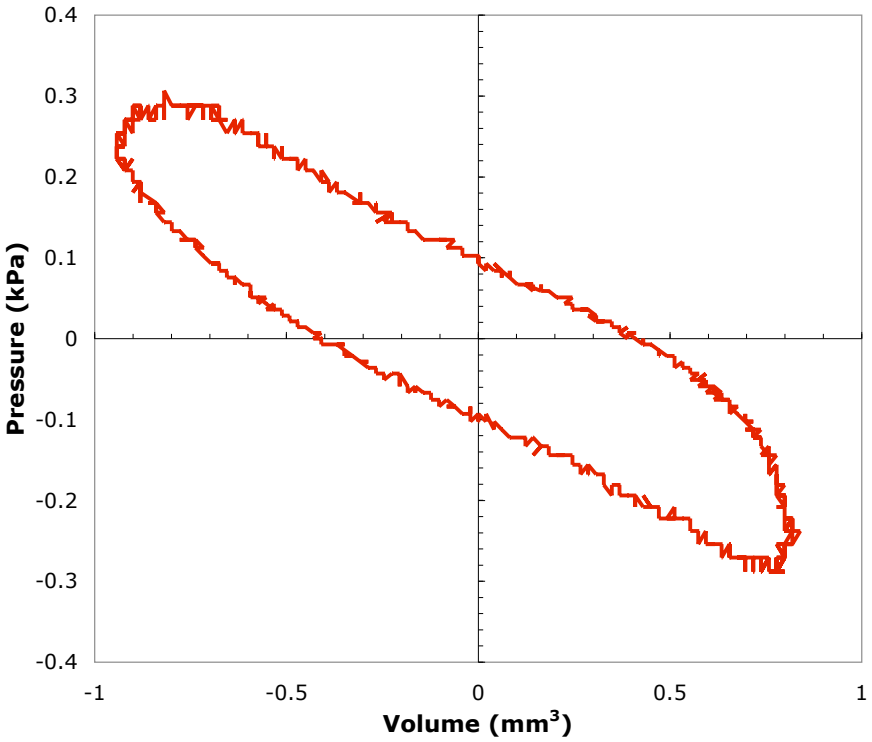

Figure A.8: Cantilever Engine Resonant Cycle

A clear compression and expansion were noted in the cyclic operation of the cantilever engine at resonance. This was similar to standard micro-engine resonant findings. Unlike the micro-engine, however, there was no constant volume heat addition. This was most likely due to the flexibility of the liquid seal which tended to absorb sudden impulses. An additional difference was the location of the pressure-volume curve about the origin. As noted during sub-resonant operation, the cantilever engine tended to operate about zero deflection. This resulted in the symmetrical centering of the pressure-volume curve.

A.3 Conclusions

The cantilever engine showed the ability to operate at resonant conditions and produced up to 18.8 μW of cyclic power. The basic resonant shape had the same compression and expansion features of standard micro-engine operations, however, lacked obvious constant volume heat addition. The use of a liquid seal allowed the resonant frequency of the engine to be adjusted. This was accomplished by increasing or decreasing the seal height and hence, the total amount of fluid present in the engine cavity.

The liquid seal was an interesting feature of this engine. It allowed increased flexibility and lower resonant frequencies, however, also robbed the engine of power output. This was because increasing cavity pressure was just as likely to push the seal outwards as push the cantilever upwards. This remained the biggest challenge in cantilever engine operation.

Appendix B

Error and Uncertainty Calculation

The details of error and uncertainty analysis are presented in this Appendix. Where applicable, engines constructed using 5 mm and 10 mm side-length top membranes were used to determine values. Micro-engines were assumed to operate with a 10 V electrical input and a 10 % duty cycle. 100 or 40 Hz was used as the micro-engine operating frequency. These operating points present a standard set of inputs for the sake of uncertainty calculation. Although operated over a range of inputs, uncertainty and error change little as a result. A Root Sum Squares (RSS) method was used to determine the total uncertainty associated with many of the uncertainty calculations. The basic form of the RSS equation is shown in Equation B.1.

$$w_R = \sqrt{\sum_{i=1}^{n} \left(\frac{\partial F}{\partial x_i} w_{xi} \right)^2} \tag{B.1}$$

w_R: Uncertainty
n: Number of contributing variables
F: Original equation for which uncertainty is being calculated
x_i: F is a function of variables, $x_i \cdots x_n$
w_{xi}: Uncertainty associated with variable x_i

The uncertainties discussed in the first sections of this appendix (B.1, B.2) pertain to measurements and calculations related to any single micro-engine. Performance variation engine-to-engine is discussed and calculated in Section B.3.

B.1 Measurement Uncertainties

The measurement uncertainties shown in Table 5.1 are detailed in this section.

B.1.1 Energy and Power Input

There are several sources of error that establish the total energy input uncertainty. A Fluke 189 True RMS multimeter was used to measure the value of the load resistor necessary to monitor input energy. The uncertainty of the multimeter was ±.005 Ω. A Tektronix 5034b oscilloscope (or equivalent) was used on a high resolution setting to monitor voltage drop across the load resistor. The uncertainty of this measurement was ±.002 mV. The current flow was calculated using Equation B.2.

$$I = \frac{\triangle V}{R_L} \tag{B.2}$$

I: Current
$\triangle V$: Measured voltage drop
R_L: Load resistor value

Applying Equation B.1 to Equation B.2 determined the uncertainty associated with current measurement. The calculated uncertainty was ±.003 A.

Instantaneous power was calculated using Equation B.3 where P represents the power. Application of Equation B.3 to Equation B.1 gave uncertainty of $\pm.03$ W.

$$P = I \triangle V \tag{B.3}$$

Using a 10 % duty cycle as a typical micro-engine operating point, an on-time of 1 ms was used for operation at 100 Hz. To determine the amount of energy input to the micro-engine per cycle, this 1 ms on-time was multiplied by the instantaneous power of .03 W. Equation B.1 was used to find the uncertainty. The power input uncertainty was determined to be $\pm.15$ mJ. Given operation at 100 Hz, this equated to an uncertainty of ± 15 mW for average power input or ± 6 mW for 40 Hz operation.

B.1.2 Deflection

Membrane deflection was measured using a Polytec OFV-5000 laser-vibrometer with DD-200 deflection decoding software. The resolution of the vibrometer given this setup was ± 2 nm for a 32 μm per Volt setting. The output was recorded by the oscilloscope with accuracy $\pm.002$ mV. For the purpose of maximum error, the largest deflection recorded during testing was 275 μm .

Given a 275 μm deflection, the voltage output from the vibrometer (as recorded by the oscilloscope) was 8.593751 V. Deflection was determined by multiplying the recorded vibrometer output by the linear vibrometer deflection slope (32 μm per Volt). Applying this to Equation

B.1 allowed the calculation of deflection uncertainty. Deflection uncertainty was determined to be ±17 nm.

B.1.3 RTD Temperature

The determination of RTD temperature was primarily experimental as each RTD was calibrated before use in the micro-engines. As the temperature of the RTD water bath was measured visually on a graduated thermometer, the accuracy was assumed to be accurate within a degree, or ±.5 °C. To calculate temperature based on RTD output, Equation B.4 was used.

$$T = V(R_{cal}) \tag{B.4}$$

T: RTD Temperature
V: Measured voltage output signal
R_{cal}: Calibrated RTD slope

The RTD calibration slope, or R_{cal}, had error associated with it due to the uncertainty of the thermometer reading. The slope of each RTD used in these experiments was examined and found to have an uncertainty of ± .3 for all cases. Noise in the recorded signal introduced .1 V of uncertainty into the measurements. 2 V was used as a typical RTD output voltage and the uncertainties of the temperature measurements were calculated using Equation B.1.

First, RTDs used on the micro-engine evaporator membranes were considered. Given the RTD calibration slope values, calibration slope error, and signal noise, the lower RTDs were found to have an accuracy of ±1.5 °C. The RTDs used on the top membranes were next considered. Based on their respective calibration slopes and errors, they were found to have an uncertainty of ±1.4 °C.

B.2 Calculation Uncertainties

Based on the known measurement uncertainties, the calculations supporting values listed in Table 5.2 are reviewed in this section.

B.2.1 Pressure

Engine operating pressure was determined as a function of the error associated with static bulge testing, membrane displacement, and pressure-deflection curves. Error associated with pressure measurement during bulge testing was due to the pressure sensor. The sensor had an error of ±.05 kPa. The error associated with the pressure-deflection curve was assumed negligible due to the high accuracy of the fitted line obtained from Labview. Equation B.5 shows the form of the pressure-deflection curve.

$$P = C_1\delta + C_2\delta^3 \tag{B.5}$$

C_1, C_2: Curve fit parameters
δ: Center point membrane deflection

The maximum recorded deflection of 275 μm (for a 10 mm micro-engine) and deflection uncertainty of ±17 nm was used to calculate the pressure uncertainty. Equation B.5 was applied to Equation B.1, yielding an uncertainty of $\pm 4.3 \times 10^{-6}$ Pa. Similarly insignificant error was calculated for 5 mm micro engines. Because of this, most error is due to the original pressure measurement during static bulge testing and determined to be ±.05 kPa.

B.2.2 Volume

The volume beneath a deflected membrane was determined in Section 5.4.1. This resulted in a linear relationship presented in Equation B.6.

$$V_{mem} = \alpha\delta \tag{B.6}$$

α: Constant based on membrane size
δ: Center point membrane deflection

The volume constant, α, was 1.26×10^{-5} for 5 mm side-length membranes. α was 5.05×10^{-5} for 10 mm membranes. Given these values and known deflection uncertainty, Equation B.1 was used to determine volume uncertainties. Volume uncertainty for a 5 mm micro-engine was $\pm.000214$ mm^3. Volume uncertainty for a 10 mm micro-engine was $\pm.000859$ mm^3.

B.2.3 Work

The work output from the micro-engine was determined as a function of pressure and volume. Equation B.7 shows the basic relationship. Equation B.7 was the basis for both sub-resonant and resonant work output calculations. Uncertainty for both modes is calculated in this section.

$$W = \int P dV \tag{B.7}$$

W: Work
P: Pressure
dV: Differential volume

For the purpose of uncertainty calculation, Equation B.7 was simplified to Equation B.8. This allowed a "worst case" uncertainty determination.

$$W = \triangle P \triangle V \tag{B.8}$$

Based on this simplified equation, Equation B.1 was used to calculate the uncertainty in the work calculation. Pressure and volume results from sub-resonant 5 mm and 10 mm micro-engine operation were used. $\triangle P$ was 20 kPa and $\triangle V$ was 2 mm^3 for 5 mm micro-engines. $\triangle P$ was 10 kPa and $\triangle V$ was 2.8 mm^3 for 10 mm micro-engines. 5 mm work output uncertainty was $\pm 1.0 \times 10^{-7}$ J. 10 mm work output uncertainty was $\pm 1.4 \times 10^{-7}$ J.

To determine the work uncertainty during resonant operation, $\triangle P$ was 1.5 kPa and $\triangle V$ was .5 mm^3. Based on these figures, the maximum work uncertainty for resonant operation was $\pm 2.5 \times 10^{-8}$ J.

B.2.4 Efficiency

The efficiency of micro-engine operation was defined as shown in Equation B.9.

$$\eta = \frac{W}{Q_{in}} \tag{B.9}$$

W: Work output
Q_{in}: Energy input

Typical values for 5 mm and 10 mm engine operation were assumed. For the 5 mm engine, work output was .03 mJ and heat input was 11.7 mJ. For the 10 mm engine, work output

was .041 mJ and heat input was 29.7 mJ. Using Equation B.1, 5 mm efficiency uncertainty was $\pm 8.56 \times 10^{-4}$ %. 10 mm efficiency uncertainty was $\pm 4.33 \times 10^{-4}$ %

B.2.5 Force Calculation

The peak force applied by a micro-engine was calculated via Equation B.10.

$$F = ma \tag{B.10}$$

F: Applied force
m: Mass
a: Acceleration

Curve fits with a high degree of accuracy were used to match the measured deflection values to a descriptive curve. Due to the high degree of accuracy, error from this process was assumed negligible. The error associated with acceleration was $\pm .00017 \times 10^{-6}$ $\frac{m}{s^2}$ based on the known deflection measurement error. Peak acceleration was calculated to be 35 $\frac{m}{s^2}$. The scale used to measure the mass was an Acculab VI-1mg with an uncertainty of $\pm .0005$ g. Using Equation B.1, the calculated force uncertainty was $\pm .018$ N for a mass of 1.2 g. This compares poorly to recorded force values from the engine (43 mN) and is due primarily to uncertainty in the mass measurement.

B.3 Engine to Engine Performance Variation

To determine the typical engine to engine performance variation at sub-resonant conditions, several engines were constructed and tested across the same energy inputs and operating frequencies. A typical plot of engine deflection is shown in Figure B.1. The deflection of the

micro-engine top membrane is recorded at 20 Hz as a function of increasing heat input. Six micro-engines were considered to establish the trend for this operating point. Similar data was recorded for the remaining micro-engine performance metrics including work output, operating efficiency, and power output.

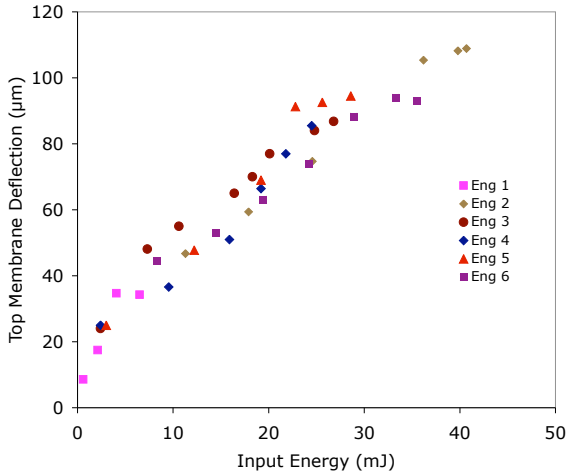

Figure B.1: 20 Hz 5 mm Si Engine Deflection with 10 μm Wicks

Figure B.1 clearly shows the variability associated with different micro-engine constructions. To establish overall engine-to-engine variability for the various performance metrics the peak performance points of each micro-engine were considered. These points were averaged and a standard deviation (68 % confidence) was established to describe the range expected for typical micro-engine operation. Appendix C details these average peak values and standard deviations in full. Table B.1 shows these values for the deflection of 5 mm micro-engines as shown in Figure B.1.

Average Peak Deflection and Standard Deviation				
Engine	**Wicks**	**20 Hz**	**40 Hz**	**100 Hz**
5 mm Si	10 μm	93.7 μm	102.8 μm	94 μm
	Deviation	9.3	5.9	5.6

Table B.1: 5 mm Silicon Average Peak Deflection and Standard Deviation

The typical engine-to-engine variance was established through examination of the standard deviation. In the case of deflection presented in Table B.1, an overall variance was established

using a weighted averaging technique which accounted for the number of engines operated at each point (20, 40, and 100 Hz). The deflection variance for a 5 mm micro-engine with 10 μm high wicks and silicon top membrane was found to be 6.95 μm . This technique was applied to the remaining performance parameters and various micro-engine assemblies.

This method produces a conservative estimate of typical engine-to-engine operating variance or uncertainty. Inherent to this approach is the determination of the average *peak* performance points. These peak performance points typically represent the greatest range of micro-engine variability simply because some engines peak before others. This is related to many factors including the amount of liquid working fluid available for evaporation at higher energy inputs. In essence, by concentrating on these points, the calculated standard deviations are highest. This leads to higher overall engine-to-engine variance values. These values are relatively small, however, and show the that various micro-engines perform within a relatively constrained performance envelope.

Appendix C

Engine Average Results and Standard Deviations

Chapter 7 presents the peak performance results of sub-resonant micro-engine operation given a variety of engine constructions and operating conditions. While these peak values accurately reflect the micro-engine capability, they do not reflect the spread of operating data as a result of testing so many different micro-engines.

This appendix presents the average peak performance for the various micro-engines as well as the standard deviations for these various performance values. As described in Chapter 7, the results presented correlate to several different micro-engine constructions operated at 20, 40, and 100 Hz using the thermal switch to reject heat.

C.1 Electrically Heated 5 mm Engine Operation

The average and standard deviation values corresponding to 5 mm micro-engine operation are presented in this section.

C.1.1 Silicon Top Membrane Results

The average maximum values and standard deviations are presented in the following tables for 5 mm silicon top membrane engines. The micro-engines were examined with increasing heat inputs at the operating frequencies of interest. Figure C.1 shows micro-engine top membrane deflection for the six engines that were tested. The average peak deflection was established by examination of the peak deflection point attained by each micro-engine. The standard deviation calculates the 68 % confidence interval about this average peak deflection. Similar data was used to determine the average peaks and standard deviations for the remaining micro-engine metrics: peak work output, maximum efficiency, and peak power output.

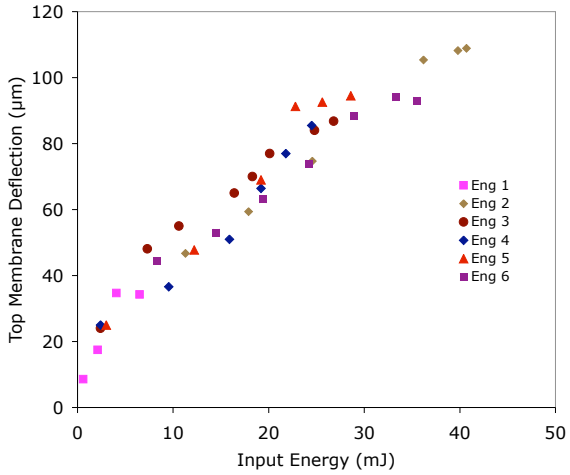

Figure C.1: 20 Hz 5 mm Top Membrane Deflection with 10 μm Wicks

Based on the data from Figure C.1, Table C.1 shows the average maximum deflection attained and standard deviation for all engines tested.

Average Peak Deflection and Standard Deviation				
Engine	**Wicks**	**20 Hz**	**40 Hz**	**100 Hz**
5 mm Si	10 μm	93.7 μm	102.8 μm	94 μm
	Deviation	9.3	5.9	5.6
5 mm Si	40 μm	96.2 μm	103.8 μm	97.4 μm
	Deviation	7.0	14.8	18.8

Table C.1: 5 mm Silicon Average Peak Deflection and Standard Deviation

Table C.2 shows the average maximum work output and standard deviation for these engines.

Average Peak Work Output and Standard Deviation				
Engine	**Wicks**	**20 Hz**	**40 Hz**	**100 Hz**
5 mm Si	10 μm	.0057 mJ	.0068 mJ	.0040 mJ
	Deviation	.0020	.0011	.0007
5 mm Si	40 μm	.0060 mJ	.0077 mJ	.0052 mJ
	Deviation	.0015	.0039	.0039

Table C.2: 5 mm Silicon Average Peak Work Output and Standard Deviation

Table C.3 shows the average maximum efficiency and standard deviation for these engines.

Average Peak Efficiency and Standard Deviation				
Engine	**Wicks**	**20 Hz**	**40 Hz**	**100 Hz**
5 mm Si	10 μm	.018 %	.028 %	.032 %
	Deviation	.003	.004	.006
5 mm Si	40 μm	.023 %	.033 %	.043 %
	Deviation	.004	.013	.023

Table C.3: 5 mm Silicon Average Peak Efficiency and Standard Deviation

Table C.4 shows the average maximum power output and standard deviation for these engines.

Average Peak Power Output and Standard Deviation				
Engine	**Wicks**	**20 Hz**	**40 Hz**	**100 Hz**
5 mm Si	10 μm	.11 mW	.27 mW	.40 mW
	Deviation	.04	.04	.07
5 mm Si	40 μm	.12 mW	.31 mW	.52 mW
	Deviation	.03	.16	.39

Table C.4: 5 mm Silicon Average Peak Power Output and Standard Deviation

C.1.2 Silicon-nitride Top Membrane Results

The average performance results and standard deviations are presented for 5 mm engines constructed using silicon-nitride top membranes. Table C.5 shows the average maximum deflection and standard deviation for all 5 mm SiNx engines tested.

Average Peak Deflection and Standard Deviation				
Engine	**Wicks**	**20 Hz**	**40 Hz**	**100 Hz**
5 mm SiNx	10 μm	155.9 μm	154.5 μm	176.4 μm
	Deviation	14.1	24.0	17.0
5 mm SiNx	40 μm	151.2 μm	152.3 μm	175.5 μm
	Deviation	16.0	11.3	16.7

Table C.5: 5 mm Silicon-nitride Average Peak Deflection and Standard Deviation

Table C.6 shows the average maximum work output and standard deviation for these engines.

Average Peak Work Output and Standard Deviation				
Engine	**Wicks**	**20 Hz**	**40 Hz**	**100 Hz**
5 mm SiNx	10 μm	.0150 mJ	.0144 mJ	.0185 mJ
	Deviation	.0018	.0053	.0061
5 mm SiNx	40 μm	.0125 mJ	.0120 mJ	.0110 mJ
	Deviation	.0047	.0028	.0092

Table C.6: 5 mm Silicon-nitride Average Peak Work Output and Standard Deviation

Table C.7 shows the average maximum efficiency and standard deviation for these engines.

Average Peak Efficiency and Standard Deviation				
Engine	**Wicks**	**20 Hz**	**40 Hz**	**100 Hz**
5 mm SiNx	10 μm	.068 %	.076 %	.147 %
	Deviation	.016	.025	.051
5 mm SiNx	40 μm	.046 %	.057 %	.131 %
	Deviation	.016	.011	.015

Table C.7: 5 mm Silicon-nitride Average Peak Efficiency and Standard Deviation

Table C.8 shows the average maximum power output and standard deviation for these engines.

Average Peak Power Output and Standard Deviation				
Engine	**Wicks**	**20 Hz**	**40 Hz**	**100 Hz**
5 mm SiNx	10 μm	.30 mW	.58 mW	1.8 mW
	Deviation	.04	.21	.61
5 mm SiNx	40 μm	.25 mW	.48 mW	1.1 mW
	Deviation	.09	.11	.93

Table C.8: 5 mm Silicon-nitride Average Peak Power Output and Standard Deviation

C.2 Electrically Heated 10 mm Engine Operation

The average and standard deviation values corresponding to 10 mm micro-engine operation are presented in this section. It is interesting to note, as mentioned in Chapter 7, the effect of premature evaporator membrane failure on the standard deviation values for these larger engines using 40 μm high wick structures. This typically occurred at operating frequencies of 20 Hz.

C.2.1 Silicon Top Membrane Results

The average maximum values and standard deviations are presented in the following tables for 10 mm, silicon top membrane engines.

Table C.9 shows the average maximum deflection attained and standard deviation for all engines tested.

Average Peak Deflection and Standard Deviation				
Engine	**Wicks**	**20 Hz**	**40 Hz**	**100 Hz**
10 mm Si	10 μm	184.5 μm	148.0 μm	171.5 μm
	Deviation	15.9	18.3	16.3
10 mm Si	40 μm	106.6 μm	203.4 μm	228.0 μm
	Deviation	26.1	23.7	56.6

Table C.9: 10 mm Silicon Average Peak Deflection and Standard Deviation

Table C.10 shows the average maximum work output and standard deviation for these engines.

Average Peak Work Output and Standard Deviation				
Engine	**Wicks**	**20 Hz**	**40 Hz**	**100 Hz**
10 mm Si	10 μm	.0204 mJ	.0100 mJ	.0065 mJ
	Deviation	.0058	.0034	.0015
10 mm Si	40 μm	.0040 mJ	.0267 mJ	.0160 mJ
	Deviation	.0031	.0101	.0132

Table C.10: 10 mm Silicon Average Peak Work Output and Standard Deviation

Table C.11 shows the average maximum efficiency and standard deviation for these engines.

Average Peak Efficiency and Standard Deviation				
Engine	**Wicks**	**20 Hz**	**40 Hz**	**100 Hz**
10 mm Si	10 μm	.024 %	.016 %	.024 %
	Deviation	.005	.008	.002
10 mm Si	40 μm	.006 %	.039 %	.042 %
	Deviation	.004	.013	.024

Table C.11: 10 mm Silicon Average Peak Efficiency and Standard Deviation

Table C.12 shows the average maximum power output and standard deviation for these engines.

Average Peak Power Output and Standard Deviation				
Engine	**Wicks**	**20 Hz**	**40 Hz**	**100 Hz**
10 mm Si	10 μm	.41 mW	.40 mW	.65 mW
	Deviation	.12	.14	.15
10 mm Si	40 μm	.08 mW	1.1 mW	1.6 mW
	Deviation	.06	.41	1.3

Table C.12: 10 mm Silicon Average Peak Power Output and Standard Deviation

C.2.2 Silicon-nitride Top Membrane Results

The average maximum values and standard deviations are presented in the following tables for 10 mm, silicon-nitride top membrane engines.

Table C.13 shows the average maximum deflection attained and standard deviation for all engines tested.

Average Peak Deflection and Standard Deviation				
Engine	**Wicks**	**20 Hz**	**40 Hz**	**100 Hz**
10 mm SiNx	10 μm	220.5 μm	255.7 μm	243.5 μm
	Deviation	12.6	18.5	20.5
10 mm SiNx	40 μm	132.4 μm	200.6 μm	271.5 μm
	Deviation	54.2	8.1	4.9

Table C.13: 10 mm Silicon-nitride Average Peak Deflection and Standard Deviation

Table C.14 shows the average maximum work output and standard deviation for these engines.

Average Peak Work Output and Standard Deviation				
Engine	**Wicks**	**20 Hz**	**40 Hz**	**100 Hz**
10 mm SiNx	10 μm	.0203 mJ	.0256 mJ	.0106 mJ
	Deviation	.0033	.0038	.0030
10 mm SiNx	40 μm	.0060 mJ	.0127 mJ	.0208 mJ
	Deviation	.0054	.0015	.0015

Table C.14: 10 mm Silicon-nitride Average Peak Work Output and Standard Deviation

Table C.15 shows the average maximum efficiency and standard deviation for these engines.

Average Peak Efficiency and Standard Deviation				
Engine	**Wicks**	**20 Hz**	**40 Hz**	**100 Hz**
10 mm SiNx	10 μm	.027 %	.045 %	.040 %
	Deviation	.006	.002	.008
10 mm SiNx	40 μm	.013 %	.023 %	.070 %
	Deviation	.007	.002	.011

Table C.15: 10 mm Silicon-nitride Average Peak Efficiency and Standard Deviation

Table C.16 shows the average maximum power output and standard deviation for these engines.

Average Peak Power Output and Standard Deviation				
Engine	**Wicks**	**20 Hz**	**40 Hz**	**100 Hz**
10 mm SiNx	10 μm	.41 mW	1.0 mW	1.0 mW
	Deviation	.07	.15	.30
10 mm SiNx	40 μm	.12 mW	.51 mW	2.1 mW
	Deviation	.11	.06	.15

Table C.16: 10 mm Silicon-nitride Average Peak Power Output and Standard Deviation

Appendix D

Alternative Engine Working Fluids

Over the course of this work, several micro-engine working fluids have been considered for use. Table D.1 shows some of the fluids and their properties.

Alternative Engine Working Fluids				
Fluid	**Boiling Point** (K)	**Latent Heat** (kJ/mol)	**Vapor Pressure** (kPa)	**Molec Weight** (g/mol)
pf-5060dl	329	31	30.9	360
IPA	356	40	4.2	60
R-11	297	180	105.5	138
R-123	301	26	91	153
R-12	244	165	652	121
R-134a	247	22	665	102
n-Pentane	309	26	73.2	72
Heptane	371	32	6.1	100

Table D.1: Alternative Working Fluids

Appendix E

Evaporator Membrane Suitability for Pressure Measurement

It has long be accepted that the top membrane, when operated at sub-resonant conditions, is suitable for pressure and volume determination. The suitability of using the evaporator membrane as a source of pressure measurement is examined in this Appendix.

To ascertain evaporator membrane suitability, a micro-engine was operated at sub-resonance. The deflections of the two membranes and their temperatures were monitored. The membrane deflections were converted to pressure by applying their respective pressure-deflection calibration curves. As the top membrane was already accepted as a reliable source for pressure measurement, its measured pressure was compared to that of the evaporator membrane as the first validating step.

Temperatures measured via RTD were used as a second validating step. By using the measured temperatures, a theoretical pressure was determined based on a simple model. This theoretical pressure then served as a final validation for the suitability of evaporator

membrane pressure measurements.

A simplified micro-engine was constructed for this work. It was assembled with a 9 mm cross-type evaporator membrane, a 150 μm cavity, and a 10 mm SiNx top membrane. Temperature of both membranes was recorded using RTDs. Only air was present in the engine cavity during these tests. As typical with other sub-resonant testing, the micro-engine was aligned over a cooled thermal switch and heated electrically. It was operated at 20 Hz and given 8.5 mJ of heat per cycle. Section 5.2.1 details this basic setup and operation. The top and evaporator membrane deflections were recorded and converted to pressure. The recorded pressures from this run are shown in Figure E.1. Good agreement was noted between top and evaporator membrane pressure measurements. This provided the first validation.

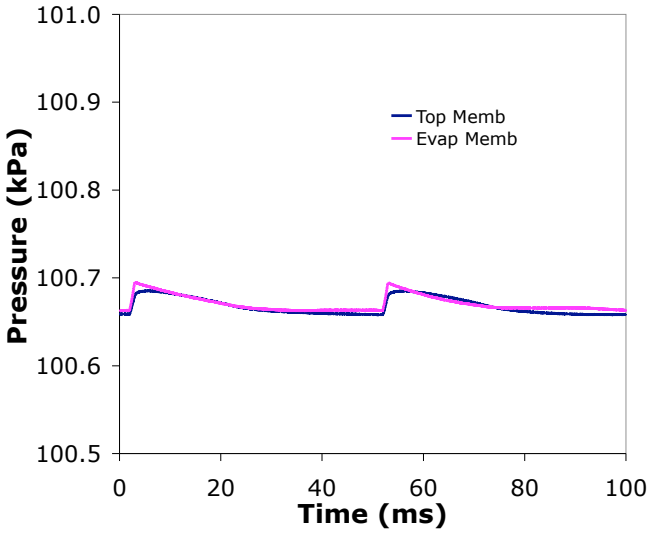

Figure E.1: Comparison of Pressures Measured by Engine Membranes

Temperatures from the top and evaporator membranes were also recorded during these tests as shown in Figure E.2. Because air was selected as the micro-engine working fluid, the ideal gas equation was used to relate the recorded membrane temperatures noted in Figure E.2 to the theoretical cavity pressure. Equation E.1 shows the ideal gas equation used to model this simplified micro-engine.

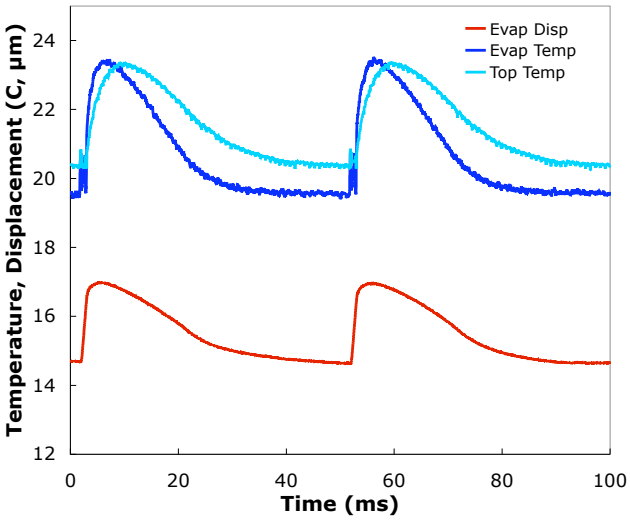

Figure E.2: Temperature of Top and Evaporator Membranes

$$P = \rho RT \tag{E.1}$$

P: Pressure
ρ: Density
R: Gas constant
T: Temperature

Equation E.1 was used to convert the measured temperature of the top membrane to a theoretical cavity pressure. The uncertainty of the RTD measurement was taken into account. Figure E.3 shows the results of this simple model. For comparison, the pressure measured by membrane deflection is also included. While the ideal gas equation over-predicted the measured pressure, the measured pressure fell within the uncertainties associated with RTD measurements.

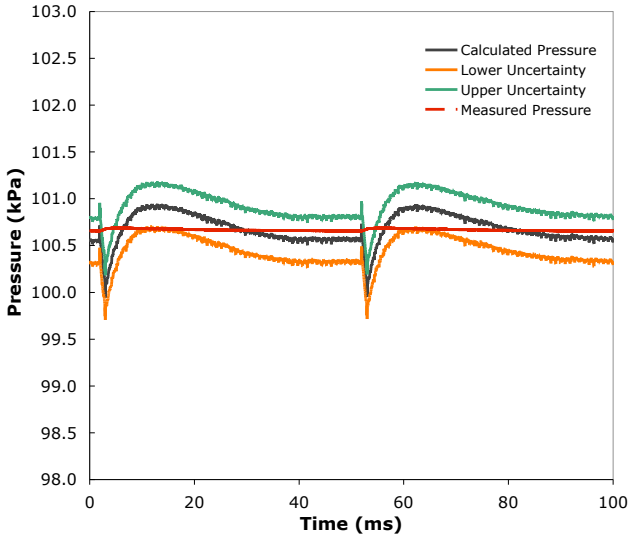

Figure E.3: Predicted Pressures based on Measured Temperature

Equation E.1 was also used to check the validity of the temperature measurements based on the membrane pressure measurement. Figure E.4 shows the results when the top membrane pressure was considered for the calculation.

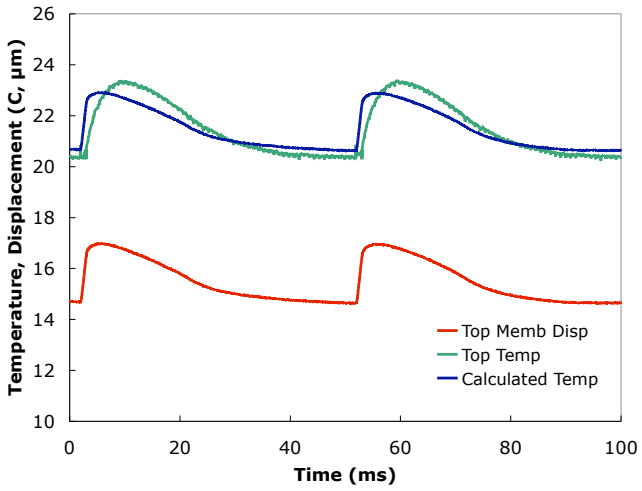

Figure E.4: Predicted Temperature based on Measured Pressure

As with the pressure calculation, the predicted temperature fell within the range of known RTD uncertainty as shown in Figure E.5.

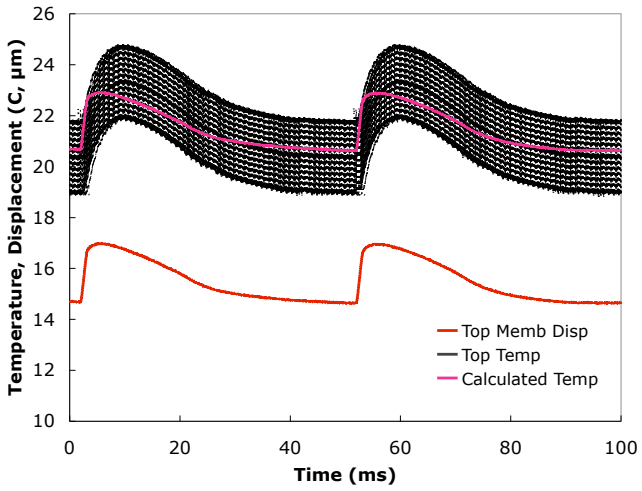

Figure E.5: Predicted Temperature within Uncertainty

Based on these findings, the use of the lower membrane to monitor engine operating pressure was validated. It compared well to measured pressure values taken via top membrane deflection. Additionally, the measured temperatures verified the recorded pressure when a simplified ideal gas model was used.

Appendix F

Engine Carrier Designs

Drawings of the acrylic engine carriers used in this dissertation are provided in this Appendix. Figure F.1 shows the dimensions and specifications for carriers used with 5 mm micro-engines. Figure F.2 shows the dimensions and specifications for carriers used with 10 mm micro-engines.

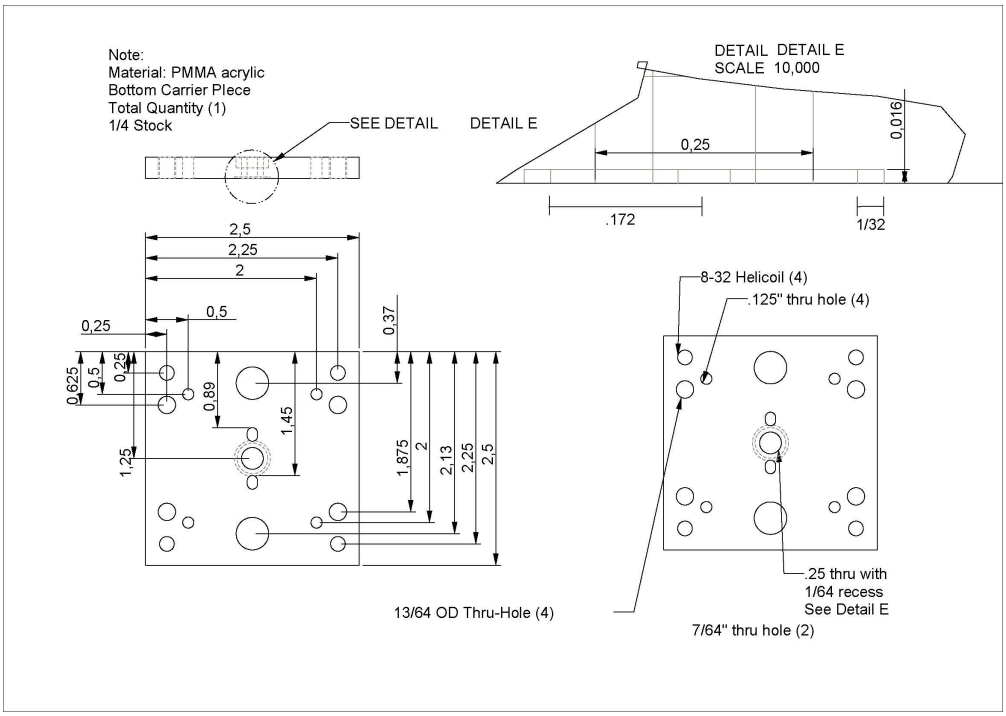

(a) Bottom

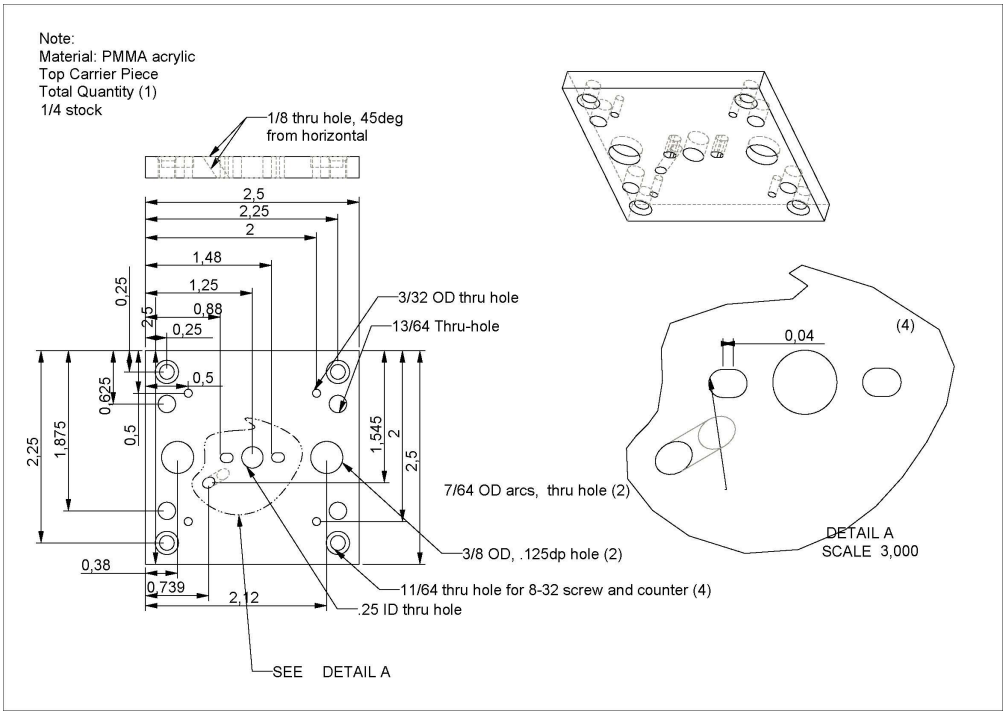

(b) Top

Figure F.1: 5 mm Acrylic Engine Carrier Pieces

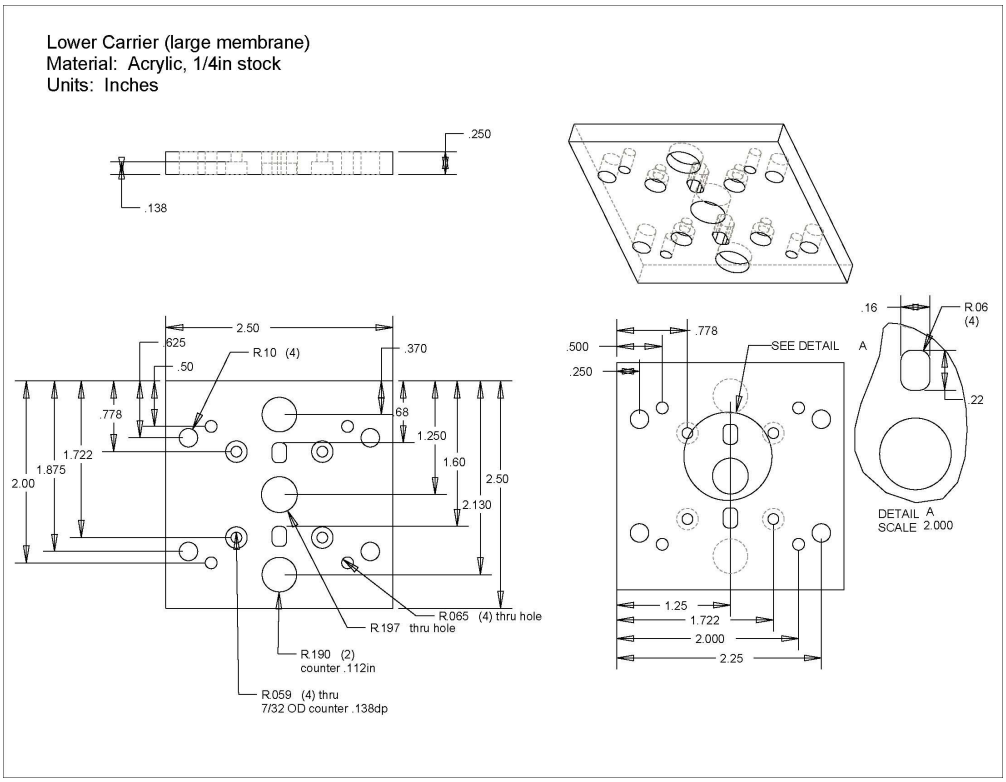

(a) Bottom

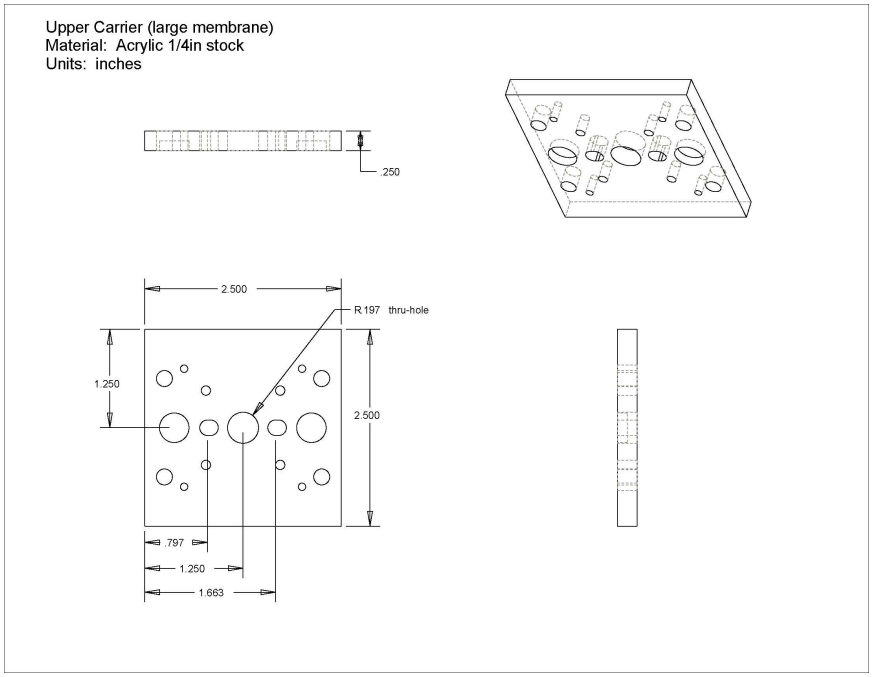

(b) Top

Figure F.2: 10 mm Acrylic Engine Carrier Pieces